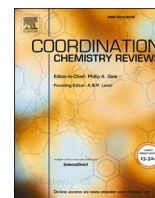




Contents lists available at ScienceDirect

## Coordination Chemistry Reviews

journal homepage: [www.elsevier.com/locate/ccr](http://www.elsevier.com/locate/ccr)

## A review on the advancements in covalent organic frameworks for photocatalytic reduction of carbon dioxide

Chien Ing Yeo<sup>a,1</sup>, Yee Seng Tan<sup>a,1</sup>, Hafiz Taimoor Ahmed Awan<sup>b</sup>, Abdul Hanan<sup>b</sup>,  
Weng Pin Wong<sup>b</sup>, Rashmi Walvekar<sup>c,d</sup>, Bey Hing Goh<sup>a,e,f</sup>, Mohammad Khalid<sup>g,h,i,\*</sup>

<sup>a</sup> Sunway Biofunctional Molecules Discovery Centre, School of Medical and Life Sciences, Sunway University, No. 5, Jalan University, Bandar Sunway, 47500, Darul Ehsan, Selangor, Malaysia

<sup>b</sup> Sunway Centre for Electrochemical Energy and Sustainable Technology (SCEEST), School of Engineering and Technology, Sunway University, No. 5, Jalan University, Bandar Sunway, 47500, Darul Ehsan, Selangor, Malaysia

<sup>c</sup> Faculty of Innovation and Technology, School of Engineering, Chemical Engineering Programme, No.1 Jalan Taylor's, Taylor's University Malaysia, 47500 Subang Jaya, Selangor, Malaysia

<sup>d</sup> Chitkara Centre for Research and Development, Chitkara University, Himachal Pradesh 174103, India

<sup>e</sup> Biofunctional Molecule Exploratory Research Group, School of Pharmacy, Monash University Malaysia, 47500 Bandar Sunway, Selangor Darul Ehsan, Malaysia

<sup>f</sup> Faculty of Health, Australian Research Centre in Complementary and Integrative Medicine, University of Technology Sydney, Ultimo, NSW, Australia

<sup>g</sup> Materials and Manufacturing Research Group, James Watt School of Engineering, University of Glasgow, Glasgow G12 8QQ, UK

<sup>h</sup> Faculty of Engineering, Manipal University Jaipur, Rajasthan 303007, India

<sup>i</sup> Centre for Research Impact and Outcome, Chitkara University, Punjab 140401, India

## ARTICLE INFO

## Keywords:

Covalent organic frameworks  
Photocatalytic reduction  
Carbon dioxide  
Sustainability

## ABSTRACT

Carbon dioxide (CO<sub>2</sub>) emissions from human activities have raised atmospheric CO<sub>2</sub> levels to unsafe highs, necessitating the development of technologies to capture and utilize this greenhouse gas. Photocatalytic conversion of CO<sub>2</sub> into value-added chemicals and fuels using solar energy has attracted significant research interest as a carbon capture and utilization approach. However, existing photocatalysts suffer from limitations such as low efficiency, instability, and poor selectivity. Covalent organic frameworks (COFs) are an emerging class of organic porous materials that show promise for photocatalytic CO<sub>2</sub> reduction applications due to their tuneable properties, high surface areas, and photochemical stability. This review provides an overview of recent advances in the development of COF-based photocatalysts for improving the efficiency of solar-driven CO<sub>2</sub> reduction. Key strategies investigated include functional group incorporation, metal doping, and integration of cocatalyst nanoparticles. Introducing polar functional groups and metal ions via doping has been demonstrated to enhance CO<sub>2</sub> binding affinity and adsorption capacity within COF structures. The incorporation of noble metal cocatalysts promotes efficient charge separation and transfer, improving photocatalytic activity. Experimental and computational studies have provided insights into structure-activity relationships, linking photocatalytic performance to factors such as pore size, crystallinity, functional group polarity, and electronic structure. Further optimization of COF compositions, morphologies, and interfaces holds promise for realizing highly efficient and durable photocatalytic systems for CO<sub>2</sub> reduction. Realizing the full potential of COFs will require the development of robust structure-property correlations to guide rational material design. With continued advances, COFs may enable economically viable and sustainable technologies for converting CO<sub>2</sub> emissions into valuable chemicals and fuels using only sunlight as an energy input.

### 1. Introduction

Increasing energy demand has initiated the global energy crisis and implicated households and global economies. According to the

International Energy Agency (IEA), energy-related carbon dioxide (CO<sub>2</sub>) emissions have increased and contributed to the largest annual emission rise of 36.3 Gt in 2021. Under a conservative scenario known as stated policies scenario (STEPS), it was estimated that the emission will reach a

\* Corresponding author at: Materials and Metallurgy Research Group, James Watt School of Engineering, University of Glasgow, Glasgow G12 8QQ, UK  
E-mail address: [mohammad.khalid@glasgow.ac.uk](mailto:mohammad.khalid@glasgow.ac.uk) (M. Khalid).

<sup>1</sup> Equal contributing authors.

<https://doi.org/10.1016/j.ccr.2024.216167>

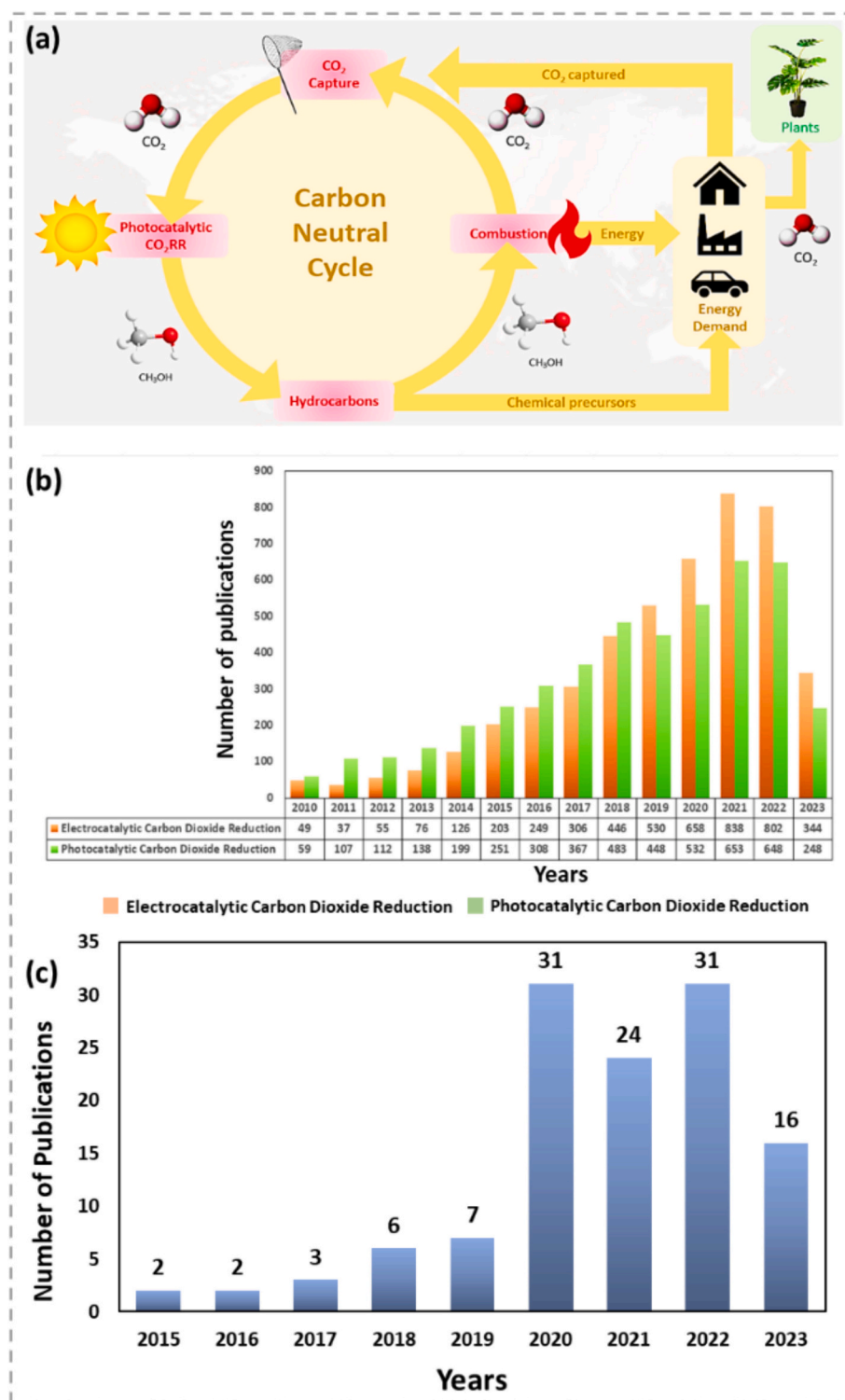
Received 15 January 2024; Received in revised form 30 July 2024; Accepted 17 August 2024

Available online 29 August 2024

0010-8545/© 2024 The Author(s). Published by Elsevier B.V. This is an open access article under the CC BY-NC license (<http://creativecommons.org/licenses/by-nc/4.0/>).

plateau of around 37 Gt before decreasing to 32 Gt in 2050. This would lead to a 2.5 °C rise in global average temperature by 2100 and the environment can be severely impacted by melting icebergs, rising sea levels and species extinction [1]. Fossil fuels have been the main source of CO<sub>2</sub> emissions, so the current primary strategy for reducing CO<sub>2</sub> emissions is utilizing clean energy sources such as solar, wind, hydro-power and geothermal energy [2]. The largest increment in renewable energy capacity to date has been achieved in 2022, with 295 GW of

renewable energy addition and 83% of global power additions. Solar power has accounted for 2/3 of the renewable energy addition [3]. It can be further classified into concentrated solar power (CSP), photovoltaic (PV) or concentrated solar photovoltaic (CPVT) systems [4]. However, it was pointed out that these alternative sources are inconsistent, unpredictable and depending on some variables such as timing, location, and weather conditions [3]. These challenges have been the main barriers to reducing CO<sub>2</sub> emissions via clean energy sources, as a continuous and



**Fig. 1.** (a) Carbon neutral cycle. Reproduced with permission from [7]. (b) Number of publications related to "electrocatalytic carbon dioxide reduction" and "photocatalytic carbon dioxide reduction" since 2010 and (c) Number of publications with the keywords "COFs" and "photocatalytic carbon dioxide reduction".

stable energy supply cannot be assured.

The existing challenges with renewable energy production have sparked the interest to convert CO<sub>2</sub> into various useful end products such as methane (CH<sub>4</sub>), ethylene (C<sub>2</sub>H<sub>4</sub>), methanol (CH<sub>3</sub>OH), carbon monoxide (CO), formaldehyde (HCHO), formic acid (HCOOH) and carbon monoxide (CO) [5,6]. In an ideal carbon neutral cycle, as shown in Fig. 1 (a), the CO<sub>2</sub> emissions from households, industries and vehicles are collected using various carbon capture and sequestration technologies and converted into hydrocarbons for combustion or chemical precursors, thus forming an overall zero-carbon loop [7]. Generally, the conversion of CO<sub>2</sub> can be categorized into biological, chemical, reforming, inorganic transformations, electrochemical and photocatalytic processes [3]. Among these processes, electrochemical and photocatalytic CO<sub>2</sub> reduction reaction (CO<sub>2</sub>RR) have shown great potential in converting the CO<sub>2</sub> efficiently.

Electrochemical CO<sub>2</sub>RR has the advantage of practical applicability, where the CO<sub>2</sub>RR can be achieved under mild conditions by applying electricity across two electrodes [7]. Fossil fuels have historically met a substantial portion of electricity demand. However, recent trends indicate a significant shift towards renewable energy sources such as wind and hydropower for electricity generation. This transition is primarily driven by the goal of reducing CO<sub>2</sub> emissions and mitigating climate change impacts. By harnessing these cleaner energy alternatives, the reduction in greenhouse gas emissions can be achieved, promoting a more sustainable and environmentally friendly energy landscape [8]. Nevertheless, the electrocatalysts required are often cost-ineffective, rare, high overpotentials, low selectivity and degraded over repeated cycles [9,10]. Meanwhile, photocatalytic CO<sub>2</sub>RR has the advantage of using only sunlight to initiate the CO<sub>2</sub> conversion process and alleviates the use of chemicals or external energy, as in the case of electrochemical CO<sub>2</sub>RR [11]. This might be the reason of more investigations have been conducted on photocatalytic CO<sub>2</sub>RR than electrocatalytic CO<sub>2</sub>RR since 2010, according to statistics from Web of Science (Fig. 1(b)). However, photocatalytic CO<sub>2</sub>RR also has the limitations of low catalytic efficiencies, low selectivity of organic products, rapid recombination of charge carriers, small working surface areas for CO<sub>2</sub> adsorption, degradation over repeated cycles, cost ineffectiveness and not able to absorb wavelengths in visible light spectrum due to larger bandgaps [1]. These limitations might be the main factor leading to a shift of research focus towards the electrocatalytic CO<sub>2</sub>RR since 2019. In addition, the gap between the number of publications has also increased by 88% since then up to 2022. This has shown that emerging photocatalysts are urgently required in order to commercialize the photocatalytic CO<sub>2</sub>RR [12,13].

Recently, various studies using homogenous and heterogeneous catalysts were extensively conducted for the photocatalytic CO<sub>2</sub>RR. Homogenous catalysts have high photocatalytic activity and selectivity for the desired end products. Still, they are not stable during extended usage and are expensive as they are rare metals that are challenging to separate and recover at the end of the photocatalytic process [14]. Meanwhile, heterogeneous catalysts can avoid the problems mentioned above, but it has low catalytic activity [15]. Therefore, anchoring metal catalysts on supports such as metal organic frameworks (MOFs) and covalent organic frameworks (COFs) [16] yields single-site photocatalysts, offering viable alternatives. MOFs have been reported as photocatalysts to produce CO or formate [17], while COFs have been reported as photocatalysts to produce hydrogen. Using MOFs as model materials to graft the single-site catalytic organometallics can be another alternative for photocatalytic CO<sub>2</sub>RR as it can hinder the catalyst deactivation or undesired reactions by eliminating the involvement of undesired dimeric species [15,18]. Meanwhile, COFs, such as materials containing bipyridine, triazine and triformyl glucinol building blocks [19], have received tremendous attention for the photocatalytic CO<sub>2</sub>RR since 2020, according to statistics of Web of Science (Fig. 1(c)). The triazine functionality usually enhances photocatalytic activity by increasing the charge separation efficiency during the photocatalysis

process [19]. Compared to 2019, the number of publications in 2020 with the keywords “COFs” and “photocatalytic carbon dioxide reduction” has increased by 4.4 times.

In the last decade, the discussion on recent advancements in using COFs for photocatalytic CO<sub>2</sub>RR has been limited. A comprehensive synthesis of synthetic methods and recent progress in COF-mediated photocatalytic CO<sub>2</sub>RR has been presented by You et al. [20]. This review encompasses various aspects, including photocatalytic degradation, organic transformations via photocatalysis, CO<sub>2</sub>RR, and hydrogen evolution reaction (HER) through water splitting. Simultaneously, Sarkar et al. [21] have extensively reported the recent progress of COFs serving as heterogeneous catalysts for CO<sub>2</sub>RR through photochemical, electrochemical, and photo-electrochemical methods. The review delves into the physicochemical properties of COFs and their influence on CO<sub>2</sub>RR selectivity, efficiency, and recyclability.

Moreover, a systematic examination of various COF types, applications, current trends, and future directions in the context of CO<sub>2</sub>RR has been presented [22]. To address existing research gaps, a detailed exploration of mechanisms, strategies for structure modification, emerging advances, and a comparative analysis of COFs with other photocatalysts is crucial. This review aims to comprehensively study and scrutinize these aspects, providing insights into the current trajectory and future prospects of COFs as photocatalysts for CO<sub>2</sub>RR.

## 2. Properties of COFs

COFs are highly structured organic polymers with exceptional porosity and offer a wide range of uses [23–25]. The covalent bonding between building units of these materials is responsible for their stable and well-organised structures [26,27]. Generally, COFs can exist in 2D or 3D forms, rendering them promising in the fields of energy storage, drug delivery, electronics, photonics, and sensor technologies, as discussed in the literature [24,28–32]. Beyond these applications, COFs find utility in diverse areas, such as gas storage [33–37], separation [37–40], sensing [41–43], and catalysis [44,45], to name a few. Notably, COFs have emerged as significant contributors to photocatalytic CO<sub>2</sub> reduction, showcasing exceptional efficacy in converting CO<sub>2</sub> into valuable compounds like methane, methanol, or formic acid utilizing solar energy [22,46–48]. This multifaceted functionality positions COFs as key materials in various scientific domains, underlining their potential impact across a spectrum of applications. COFs are synthesized through various reactions, such as Schiff-base condensation, boronate ester formation, and imine condensation [49,50]. These reactions facilitate the direct linkage of monomers, resulting in the creation of extensive networks and diverse frameworks with periodic pores. The fundamental building blocks of COFs are typically organic molecules featuring different reactive sites, such as amines, aldehydes, and boronic acids. These sites enable the formation of expanded 2D or 3D networks, allowing for a wide range of structural and functional properties in the resulting COFs [30,51].

Two-dimensional (2D) COFs consist of layers of covalently bonded organic molecules arranged in a planar fashion, resulting in highly ordered 2D sheets [52]. These layers are further interconnected through  $\pi$ - $\pi$  stacking interactions, which involve non-covalent forces arising from the overlap of electron clouds in aromatic rings. This  $\pi$ - $\pi$  stacking not only stabilizes the structure but also creates well-defined channels and periodic pores within the material. The precise arrangement of these 2D layers enables a high degree of crystallinity, which is crucial for the desirable properties of COFs [53]. Moreover, the planar structure of these 2D COFs contributes exceptionally to their large specific surface area where each layer formation gives the broad expanse of surface that is easily accessible to the guest molecule, forming these materials a viable candidate for the applications that rely on the surface interactions like gas separation and storage respectively. Additionally, the increased surface area boosts the capacity of materials to absorb these gases or opens the other channel, which is formed by  $\pi$ - $\pi$  stacking interactions

that facilitate the ions diffusion of guest molecules across the channel and structure [54,55]. This allows molecules to flow freely within the COF, which is useful for processes like catalysis, where reactants must effectively reach active sites. Another crucial feature of 2D COFs is their effective charge transport. In addition to stabilizing the layers, the  $\pi$ - $\pi$  stacking interactions provide channels for electron mobility. This is especially crucial for applications requiring effective charge separation and transfer, such as electrical devices, photovoltaics, and photocatalysis. The stacked layers' delocalized  $\pi$ -electrons have the highest mobility, which modifies the conductivity of materials with overall performance in different applications. Apart from these various features, 2D COFs' structural adaptability enables tunability. Researchers can modify the surface area, pore size, and electrical characteristics of the COFs to fit different applications by selecting various building blocks. The controlled synthesis of the COFs is made possible by the chosen covalent connections and the thoughtful design of the organic monomers. The variety of possible applications can be increased by post-synthetic alterations, which can also bring new or improved features respectively.

In contrast, three-dimensional (3D) COFs are constructed from a 3D network of interconnected pores, forming a robust and stable framework [56]. These structures are assembled from organic molecules linked by strong covalent bonds, resulting in an extensive network that spans all three spatial dimensions. This comprehensive spatial arrangement creates a rigid architecture, endowing the material with high mechanical and thermal stability. Due to their exceptional stability, 3D COFs are particularly valuable for applications requiring long-term durability or that will be exposed to harsh environmental conditions [57,58]. The interconnected pores within 3D COFs possess unique properties that significantly enhance their functionality. These pores offer a large surface area, facilitating the easy adsorption of molecules. Furthermore, the high porosity of 3D COFs makes them suitable for applications such as gas storage, as they can contain substantial amounts of gas within their structure. The uniform and well-defined pore diameters of 3D COFs also enable selective adsorption, allowing for the separation of specific gases or compounds from mixtures [59]. This selective capability is crucial in applications like carbon capture, where COFs are used to selectively capture CO<sub>2</sub> while allowing other gases to pass through efficiently.

COFs exhibit unique properties that make them suitable for photocatalytic CO<sub>2</sub> reduction, including their ability to generate electron-hole pairs and absorb light [60,61]. This capability is accomplished by judiciously selecting particular building components that enable effective electron transmission. This functionality is achieved through the strategic selection of building components that facilitate efficient electron transfer. COFs possess well-structured electrical systems that allow them to produce electron and hole pairs upon light absorption. This process involves the excitation of electrons from the VB to the CB, resulting in the formation of electron-hole pairs.

The electrical structure of COFs, particularly their tunable bandgap and conjugated systems, plays a significant role in the efficiency of electron-hole pair generation and separation. Researchers can further enhance charge separation by carefully selecting and designing building blocks with appropriate electrical properties, potentially creating donor-acceptor pairs or optimizing  $\pi$ -conjugation. This enhancement is vital for improving the photocatalytic activity of COFs, as it allows for more effective utilization of absorbed light energy to drive photocatalytic reactions. The separation efficiency of electron-hole pairs can be further improved by incorporating electron donor-acceptor components that facilitate electron transfer [62]. Additionally, COFs feature a well-defined periodic array of electron channels, and the  $\pi$ -conjugated stacking supports efficient electron transport and promotes electronic delocalization [62]. These attributes highlight the potential of COFs for advanced CO<sub>2</sub> reduction applications and enhance their overall performance as a framework for photocatalytic processes.

Furthermore, the large surface area and the ability of COFs to support a high density of active sites make them exceptionally well-suited

for photocatalytic CO<sub>2</sub> reduction [61]. The high surface area of COFs, as a result of their porous structure, can be tailored through the selection of building blocks or post-synthesis alterations [63]. Such tunability enhances the adsorption of CO<sub>2</sub> molecules, facilitating their conversion into valuable products [62,64]. Additionally, the outstanding chemical and physical stability of COFs contributes to their durability and recyclability as photocatalysts [65–67]. Collectively, these properties position COFs as ideal candidates for photocatalytic CO<sub>2</sub> reduction.

### 3. Potential applications of COFs for photocatalytic CO<sub>2</sub> reduction

There has been a rising interest in the increased CO<sub>2</sub> adsorption capabilities of catalysts based on COFs in the field of scientific study. These extraordinary materials, which are made up of porous structures produced by organic building blocks, have large surface areas and variable pore diameters [68]. Because of these features, COFs are ideal for CO<sub>2</sub> capture. Recent advances have aimed to refine COFs by including functional groups or metal ions in their structures, resulting in catalysts with increased CO<sub>2</sub> adsorption capacity and selectivity [69]. This advancement offers enormous potential for tackling the pressing problem of climate change by reducing greenhouse gas emissions. The improved COF catalysts not only feature increased adsorption efficiency but also selectively collect CO<sub>2</sub> from mixed gas streams. This differentiating property is critical in extracting CO<sub>2</sub> from industrial operations and power plants, where the gas is often present in conjunction with other molecules. Furthermore, the recyclability of these catalysts adds to their attractiveness as possible instruments for constructing efficient and sustainable carbon capture methods.

Improved CO<sub>2</sub> adsorption characteristics in COF-based catalysts have far-reaching ramifications that go beyond theoretical considerations. It opens the path for practical applications that may dramatically cut CO<sub>2</sub> emissions while also easing the transition to a greener, more sustainable future. Scientists and engineers are actively striving to solve the difficulties presented by climate change by using the outstanding capabilities of COFs, all while promoting a cleaner and healthier environment for future generations. Due to their potential for sustainable energy conversion, COFs have received a lot of interest in the context of photocatalytic CO<sub>2</sub> reduction. Because of their adjustable features and strong architectures, COFs provide a diverse platform for photocatalysis [67]. The stability of COFs is critical in the search for effective and long-lasting CO<sub>2</sub> reduction catalysts. These frameworks must endure harsh conditions, including prolonged exposure to light, moisture, and reactive intermediates. To enhance COF stability, researchers have employed various strategies such as structural modifications, post-synthetic treatments, and encapsulation techniques [70].

In this context, Monte Carlo simulation and density functional theory (DFT) calculations were used to evaluate the effect of different functional groups in COFs on CO<sub>2</sub> sorption. The findings showed that the interaction between COFs and CO<sub>2</sub> was critical at low pressures, but at high pressures, COF pore diameters were the major determinant. Functionalization significantly improved CO<sub>2</sub> sorption selectivity over N<sub>2</sub>, CH<sub>4</sub>, and H<sub>2</sub>. At ambient temperature and 1 bar pressure, functional groups such as —CH<sub>2</sub>NH<sub>2</sub>, —SO<sub>3</sub>H, —COOH, and —OCO(CH<sub>2</sub>)<sub>2</sub>—COOH showed increased CO<sub>2</sub> sorption capacities. The —SO<sub>3</sub>H functional group emerged as the most viable choice for CO<sub>2</sub> extraction from mixed gas streams. These results shed light on the role of functional groups in CO<sub>2</sub> sorption and provide useful insights for creating COFs with improved CO<sub>2</sub> capture and separation capabilities [73]. Kang and colleagues improved the efficacy of two COFs, namely NUS-3 and NUS-2, featuring unique pore diameters and water resistance, by introducing poly(ether imide) or PBI (polybenzimidazole) into mixed matrix membranes (MMMs). Because of the excellent selective sorption power of the fillers included inside the COFs, the resultant COFs separated CO<sub>2</sub> from H<sub>2</sub> with remarkable efficiency [74]. In their study, Alahakoon and colleagues created azine-linked COFs and added aldehyde groups as

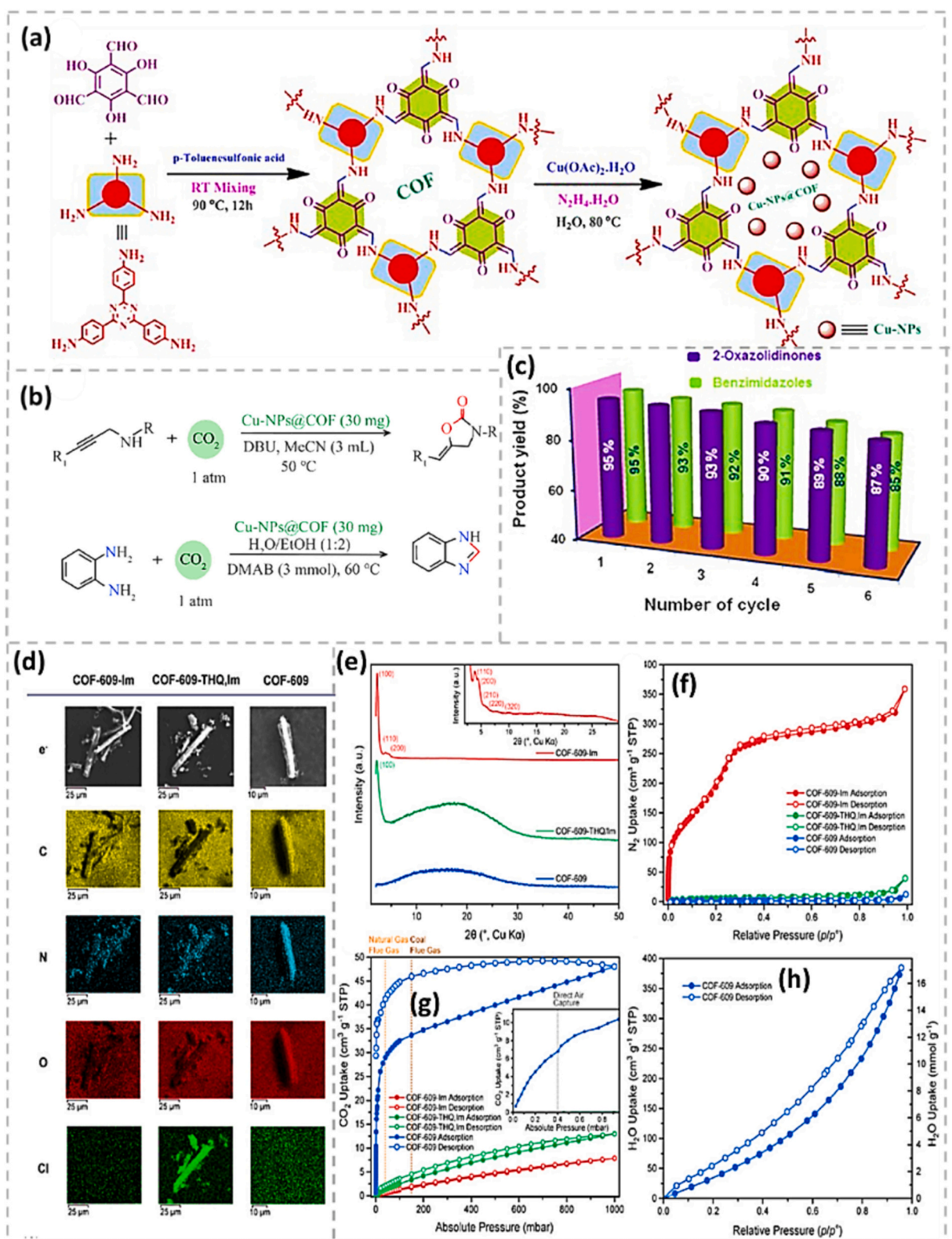
functional moieties. These COFs have pore sizes of 1 nm and a surface area of  $>1200 \text{ m}^2 \text{ g}^{-1}$ . Remarkably, they demonstrated a high  $\text{CO}_2$  sorption capability, able to adsorb up to 20% of  $\text{CO}_2$  at the pressure of 1 atm and a temperature of 273 K. Furthermore, the researchers successfully created  $\text{NH}_2\text{-UiO-66@Br-COFs}$  hybrids by establishing C—N covalent bonds through Schiff-base reactions, demonstrating an efficient way for integrating the desired features of both N  $\text{H}_2\text{-UiO-66}$  and Br-COFs [75,76]. Copper nanoparticles (Cu-NPs) were successfully placed into a 2D COF in a synthesis by Khatun et al. [77], resulting in a composite material known as Cu-NPs@COF (Fig. 2 (a)). The copper loading in the composite was found to be 8.26%. The synthesis of 2-oxazolidinones utilizing a  $\text{CO}_2$  balloon in acetonitrile at 50 °C is shown in Fig. 2 (b), which is aided by the presence of Cu-NPs@COF and 1,8-Diazabicyclo[5.4.0]undec-7-ene (DBU) base. The recyclability and reusability of this hybrid material were further examined using 2-oxazolidinones and benzimidazoles. Each catalytic test's isolated Cu-NPs@COF catalyst was used for six cycles of  $\text{CO}_2$  coupling reactions, confirming its maintained catalytic characteristics (Fig. 2 (c)). These findings demonstrate the Cu-NPs@COF catalyst as an effective heterogeneous catalyst capable of retaining its performance over numerous cycles, emphasizing the catalyst's fine heterogeneous character throughout the catalytic process.

Lyu and colleagues [72] investigated the synthesis of COF-609 and subsequently incorporated aliphatic amine groups into it, creating COF-609-Im. They further treated COF-609-Im with  $\text{FeCl}_3$  to produce COF-609-THQ, Im. These three COFs were evaluated for their ability to capture  $\text{CO}_2$  from the air. EDS mapping confirmed a homogenous distribution of elements inside the COFs, with Cl and Im elements successfully doped into COF-609-THQ, respectively (Fig. 2 (d)). The existence of 1D channel-shaped porous structures was verified by PXRD patterns (Fig. 2 (e)), and  $\text{N}_2$  adsorption-desorption isotherms revealed that the highly porous structures of COF-609-Im allowed for  $\text{N}_2$  accessibility, but COF-609 and COF-609-THQ, Im did not (Fig. 2 (f)). Fig. 2 (g) depicts the  $\text{CO}_2$  adsorption isotherms of the three COFs. Notably, despite having the highest surface area and porous structure, COF-609-Im exhibited the lowest  $\text{CO}_2$  adsorption performance. COF-609-THQ, Im, on the other hand, demonstrated a higher adsorption ability than COF-609-Im. This improvement was ascribed to the addition of amine groups in the THQ linkage, which resulted in enhanced polarity. COF-609 had the greatest  $\text{CO}_2$  adsorption ability, indicating that the chemisorption interaction was more conducive for successful  $\text{CO}_2$  collection. While prior research has described the integration of amine [78] or hydroxyl [79] groups into COFs for  $\text{CO}_2$  capture, the study in [72] stresses the need for robust chemisorption in  $\text{CO}_2$  capture by COFs. The study also evaluated the sorption of  $\text{H}_2\text{O}$  vapor on COF-609 and discovered that the quantity of  $\text{H}_2\text{O}$  absorption was sufficient to improve  $\text{CO}_2$  capture (Fig. 2 (h)). This data implies that the humidity in the air did not affect  $\text{CO}_2$  chemisorption, emphasizing the robust nature of COF-609 in preserving its  $\text{CO}_2$  capture capability. Ding and colleagues [80] successfully produced 2D COFs and executed a modification method employing acetate anions in their work. Through a strong interaction between the acetate anion and  $\text{CO}_2$ , the introduction of acetate anions resulted in a significant improvement in  $\text{CO}_2$  collection capacities. This enhancement outperformed the performance of the unmodified pristine 2D COFs. The results of this study offered solid evidence for the usefulness of the channel-wall engineering technique in changing COFs to reach extraordinary amounts of  $\text{CO}_2$  collection. Sharma and colleagues [81] synthesized COFs with slipped and eclipsed structures and tested their performance in  $\text{CO}_2$  collection and  $\text{CO}_2/\text{H}_2$  separation. The slipping COFs had an impressive  $\text{CO}_2$  sorption capacity of 5.8 mol/kg and a  $\text{CO}_2/\text{N}_2$  separation selectivity of 197 at 298 K at 1 bar pressure. These levels much exceeded those observed in the eclipsed COFs. As a result, the slipping COFs proved to be effective materials for  $\text{CO}_2$  collection and separation from gas mixtures. Tz-COFs and Cz-COFs were also produced utilizing benzobisthiazole and carbazole monomers, respectively [82]. These COFs exhibited outstanding  $\text{CO}_2$  adsorption capabilities, with Tz-

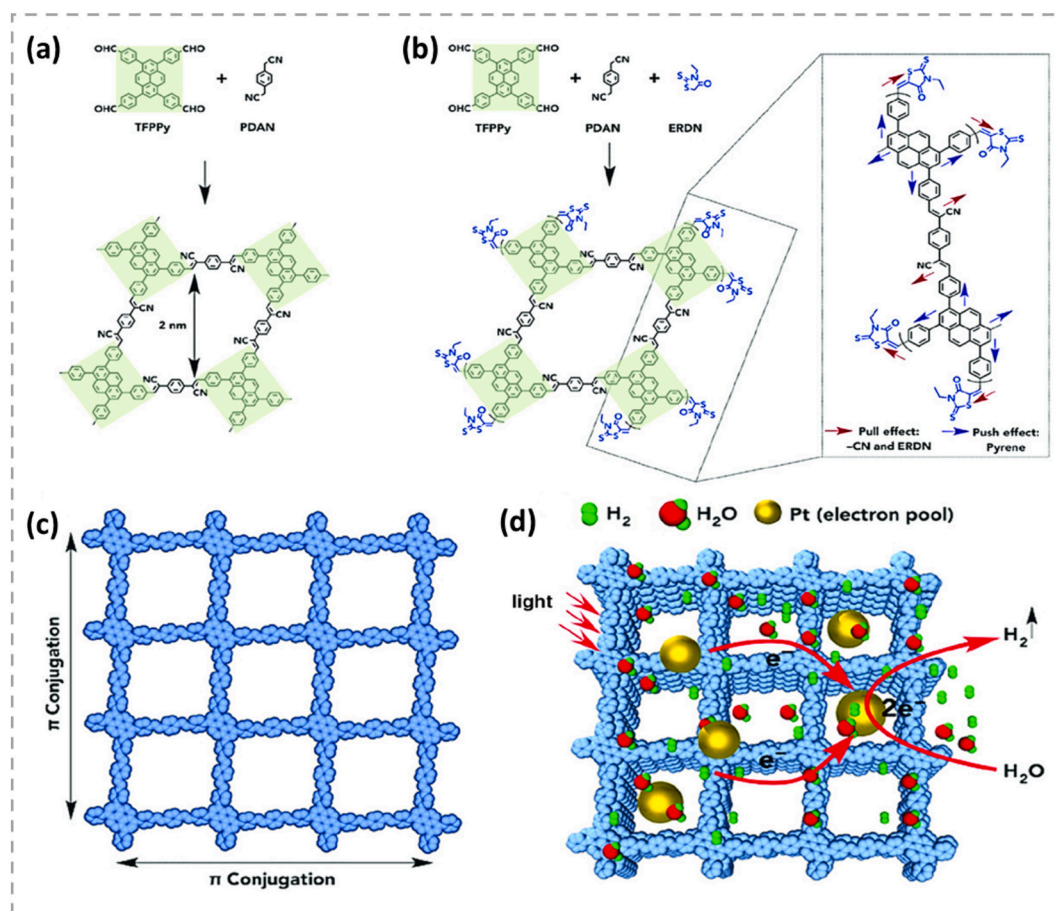
COFs and Cz-COFs reaching 15% wt. and 11% wt., respectively. Furthermore, they displayed great selectivity in extracting  $\text{CO}_2$  from  $\text{N}_2$  and demonstrated outstanding recyclability [82]. Liu et al. [83] created a hydrazone-based COF with high porosity and a surface area of  $1501 \text{ m}^2 \text{ g}^{-1}$ . The COF was created by condensing 2,5-dimethoxy-terephthalohydrazone with 1,3,5-triformyl-benzene using the solvothermal process, resulting in a highly crystalline and chemically stable structure. This COF material showed tremendous promise as a reusable photocatalyst for cross-dehydrogenative coupling reactions involving tetrahydroisoquinolines and nucleophiles. Under solvothermal conditions, Zhi et al. [84] successfully synthesized COF-JLU5 by condensing 1,3,5-tris-(4-aminophenyl)triazine with 2,5-dimethoxyterephthalaldehyde. COF-JLU5 exhibited remarkable properties, including a specific surface area (SBET) of  $1632 \text{ m}^2 \text{ g}^{-1}$  and a pore size of 2.7 nm. This COF was then employed as a heterogeneous photocatalyst for facilitating aerobic CeH functionalizations of N-aryltetrahydroisoquinolines. Wang and colleagues [85] reported for the first time on the photocatalytic properties of extremely stable COFs (LZU-190, LZU-191, and LZU-192) based on benzoxazole. The incorporation of benzoxazole moieties into these p-conjugated metal-free photocatalysts helped to stabilize the COF structure, resulting in a considerable decrease in the optical band gap. As a result, the materials were more sensitive to visible light. These COFs were formed in a reversible/irreversible cascade, starting with the reversible creation of imine bonds and ending with the irreversible formation of benzoxazole rings. The use of irreversible benzoxazole rings throughout the frameworks led to better stability of the synthesized COFs over imine-linked COFs. Surprisingly, even under harsh circumstances, these benzoxazole-based COFs displayed excellent stability. They preserved structural integrity after three days of boiling water and exposure to pure trifluoroacetic acid, 9 M HCl, or NaOH, demonstrating their toughness. These discoveries pave the way for the practical implementation of these very stable COFs in a variety of photocatalytic processes.

Meanwhile, the physicochemical stability of COF connections plays a crucial role in influencing the efficiency of the photocatalytic process. A pertinent illustration is the remarkable stability exhibited by the ultra-stable benzoxazole-linked LZU-191, which sustained long-term photocatalytic activity in the oxidative hydroxylation of aryl boronic acid. In contrast, the imine-linked COF-LZU1 suffered structural degradation during the reaction, attributed to the comparatively lower stability of the imine linkage [85]. To optimize their photocatalytic activity, COFs require well-defined structures with exceptional crystallinity, which enhances charge separation/migration and pore accessibility. Achieving these attributes depends on the use of precise synthetic techniques, emphasizing the importance of appropriate methodologies in the design and development of COFs with improved photocatalytic properties. Recent advancements have enabled the synthesis of 2D COFs with high crystallinity under diverse conditions, thanks to the “two in one” approach that involves dual organic derivatization of building blocks [86]. Another type of COF used as a photocatalyst is the 2D fully conjugated COFs based on C—C linkages. These COFs differ from others due to the reduced reversibility of the C—C bonding process, leading to slightly lower crystallinity [87]. However, they offer extraordinary stability and efficient electron transport, which minimizes the loss of excitation energy at nitrogen atoms caused by lone pair electrons. An excellent case is the  $\text{sp}^2$  c-COF developed by Jiang and colleagues, which represents a fully conjugated COF (Fig. 3 (a–c)). This COF demonstrated remarkable chemical stability, maintaining its crystalline structure even after a 7-day exposure to concentrated hydrochloric acid (12 M) and aqueous sodium hydroxide solution (14 M).

Furthermore, when platinum was utilized as a co-catalyst and TEOA was used as a sacrificial electron donor ( $>420 \text{ nm}$ ), it produced hydrogen at a steady rate of  $1360 \text{ mol g}^{-1} \text{ h}^{-1}$ . The amorphous  $\text{sp}^2$  c-CMP, on the other hand, only attained a hydrogen evolution rate of  $140 \text{ mol g}^{-1} \text{ h}^{-1}$  [88]. To some degree, the difference in catalytic activity between  $\text{sp}^2$  and c-COF and amorphous  $\text{sp}^2$  c-CMP underlined the



**Fig. 2.** (a) The Cu-NPs@COF undergoes a synthetic procedure. (b) Cu-NPs@COF catalytically synthesizes oxazolidinone and benzimidazole by fixing CO<sub>2</sub>. (c) The capability of Cu-NPs@COF to be reused is demonstrated [71]. (d) The characteristics of Cu-NPs@COF are examined through scanning electron micrographs and elemental maps. (e) The PXRD patterns of COF-609-Im, COF-609-THQ, Im, and COF-609, along with (f) N<sub>2</sub> sorption isotherms at 77 K and (g) single-component CO<sub>2</sub> isotherms at 25 °C are analyzed. (h) The single-component H<sub>2</sub>O isotherm of COF-609 at 25 °C is also studied. The zoomed-in view of the PXRD pattern of COF-609-Im with low-intensity reflections is provided as an inset in panel (e). Similarly, the inset in panel (g) showcases a closer look at the adsorption branch of COF-609 at 0–1 mbar to highlight the uptake at the relevant pressure for DAC [72]. Reproduced through Copyright © permission.



**Fig. 3.** (a) A visual representation of the synthetic process for  $sp^2c$ -COF is provided. (b) The diagram depicts the synthesis of  $sp^2c$ -COFERDN and highlights the electron donor-acceptor pull-push effects on the 2D frameworks of  $sp^2c$ -COFERDN. (c) The reconstructed 2D layers of  $sp^2c$ -COF demonstrate outstanding conjugation in both the x and y directions. (d) A schematic illustration showcases the photocatalytic HER occurring over  $sp^2c$ -COF [87]. Reproduced through Copyright © permission.

necessity of crystallinity for COFs utilized in photocatalysis. When electron-deficient 3-ethylrhodanine (ERDN) was used as a final stage group during the synthesis of  $sp^2c$ -COF, the  $sp^2c$ -COFERDN (Fig. 3 (d)) demonstrated a 1.6% higher hydrogen production rate of  $2120 \text{ mol g}^{-1} \text{ h}^{-1}$  with the same experimental conditions as the unmodified  $sp^2c$ -COF ( $1360 \text{ mol g}^{-1} \text{ h}^{-1}$ ).

#### 4. Mechanisms of photocatalytic $CO_2$ reduction by COFs

The photocatalytic reduction of  $CO_2$  using COFs is a complex process and its mechanism can therefore be affected by structural variation of COFs and other factors. Nevertheless, a general mechanism for the photocatalytic reduction of  $CO_2$  using COFs can be deduced as follows: (i) Light absorption and charge separation: COFs undergo electron excitation in the  $\pi$ -conjugated system when exposed to light, resulting in the formation of electron-hole pairs. Excited electrons ( $e^-$ ) are transported from the valence band (VB) to the conduction band (CB), while holes ( $h^+$ ) remain in the VB. Later,  $e^-$  migrates to the surface of COF to participate in  $CO_2$  reduction. (ii)  $CO_2$  activation:  $CO_2$  molecules are adsorbed onto the COF surface and activated by forming a complex with a surface functional group or defect. As linear  $CO_2$  molecules are relatively stable, hence a more negative redox potential is required for direct photocatalytic  $CO_2$  reduction. The  $CO_2$  molecule adsorption on the surface perturbs its linear structure, lowering  $CO_2$  LUMO levels and activating the molecule, rendering it more reactive to reduction. (iii) Reduction of  $CO_2$ : The activated  $CO_2$  reacts with  $e^-$  on the COF surface to form a radical intermediate,  $CO_2^{\cdot-}$ , that can be further reduced by

receiving another electron to form  $CO^{\cdot-}$ . Upon reaction with a proton ( $H^+$ ),  $CO^{\cdot-}$  readily reduced to CO and other products. (iv) Water ( $H_2O$ ) oxidation: The  $h^+$  generated during the light absorption process can also participate in the reaction by oxidizing  $H_2O$  adsorbed on the COF surface to give oxygen ( $O_2$ ) and  $H^+$ . (v) Recombination: Excited electrons and holes can recombine instead of participating in  $CO_2$  reduction or  $H_2O$  oxidation, thereby diminishing the overall efficiency of the photocatalytic process. The exact mechanism of the photocatalytic reduction of  $CO_2$  using COFs remains elusive and forms a focused subject of ongoing research. Multiple approaches are employed to enhance the surface adsorption ability of  $CO_2$  molecules on the photocatalyst, including incorporating surface defects, introducing a co-catalyst, and widening the surface area, as discussed in the earlier section. In general, three distinct mechanisms have been proposed for the photocatalytic reduction of  $CO_2$  by COFs, as illustrated in Fig. 4. First, the effective separation of photogenerated charge carriers—electrons and holes—is essential, as their pathways determine their availability for  $CO_2$  reduction. Second, the presence of catalytic active sites within the COF structure plays a vital role. These active sites, which may include functional groups or metal centers, are vital in the activation and conversion of  $CO_2$  molecules. Lastly, the formation of heterojunctions is considered, where integrating COFs with other semiconductors can substantially improve charge separation and enhance the overall efficiency of the photocatalytic process.

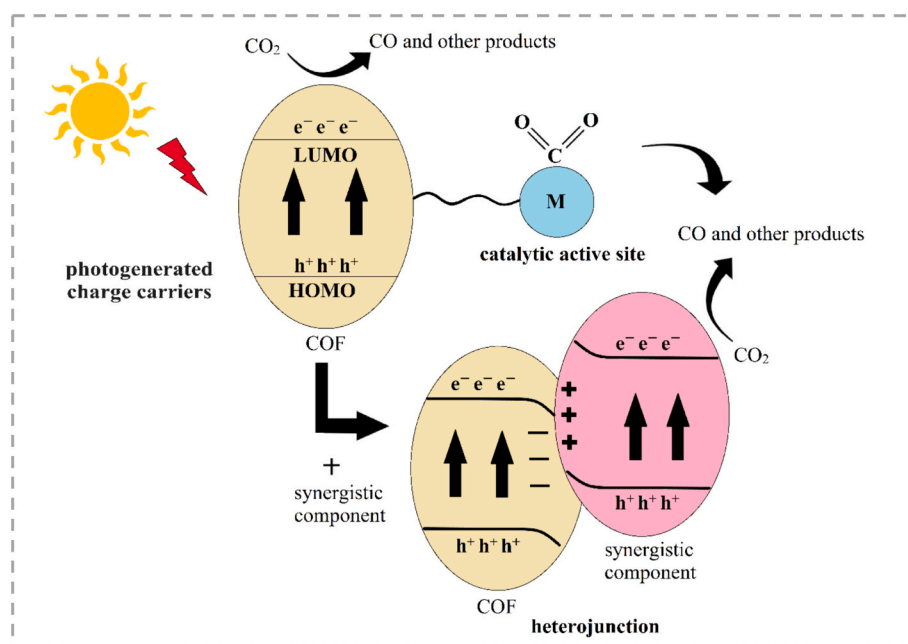


Fig. 4. Proposed mechanisms of photocatalytic reduction of CO<sub>2</sub> utilizing COFs.

#### 4.1. Photogenerated charge carriers

The donor-acceptor approach, which involves incorporating electron-donating and electron-accepting units as knots and linkers, has been demonstrated as a reliable method for constructing photocatalytic COFs [89]. In the usual photoexcitation scenario of COFs, electron-hole pairs are generated upon sunlight exposure, initiating an electron transfer process from the donor to the acceptor. This process creates a CB electron at the acceptor site and a VB hole at the donor site. Subsequently, the excited electrons and holes undergo transfer within the COF structure by hopping between donor and acceptor units, respectively. The dispersion of these units within the COF lattice results in the formation of numerous heterojunctions, thereby enhancing the charge separation efficiency of the system.

Following the first study of COFs for the photocatalytic reduction of CO<sub>2</sub> contributed by Yadav et al. [90], elucidation of the mechanisms involved in the photocatalytic reduction of CO<sub>2</sub> using COFs forms a focus of current research as an initiative to improve and explore the opportunities to fully utilize the potential of COFs in this area. In 2018, Fu et al. studied two azine-linked 2D COFs, namely ACOF-1 and N<sub>3</sub>-COF, prepared from the condensation of hydrazine hydrate and 1,3,5-triformylbenzene (TFB) or 2,4,6-tris(4-bromophenyl)-1,3,5-triazine (N<sub>3</sub>-Ald), respectively [91]. The authors investigated the potential of these materials as photocatalysts for the reduction of CO<sub>2</sub> with H<sub>2</sub>O under visible light irradiation. The large HOMO-LUMO gap (HOMO = highest occupied molecular orbital; LUMO = lowest unoccupied molecular orbital) of either ACOF-1 or N<sub>3</sub>-COF allowed for CO<sub>2</sub> reduction through band gap excitation while enabling significant harvesting of the visible light spectrum, see Fig. 5 (a) for the proposed photocatalytic reduction mechanism. By associating the HOMO with charge-transfer sites for holes, it was deduced that the azine moiety could facilitate efficient hole quenching via hydrogen bonding interactions with H<sub>2</sub>O, whereas excited electrons from the LUMO energy level could react with adsorbed CO<sub>2</sub> on the COFs surface to produce methanol as the main product, with traces of H<sub>2</sub> and O<sub>2</sub> as by-products; the amount of CH<sub>3</sub>OH formed over N<sub>3</sub>-COF is 13.7 μmol g<sup>-1</sup> in 24 h cf. approximately 8.6 μmol g<sup>-1</sup> for ACOF-1, which is 1.6 times higher than that formed over g-C<sub>3</sub>N<sub>4</sub> as illustrated in Fig. 5 (b). To validate the proposed mechanism, various characterization techniques were employed. For instance, UV-vis diffuse reflectance spectra revealed that both ACOF-1 and N<sub>3</sub>-COF

absorb light in the ultraviolet and blue regions, with an absorption edge at approximately 480–500 nm. This indicates an optical band gap of about 2.6 eV, as calculated using the Kubelka-Munk equation. Photocurrent measurements conducted under visible light irradiation (λ ≥ 420 nm) provided evidence of the transfer of photogenerated carriers. Additionally, CO<sub>2</sub> reduction experiments carried out under visible light irradiation confirmed the photocatalytic activity of the materials, further supporting the proposed mechanism.

A highly stable dioxin-linked COF (HBC-TFPN) prepared using 2,3,10,11,18,19-hexahydroxy-cata-hexabenzocoronene (HBC) and tetrafluorophthalonitrile (TFPN) as electron-donating and accepting building units, as depicted in Fig. 5 (c) for preparation procedure, was reported with prominent photocatalytic activity in CO<sub>2</sub> reduction [92]. The final material featured a wavy 2D lattice that directed the attachment of successive layers in order to align the HBC and TFPN units for efficient charge carrier transport. To study the mechanism of CO<sub>2</sub> reduction, the researchers employed several sophisticated methods and techniques. Theoretical calculations showed that the HOMO and LUMO energy levels of HBC and TFPN suggest a type-II heterojunction alignment in the constructed COF. DFT calculations on HBC-TFPN revealed that the spatial distribution of valence band maximum (VBM) and conduction band minimum (CBM) facilitates charge separation after excitation, aiding in efficient photocatalysis. In the study, HBC-TFPN was subjected to visible light irradiation for 2 h with [Ru(bpy)<sub>3</sub>]Cl<sub>2</sub> (bpy = 2,2'-bipyridine) acting as photosensitizer and sodium ascorbate as electron donor, and resulted in the formation of 15.4 μmol g<sup>-1</sup> of CO and 1.4 μmol g<sup>-1</sup> of H<sub>2</sub> as the main products. The photocatalytic CO<sub>2</sub> reduction process is attributed to a photosensitized mechanism as it was triggered by the excitation of [Ru(bpy)<sub>3</sub>]<sup>2+</sup>. As the CBM of HBC-TFPN (-0.66 V vs normal hydrogen electrode (NHE)) is located between the LUMO of [Ru(bpy)<sub>3</sub>]<sup>2+</sup> (-1.26 V NHE) and the equilibrium potential of CO<sub>2</sub>/CO conversion (E(CO<sub>2</sub>/CO) = -0.53 V vs NHE), this enables the CBM to readily accept the excited electron from [Ru(bpy)<sub>3</sub>]<sup>2+</sup> and transport it to CO<sub>2</sub>. The updated energy level diagram of the photocatalytic CO<sub>2</sub> reduction system is shown in Fig. 5 (d). It has been observed that HBC-TFPN exhibits high activity in the reaction due to its efficient charge carrier transport. The cyano group on the TFPN linker is believed to be the active site for CO<sub>2</sub> reduction, attributed to its strong affinity for CO<sub>2</sub> and the localization of the accepted electron by HBC-TFPN, as suggested by the spatial distribution of the CBM. Notably,





photocurrent measurements under visible light irradiation reveal that HBC-TFPN generates a rapid on/off photocurrent with a density of 300 nA cm<sup>-2</sup>, indicating efficient kinetics of photogenerated charge carriers.

A recent study investigated the use of a  $\beta$ -ketoenamine-based COF, TpBb-COF, as a photocatalyst for the conversion of CO<sub>2</sub> and H<sub>2</sub>O into CO and O<sub>2</sub> under visible-light irradiation without the use of photosensitizers or sacrificial agents [93]. The results showed that at a CO<sub>2</sub> concentration of 30%, TpBb-COF produced CO at a rate of 89.9  $\mu\text{mol g}^{-1} \text{h}^{-1}$  at 80 °C, surpassing the rate of 52.8  $\mu\text{mol g}^{-1} \text{h}^{-1}$  observed in pure CO<sub>2</sub> (Fig. 5 (e)). The above suggests that low concentrations of CO<sub>2</sub> are more favourable for the process. To gain insights into the mechanism of photocatalytic CO<sub>2</sub> reduction by TpBb-COF, updated quantum chemical calculations were conducted. DFT was utilized to optimize the ground state geometry of the TpBb-COF model. Following this, electrostatic potential (ESP) and orbital composition analyses were performed. The ESP analysis offered valuable information regarding the charge distribution within the molecule, while the orbital composition analysis elucidated the electronic transitions that occur upon light excitation. Significantly, the orbital composition analysis identified electron transfer from the benzothiazole ring to the cyclohexanetrione moiety during excitation. Based on these findings, an intrinsic mechanism for photocatalytic CO<sub>2</sub> reduction and H<sub>2</sub>O oxidation over TpBb-COF was proposed, as depicted in Fig. 5 (f). When TpBb-COF is exposed to visible light, it absorbs photons due to the appropriate band gap and becomes excited. H<sub>2</sub>O is first adsorbed through a hydrogen bond, and the excited electrons are transferred from the HOMO centre to the LUMO centre to generate electron-hole pairs, which move to the active site that adsorbs CO<sub>2</sub>. The CO<sub>2</sub> reacts with the adsorbed H<sub>2</sub>O to produce HO-HOCO, which loses OH to form HOCO. HOCO then decomposes into CO and OH. The catalytic system later obtains electrons from H<sub>2</sub>O and maintains charge balance by oxidizing H<sub>2</sub>O using photogenerated holes. In the absence of H<sub>2</sub>O, however, the CO<sub>2</sub> reduction efficiency of TpBb-COF is extremely low. The authors suggest that TpBb-COF has a greater preference for the adsorption of H<sub>2</sub>O, thereby promoting the adsorption and reduction of CO<sub>2</sub>.

The motivation to design stable COFs that utilize H<sub>2</sub>O as a source of hydrogen and electrons for converting CO<sub>2</sub> into valuable products through photocatalysis led Yu et al. to develop COFs incorporating 4-carboxyl-quinoline linkages [94]. The authors demonstrated that modifying COFs with hydrophilic 4-carboxyl-quinoline linkages (QL-COF) instead of imine linkages (LZU1-COF) enhanced their photocatalytic efficiency for CO<sub>2</sub> reduction using H<sub>2</sub>O as an electron donor. QL-COF exhibited a remarkable CO production rate of 156  $\mu\text{mol g}^{-1} \text{h}^{-1}$ , surpassing LZU1-COF by over sixfold (25  $\mu\text{mol g}^{-1} \text{h}^{-1}$ ). This superior performance is attributed to the smaller band gap for QL-COF (2.20 eV) compared to LZU1-COF (2.57 eV), as evidenced by their UV-vis diffuse reflectance spectroscopy (DRS) spectra. This smaller band gap in QL-COF, due to its fully conjugated structure, enhances light utilization in the visible region, increasing the number of photogenerated carriers for driving photocatalytic reactions. Photocurrent and EIS measurements also confirmed superior charge separation in QL-COF (higher photocurrent, lower EIS resistance) compared to LZU1-COF. Additionally, PL and TRFDS confirmed less charge recombination (weaker PL intensity) and longer charge carrier lifetime (longer TRFDS) in QL-COF, indicating more opportunities for photocatalysis. Additionally, the *in situ* diffuse reflectance infrared spectroscopy (DRIS) performed revealed the CO<sub>2</sub> photoreduction pathway. Peaks confirmed the efficient capture of H<sub>2</sub>O and CO<sub>2</sub> via -COOH and quinoline groups in QL-COF. Under irradiation, new peaks indicated the formation of \*COOH as the key intermediate.

The proposed mechanism for the photocatalytic reduction of CO<sub>2</sub> with H<sub>2</sub>O over QL-COF, illustrated in Fig. 5 (g), involves the strong binding interaction between hydrophilic -COOH groups and H<sub>2</sub>O molecules. When exposed to irradiation, an electron in QL-COF is excited from the VB to the CB, leaving behind a h<sup>+</sup> in the VB. The adsorbed H<sub>2</sub>O molecule on QL-COF accepts the h<sup>+</sup> and produces a hydrogen ion (H<sup>+</sup>) and O<sub>2</sub>. Meanwhile, the adsorbed CO<sub>2</sub> molecule captures an h<sup>+</sup> and

electron to form an intermediate, COOH\*. COOH\* then captures another H<sup>+</sup>/e<sup>-</sup> pair and undergoes dehydration to produce adsorbed CO, which finally escapes from the surface of QL-COF, releasing free CO. Comparing the reported featuring COFs photogenerated charge carriers' mechanism, QL-COF is by far the most effective COF as shown in Table 1. It exhibits superior photocatalytic performance at a CO production rate of 156  $\mu\text{mol g}^{-1} \text{h}^{-1}$  at a surface area of 209 m<sup>2</sup> g<sup>-1</sup>, as compared to other COFs that yield products such as CH<sub>3</sub>OH or CO within a considerably narrower range of 8.6 to 89.9  $\mu\text{mol g}^{-1} \text{h}^{-1}$ .

#### 4.2. Catalytic active sites

The efficiency of photocatalytic CO<sub>2</sub> reduction with COFs is limited by rapid electron-hole recombination and the need for more active sites. To address this, COFs with heteroatoms and unique microenvironments can be used as functional platforms for anchoring metal complexes to function as catalytically active sites. A bipyridine-based COF, namely COF-TVBT-Bpy, was synthesized by condensing 2,4,6-tri(4-vinylbenzoyl)-s-triazine (TVBT) with 2,2'-bipyridine-5,5'-diamine (Bpy-NH<sub>2</sub>), and Co ion was anchored into COF to produce Co@COF-TVBT-Bpy as a photocatalyst [95]. The marked decrease in PL intensity of Co@COF-TVBT-Bpy and a substantially shorter average fluorescence lifetime ( $\tau = 2.5$  ns), when compared to COF-TVBT-Bpy ( $\tau = 6.5$  ns), suggest that the incorporation of Co ions effectively suppresses the recombination of photogenerated electron-hole pairs. Having [Ru(bpy)<sub>3</sub>]Cl<sub>2</sub>·6H<sub>2</sub>O as a photosensitizer and triethanolamine (TEOA) as a sacrificial agent, Co@COF-TVBT-Bpy showed remarkable performance in visible light-driven reduction of CO<sub>2</sub> to syngas at a production rate of 2291.1  $\mu\text{mol g}^{-1} \text{h}^{-1}$  and a CO/H<sub>2</sub> ratio of approximately 1:1, as shown in Fig. 6 (a). To elucidate the mechanism behind the enhanced photocatalytic CO<sub>2</sub> reduction of Co@COF-TVBT-Bpy compared to COF-TVBT-Bpy, various advanced methods and techniques were employed. PL and time-resolved fluorescence decay measurements indicated a significant decrease in the recombination of light-induced electron-hole pairs within Co@COF-TVBT-Bpy. This reduction in recombination leads to more efficient charge utilization during the reduction process, contributing to its superior performance.

Further confirmation came from transient photocurrent response and electrochemical impedance spectroscopy (EIS) measurements. Co@COF-TVBT-Bpy exhibited a stronger photocurrent response and lower impedance, indicating enhanced transfer of these charges. Additionally, *in situ* DRIFTS provided valuable insights into the interactions of Co@COF-TVBT-Bpy with CO<sub>2</sub>. The formation of chemical species, including carbonate species, formate, and a crucial intermediate COOH\*, was observed. The intensity of these peaks increased with irradiation time, confirming the chemisorption of CO<sub>2</sub> on the surface of COFs. The electron transfer pathway during CO<sub>2</sub> reduction was also studied via quantum chemical calculations. The calculations suggest a specific sequence: photogenerated electrons first move from the TVBT moiety to the Bpy-NH<sub>2</sub> moiety and then to the Co-active sites. These Co sites then facilitate the reduction of both CO<sub>2</sub> and H<sub>2</sub>O molecules. The mechanism is therefore proposed involving photogenerated electrons moving from triazine and benzene ring-occupied (HOMO) to bipyridine and Co centre-unoccupied (LUMO) orbitals. Initially, Co<sup>II</sup> receives photoelectrons and turns into Co<sup>I</sup> species, which adsorbs CO<sub>2</sub> or H<sup>+</sup> at the active site, and CO and H<sub>2</sub> are generated through two hydrogenation steps in distinctive pathways. In the first hydrogenation step, an intermediate COOH\* is generated, which is later converted to CO and H<sub>2</sub>O through the second hydrogenation step, as depicted in Fig. 6 (b). On the other hand, in the pathway of H<sub>2</sub> generation, H<sub>2</sub> was generated through the hydrogenation step and acceptance of photogenerated electrons. Sacrificial agents play a crucial role in this system by consuming the holes in the photosensitizer, thereby maintaining the charge balance within the photocatalytic system.

In a recent study, Gong et al. [96] incorporated [Ru(bpy)<sub>3</sub>]<sup>2+</sup> into the framework of cobalt porphyrin (Co-Por)-based COF (COF-Bpy-Co),

**Table 1**A summary of photocatalytic reduction of CO<sub>2</sub> utilizing COFs.

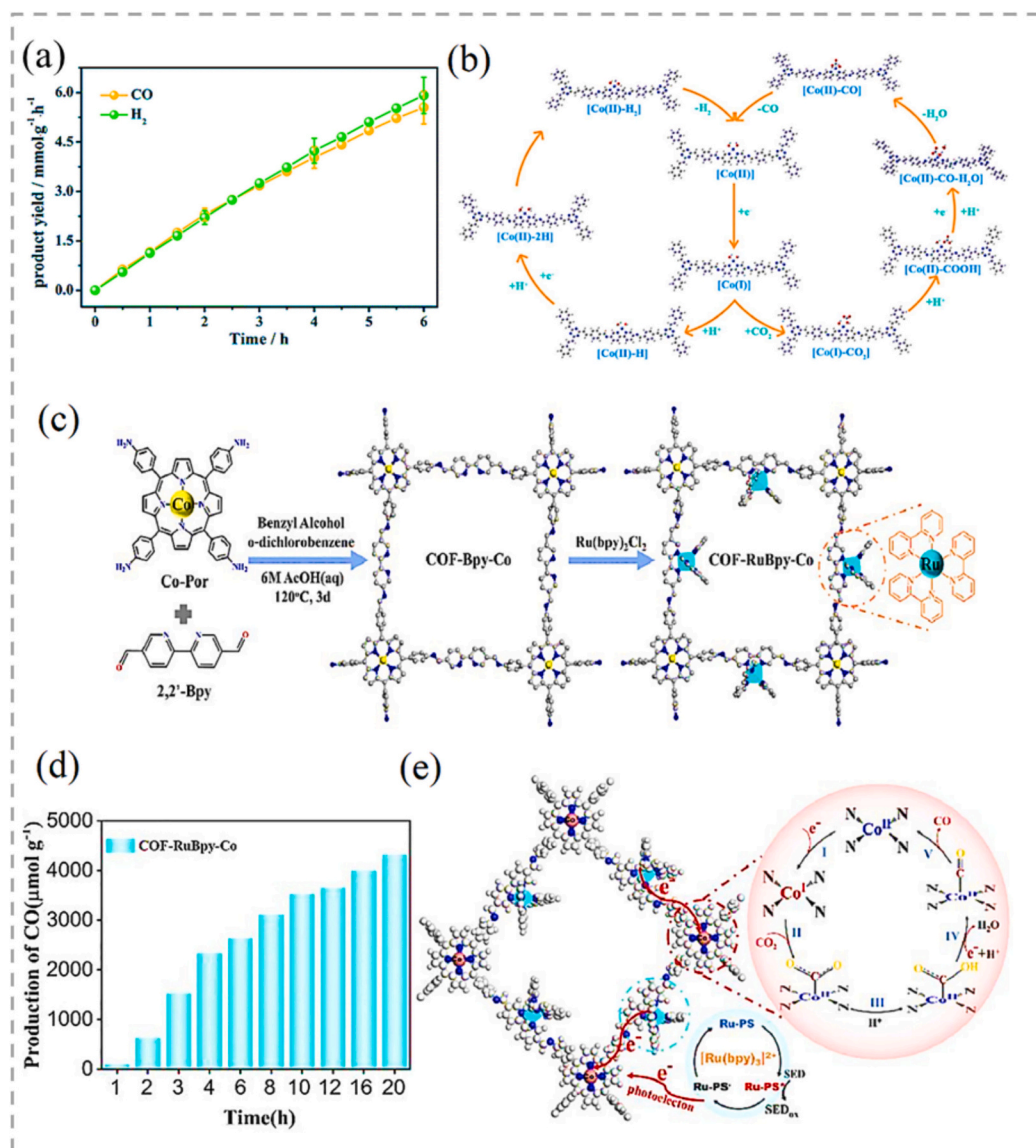
Catalyst	Metal / Synergistic Material	Additive(s)	Products*	Surface Area (m <sup>2</sup> g <sup>-1</sup> )	Yield	Ref.
<b>Photogenerated charge carriers</b>						
ACOF-1	–	–	CH <sub>3</sub> OH (H <sub>2</sub> and O <sub>2</sub> )	1053	8.6 μmol g <sup>-1</sup> in 24 h	[91]
N3 – COF	–	–	CH <sub>3</sub> OH (H <sub>2</sub> and O <sub>2</sub> )	1412	13.7 μmol g <sup>-1</sup> in 24 h	[91]
HBC-TFPN	–	[Ru(bpy) <sub>3</sub> ]Cl <sub>2</sub> and sodium ascorbate	CO and H <sub>2</sub>	681	CO: 15.4 μmol g <sup>-1</sup> H <sub>2</sub> : 1.4 μmol g <sup>-1</sup> in 2 h 89.9 μmol g <sup>-1</sup> h <sup>-1</sup> (under photocatalytic condition of 30% CO <sub>2</sub> )	[92]
TpBb-COF	–	–	CO (H <sub>2</sub> )	913.56	52.8 μmol g <sup>-1</sup> h <sup>-1</sup> (under pure CO <sub>2</sub> )	[93]
LZU1-COF	–	–	CO (CH <sub>4</sub> )	172	25 μmol g <sup>-1</sup> h <sup>-1</sup>	[94]
QL-COF	–	–	CO (CH <sub>4</sub> )	209	156 μmol g <sup>-1</sup> h <sup>-1</sup>	[94]
<b>Catalytic Active Sites</b>						
Co@COF-TVBT-Bpy	Co	[Ru(bpy) <sub>3</sub> ]Cl <sub>2</sub> ·6H <sub>2</sub> O and TEOA	CO and H <sub>2</sub>	342.8	CO: 1132.7 μmol g <sup>-1</sup> h <sup>-1</sup> H <sub>2</sub> : 1158.4 μmol g <sup>-1</sup> h <sup>-1</sup>	[95]
COF-RuBpy-Co	[Ru(bpy) <sub>3</sub> ] <sup>2+</sup>	BIH and TEOA	CO (H <sub>2</sub> )	488	2190 μmol g <sup>-1</sup> in 4 h	[96]
Ni@TPHH-COF	Ni	[Ru(bpy) <sub>3</sub> ]Cl <sub>2</sub> and TEOA	CO and H <sub>2</sub>	654	CO: 1270 μmol g <sup>-1</sup> h <sup>-1</sup> H <sub>2</sub> : 10 μmol g <sup>-1</sup> h <sup>-1</sup>	[97]
DQTP COF-Co	Co	[Ru(bpy) <sub>3</sub> ]Cl <sub>2</sub> ·6H <sub>2</sub> O and TEOA	CO (HCOOH)	195.92	1020 μmol h <sup>-1</sup> g <sup>-1</sup>	[98]
DQTP COF-Zn	Zn	[Ru(bpy) <sub>3</sub> ]Cl <sub>2</sub> ·6H <sub>2</sub> O and TEOA	HCOOH (CO)	345.57	152.5 μmol h <sup>-1</sup> g <sup>-1</sup>	[98]
Co-PI-COF	Co	TEOA	HCOO <sup>-</sup>	22	50 μmol g <sup>-1</sup> h <sup>-1</sup>	[99]
CoNi–COF-3	Co and Ni	[Ru(bpy) <sub>3</sub> ]Cl <sub>2</sub> ·6H <sub>2</sub> O and TEOA	CO (H <sub>2</sub> and CH <sub>4</sub> )	NA	2567 μmol g <sup>-1</sup> h <sup>-1</sup>	[100]
LaNi-Phen/COF-5	La and Ni-phen	BIH	CO (H <sub>2</sub> )	1326	608 μmol g <sup>-1</sup> h <sup>-1</sup>	[101]
Ni-TpBpy	Ni	[Ru(bpy) <sub>3</sub> ]Cl <sub>2</sub> and TEOA	CO (H <sub>2</sub> )	580	4057 μmol g <sup>-1</sup> in 5 h	[102]
Fe SAS/Tr-COF	Fe	[Ru(bpy) <sub>3</sub> ]Cl <sub>2</sub> ·6H <sub>2</sub> O and TEOA	CO	528.14	980.3 μmol g <sup>-1</sup> h <sup>-1</sup>	[103]
COF-367-Co NSs	Co	[Ru(bpy) <sub>3</sub> ]Cl <sub>2</sub> and ascorbic acid	CO and H <sub>2</sub>	NA	CO: 10162 μmol g <sup>-1</sup> h <sup>-1</sup> H <sub>2</sub> : 2875 μmol g <sup>-1</sup> h <sup>-1</sup>	[104]
Co/CTF-1	Co	TEOA	CO	NA	50 μmol g <sup>-1</sup> h <sup>-1</sup>	[105]
TFBD-COF-Co-SA	Co	[Ru(bpy) <sub>3</sub> ]Cl <sub>2</sub> ·6H <sub>2</sub> O and TEOA	CO (HCOO <sup>-</sup> )	560.65	7400 μmol g <sup>-1</sup> in 5 h	[106]
<b>Synergistic Effects of Different Components</b>						
PI-COF-TT	[Ni(bpy) <sub>3</sub> ] <sup>2+</sup>	TEOA	CO (H <sub>2</sub> )	825	1933 μmol g <sup>-1</sup> in 4 h	[107]
2D CN-COF	2D carbon nitride	–	CO and CH <sub>4</sub>	45.91	CO: 7.08 μmol g <sup>-1</sup> h <sup>-1</sup> CH <sub>4</sub> : 2.37 μmol g <sup>-1</sup> h <sup>-1</sup> 85.8 μmol g <sup>-1</sup>	[108]
β-Ga <sub>2</sub> O <sub>3</sub> /COF	β-Ga <sub>2</sub> O <sub>3</sub>	–	CO	94.620	(max at 12% β-Ga <sub>2</sub> O <sub>3</sub> /COF)	[109]
g-C <sub>3</sub> N <sub>4</sub> (NH)/COF	g-C <sub>3</sub> N <sub>4</sub>	TEOA	CO	59.233	11.25 μmol h <sup>-1</sup> CO: 122.9 μmol g <sup>-1</sup> CH <sub>4</sub> : 34.4 μmol g <sup>-1</sup>	[110]
CTF-1	Cs <sub>2</sub> AgBiBr <sub>6</sub> (CABB)	–	CO and CH <sub>4</sub>	–	(max for 10% CTF-1 composite)	[111]
TTCOF	NH <sub>2</sub> – UiO-66 (Zr)	–	CO (CH <sub>4</sub> )	900	6.56 μmol g <sup>-1</sup> h <sup>-1</sup>	[112]
Tp-Tta COF	101-TiO <sub>2</sub>	TEOA	CO (H <sub>2</sub> )	–	Production rate: 11.6 μmol h <sup>-1</sup>	[113]
TpPa-1	Reduced graphene oxide (rGO)	–	CO	882.4	198.975 μmol g <sup>-1</sup> h <sup>-1</sup>	[115]
TpPa-2-COF	Bi <sub>2</sub> O <sub>2</sub> S	TEOA	CO and CH <sub>4</sub>	528.52	CO: 19.5 μmol g <sup>-1</sup> h <sup>-1</sup> CH <sub>4</sub> : 6.2 μmol g <sup>-1</sup> h <sup>-1</sup>	[114]

\* Bracketed products indicate by-products or appeared in trace amounts.

resulting in the formation of COF-RuBpy-Co, as shown in Fig. 6 (c). This photosystem, in the presence of 1,3-dimethyl-1,3-dihydro-2-phenyl-2H-benzimidazole (BIH) as a sacrificial electron donor (SED) and triethanolamine (TEOA) as a proton acceptor for BIH<sup>•+</sup>, exhibited significantly improved CO<sub>2</sub> capture and photoreduction efficiency compared to a physical mixture system. Fig. 6 (d) demonstrates that under 4 h of light exposure, COF-RuBpy-Co yielded 2190 μmol g<sup>-1</sup> of CO with a selectivity for CO generation over H<sub>2</sub> at 75% and an evolution rate of 547 μmol g<sup>-1</sup> h<sup>-1</sup>. The team employed a range of techniques to comprehensively investigate the photocatalytic reduction mechanism of CO<sub>2</sub> using COF-RuBpy-Co. For instance, electrochemical tests and UV–vis DRS were conducted to assess the feasibility of electron transfer between [Ru(bpy)<sub>3</sub>]<sup>2+</sup> and Co-Por centers, including their oxidation potentials and

band gaps. Differential pulse voltammetry (DPV) confirmed favourable electron transfer from [Ru(bpy)<sub>3</sub>]<sup>2+</sup> to Co-Por units. Further insights were gained through in situ X-ray photoelectron spectroscopy (XPS) under light and dark conditions. Positive shifts in Ru 3p peaks and negative shifts in Co 2p peaks indicated continuous electron acceptance by Co(II) centers from excited [Ru(bpy)<sub>3</sub>]<sup>2+</sup>. DFT calculations corroborated this observation, revealing efficient charge transfer due to favourable charge density distribution patterns and enhanced overlap between molecular orbitals in COF-RuBpy-Co, as shown by the projected density of states (PDOS).

Additionally, femtosecond transient absorption (TA) spectroscopy highlighted the advantage of covalent coupling in COF-RuBpy-Co. Compared to a physical mixture system, COF-RuBpy-Co displayed



**Fig. 6.** (a) Profiles of CO and H<sub>2</sub> generation using Co@COF-TVBT-Bpy as the photocatalyst, (b) proposed photoreduction mechanism on Co@COF-TVBT-Bpy, (c) preparation of COF-Bpy-Co and COF-RuBpy-Co through post-synthesis modification, (d) time-dependent photocatalytic CO production over COF-RuBpy-Co, and (e) proposed mechanism for CO<sub>2</sub> photoreduction over COF-RuBpy-Co. Reproduced through Copyright © permission.

faster recovery of the ground-state bleaching (GSB) signal, signifying optimized dynamic charge transfer. Luminescence studies with Ru(bpy)<sub>3</sub>Cl<sub>2</sub> and increasing amounts of BIH and Co-Por confirmed reductive quenching of photoexcited Ru(bpy)<sub>3</sub>Cl<sub>2</sub> by BIH. In situ diffuse reflectance infrared Fourier transform spectroscopy (DRIFT) monitored reaction intermediates during CO<sub>2</sub> reduction. The presence of COO<sup>-</sup> and \*COOH species was identified, revealing their role as key intermediates in the process. Based on these observations, a reaction mechanism is proposed, as illustrated in Fig. 6 (e). Initially, [Ru(bpy)<sub>3</sub>]<sup>2+</sup> moieties were stimulated and produced excited states [Ru(bpy)<sub>3</sub>]<sup>2+</sup>\* (Ru-PS\*) when exposed to visible light. BIH then reductively quenched the hole of the Ru-PS\* to produce [Ru(bpy)<sub>3</sub>]<sup>1+</sup> (Ru-PS<sup>-</sup>) species and BIH<sup>+</sup>. By accepting a proton from the BIH<sup>+</sup> species, TEOA generates the BI• species and releases another electron to quench another Ru-PS\*. Following the transport of the photoexcited electrons from Ru-PS<sup>-</sup> to the Co-Por center via the π-conjugated skeleton of COF-RuBpy-Co, the CO<sub>2</sub> activated by Co centers generated the intermediates COO<sup>-</sup> and COOH\* before being reduced to CO.

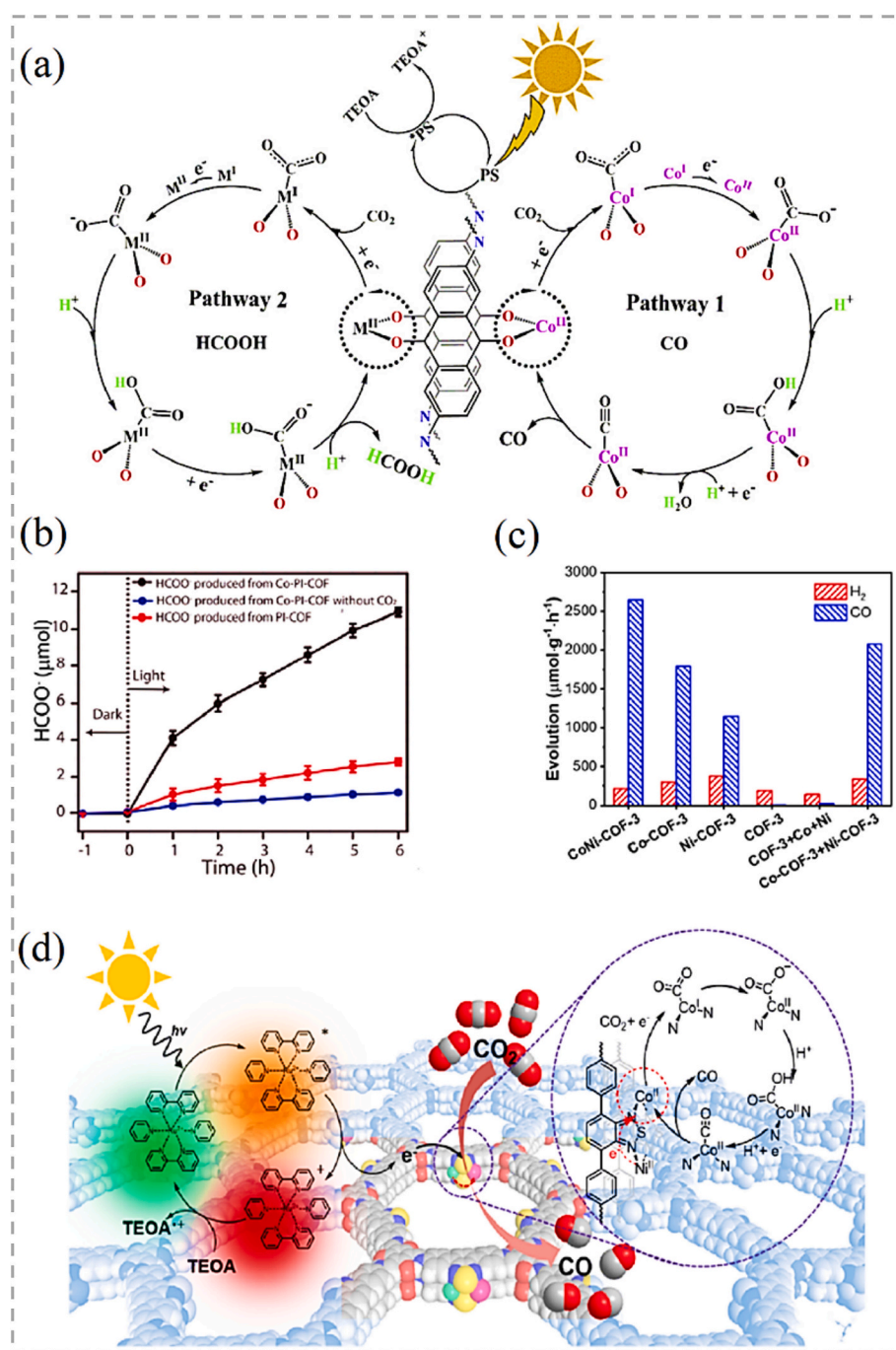
Furthermore, a novel approach for direct photoreduction of CO<sub>2</sub> from flue gas using a layer of Ni<sup>2+</sup>-bonded hydrazone-COF

(Ni@TPHHCOF) has been developed [97]. This system has demonstrated high efficiency for converting flue gas (7% CO<sub>2</sub>) into syngas, with a CO yield of 2.1 mol/kg h<sup>-1</sup> and a conversion efficiency of up to 672 L kg<sup>-1</sup> h<sup>-1</sup> under ideal conditions. On the other hand, under conditions of 100% CO<sub>2</sub>, the primary products detected are CO and H<sub>2</sub>, with yields of 1270 and 10 μmol g<sup>-1</sup> h<sup>-1</sup>, respectively, demonstrating a remarkable CO selectivity of 99.2%. In this study, in situ infrared spectroscopy revealed key steps in the photocatalytic mechanism, i.e. peaks corresponding to adsorbed CO<sub>2</sub> and reduction intermediates (\*COOH and \*CO) confirmed their role in the process. Additionally, new peaks emerged, suggesting an interaction between TEOA and the COF framework as well as intermediates, as revealed by the presence of a peak at ~3350 cm<sup>-1</sup>. DFT calculations further supported these findings. The calculations showed that TEOA interaction with Ni@TPHH-COF and intermediates significantly reduced the Gibbs free energy (ΔG) for CO<sub>2</sub> activation, particularly the rate-determining step (CO<sub>2</sub> → COOH). This suggests that TEOA lowers the energy barrier and stabilizes intermediates, promoting efficient CO<sub>2</sub> reduction.

On the other hand, Photocurrent measurements confirmed efficient photogenerated charge carrier movement under light irradiation, while

UV-Vis diffuse reflectance and Mott-Schottky spectra analysis provided insights into the band structure and semiconducting behaviour of the system. Notably, the catalytic activity exhibited a three-stage response to varying  $\text{CO}_2$  concentrations. Combining photoelectric characterization results with mechanistic studies suggested that the embedded  $\text{Ni}^{2+}$  acts as the active center, with  $\text{CO}_2$  serving a dual role as both a component of the catalytic active site and a reactant. This  $\text{CO}_2$ -dominated bifunctional photocatalytic site, composed of TEOA,  $\text{CO}_2$ , and  $\text{Ni@TPHH-COF}$ , significantly extends electron lifetime, stabilizes reaction intermediates, and lowers the free energy barrier under diluted  $\text{CO}_2$  conditions.

Lu and coworkers reported a series of transition metal ion (TMI)-modified COFs, namely DQTP COF-M ( $\text{M(II)} = \text{Co, Ni or Zn}$ ), prepared based on a 2D anthraquinone-contained COF for electron transport and  $\text{CO}_2$  adsorption [98]. They discovered that TMI can serve as active sites in photocatalytic  $\text{CO}_2$  reduction, and the different TMI types can modify the reduced products. To investigate the intramolecular charge transfer (ICT) behaviour of COFs, PL and time-resolved fluorescence decay techniques were employed. The results indicated significant quenching of PL intensity in DQTP COF-Co compared to DQTP COF, with further reduction when TEOA was introduced. Particularly, the fluorescence life expectancy decreased significantly with TEOA, suggesting suppression



**Fig. 7.** (a) proposed “two-pathway” mechanisms for the photocatalytic reduction of  $\text{CO}_2$  with DQTP COF-M, (b) the amount of formate ions ( $\text{HCOO}^-$ ) generated as a function of irradiation time over Co-PI-COF and PI-COF, along with a control experiment in the absence of a  $\text{CO}_2$  source, (c) catalytic performance of photocatalytic  $\text{CO}_2$  reduction over CoNi-COF-3, Co-COF-3, Ni-COF-3, pure COF-3, and comparative samples, showcasing the evolution rates of CO and  $\text{H}_2$  products, and (d) proposed mechanism for the photocatalytic  $\text{CO}_2$  reduction into CO over CoNi-COF-3 under visible light irradiation. Reproduced through Copyright © permission.

of recombination of the excited state by incorporating Co active sites, where electrons transfer from COF to Co(II) after photoexcitation, and holes are scavenged by TEOA. A “two-pathway” mechanism was proposed in the photocatalytic reduction of CO<sub>2</sub> (Fig. 7 (a)): upon exposure to visible light, [Ru(bpy)<sub>3</sub>]<sup>2+</sup> (PS) undergoes excitation to form the excited species [Ru(bpy)<sub>3</sub>]<sup>2+\*</sup> (PS\*), resulting in the transfer of photo-generated electrons to the DQTP COF-M, followed by the subsequent delivery to the adsorbed CO<sub>2</sub> molecules at the active site. The LUMO level of CO<sub>2</sub> decreases upon adsorption onto the transition metal centre, leading to the formation of a highly reactive bent CO<sub>2</sub> intermediate. The activated CO<sub>2</sub><sup>-</sup> intermediate follows two alternative pathways to yield the final reductive products (HCOOH or CO) through either C–O bond cleavage or proton adduct (COOH<sup>-</sup>). The TEOA sacrificial electron donors scavenge the produced holes in the photosensitizer, ensuring a continuous supply of electrons to the DQTP COF-M for efficient photocatalytic CO<sub>2</sub> reduction. The importance of the quinone oxygen atom in immobilizing metal ions within DQTP COFs was further elucidated through the examination of DATP COF (2,6-diaminoanthracene - 2,4,6-triformylphloroglucinol COF), which shared a similar COF structure but substituted 2,6-diaminoanthraquinone with 2,6-diaminoanthracene, leading to a deficiency of suitable oxygen coordination sites within the COFs and, consequently, a weak capacity for anchoring metal ions.

Furthermore, DFT calculations were performed to understand the interaction between TMIs and the COF, focusing on Zn as a model. The calculations identified the coordination of Zn with interlayer oxygen atoms as the most stable interaction, reinforcing the experimental findings that TMIs primarily anchor to quinone oxygen atoms within the COF. In this study, the highest CO production rate of  $1.02 \times 10^3 \mu\text{mol g}^{-1} \text{h}^{-1}$  (TON = 2.18 and TOF = 0.55 h<sup>-1</sup>) was observed in the case of DQTP COF-Co, while DQTP COF-Zn demonstrated a marked selectivity for formic acid generation (90% over CO) at a rate of  $152.5 \mu\text{mol g}^{-1} \text{h}^{-1}$ , with TON = 0.33 and TOF = 0.08 h<sup>-1</sup>. In the case of DQTP COF-Ni, it is noteworthy that a nearly equal quantity of CO and HCOOH was generated during the photocatalytic CO<sub>2</sub> reduction reaction, suggesting that both of these pathways exhibit approximately equivalent likelihoods for progression.

The improved photocatalytic efficiency in COF upon inclusion of cobalt metal centre was also observed in PI-COF, composed of indigo and metalloporphyrin building units [99]. Briefly, Co metal centres were introduced into the material via post-synthetic metalation of the porphyrin subunits. The material was then assessed for its potential to catalyse the photoreduction of CO<sub>2</sub> into formate (HCOO<sup>-</sup>). The superior performance of Co-PI-COF in comparison to PI-COF can be attributed to several key factors, such as efficient separation of charge carriers, a lower band gap, and robust CO<sub>2</sub> adsorption at the metal centres. Owing to the above, Co-PICOF achieved a notable rate of  $50 \mu\text{mol g}^{-1} \text{h}^{-1}$  of HCOO<sup>-</sup> generated. As shown in Fig. 7 (b), the amount of HCOO<sup>-</sup> produced continuously increased, reaching  $11 \mu\text{mol}$  in 6 h with an average formation rate of  $2 \mu\text{mol h}^{-1}$ . To elucidate the mechanism of action in the photocatalytic reduction of CO<sub>2</sub>, the study initially employed DFT calculations to investigate the donor–acceptor properties and band gap of the COF building blocks. Both the PI-COF and Co-PI-COF exhibited low band dispersion. The PI-COF demonstrated a direct band gap of 0.88 eV with the valence band located on the porphyrin subunit and the conduction band on the isoindigo building block. In contrast, the Co-PI-COF, metallated with Co<sup>2+</sup> ions, had a smaller band gap of 0.56 eV. Optical properties were explored using fluorescence spectroscopy, showing that metallation in Co-PI-COF decreased the relative intensities of the main emission peaks, indicating reduced charge-carrier recombination. The fluorescence lifetime measurements revealed an increase in the third term ( $\tau_3$ ) from 4.34 ns in the PI-COF to 6.79 ns in the Co-PI-COF upon metallation. Photocatalytic performance was assessed by conducting CO<sub>2</sub> photoreduction reactions using the Co-PI-COF as a catalyst in a CO<sub>2</sub>-saturated acetonitrile with TEOA. The product, HCOO<sup>-</sup>, was quantified by ion chromatography, showing significant photocatalytic activity. A mechanism of the catalytic process was

therefore proposed wherein the porphyrins were first reductively quenched upon visible-light absorption, resulting in the formation of the excited CoTAPP\*. The excited species then accepted electrons from TEOA to form CoTAPP\*<sup>-</sup>, which ultimately reduced CO<sub>2</sub> to formate at the Co<sup>II</sup> centres. The Co<sup>II</sup> centres acted as both adsorption and activation sites for the CO<sub>2</sub> molecules. In this process, the sacrificial electron donor TEOA played a critical role in completing the photocatalytic cycle and preventing charge recombination in the porphyrin subunits.

Wang and colleagues investigated the incorporation of atomically dispersed dual-metal sites (Co<sup>2+</sup> and Ni<sup>2+</sup>) into the benzothiadiazole-based COF matrix to enhance the photocatalytic performance of COF [100]. The resulting CoNi–COF-3 showed a significantly improved CO evolution rate of up to  $2567 \mu\text{mol g}^{-1} \text{h}^{-1}$  with a selectivity of 92.2% for photocatalytic CO<sub>2</sub> reduction (Fig. 7 (c)), using TEOA as the sacrificial agent and [Ru(bpy)<sub>3</sub>]Cl<sub>2</sub>·6H<sub>2</sub>O as the photosensitizer (PS). The enhanced activity was attributed to the cooperative contribution of Co and Ni active sites. The physical mixture of Co – COF-3 and Ni – COF-3 gave a much lower catalytic activity than the CoNi–COF-3 species, indicating that Co and Ni sites served as predominant catalytic centres. The above is further supported by UV–vis DRS and Mott-Schottky plots, which revealed that incorporating metals (Co and Ni) into the COF structure red-shifted the light absorption edge and narrowed the band gap (1.93–2.35 eV) compared to the pristine CoNi–COF-0. This indicates enhanced visible light absorption and semiconducting behaviour, making them suitable for CO<sub>2</sub> reduction. Notably, the energy band structure diagram confirmed that the conductive band potentials were appropriate for the reduction process. Further analysis focused on charge transfer dynamics, which is crucial for efficient photocatalysis. EIS identified CoNi–COF-3 as having the best charge transfer resistance, indicated by the smallest semicircle in the Nyquist plot. This translates to better separation and transport of charge carriers. Similarly, transient photocurrent measurements showed the strongest photocurrent in CoNi–COF-3, signifying significant electron accumulation due to improved charge transfer. Finally, linear sweep voltammetry (LSV) tests in N<sub>2</sub> and CO<sub>2</sub> atmospheres confirmed the superior CO<sub>2</sub> reduction capabilities of CoNi–COF-3. It displayed the highest current densities in both environments, with a more significant drop in CO<sub>2</sub> compared to N<sub>2</sub>. This observation indicates a preferential reduction of CO<sub>2</sub> over H<sub>2</sub> evolution. A proposed mechanism (Fig. 7 (d)) suggests that upon exposure to visible light, the [Ru(bpy)<sub>3</sub>]<sup>2+</sup> (PS) is excited, leading to the formation of [Ru(bpy)<sub>3</sub>]<sup>2+\*</sup> (PS\*). The excited molecule then transferred electrons to carbonyl groups on COF-3, which led to the formation of [Ru(bpy)<sub>3</sub>]<sup>3+</sup> (PS<sup>+</sup>). The COF facilitated the acceptance and transfer of electrons to Co active sites, which resulted in the reduction of Co<sup>II</sup> to Co<sup>I</sup> species. Adsorbed CO<sub>2</sub> on Co<sup>I</sup> species accepted electrons and protons, leading to the formation of a radical CO<sub>2</sub><sup>-</sup> intermediate. This intermediate then acquired a proton to form COOH intermediates, which later accepted a proton and electron to form CO\* and then desorbed from the catalysts. CO<sub>2</sub> molecules were mainly adsorbed on the Co sites due to their higher adsorbed energy, which was crucial in inhibiting H<sub>2</sub> formation. The strong orbital interaction between Co and Ni atoms influenced the electron distribution of the Co centre, which enhanced the activity of the Co site. Integrating the CoNi–COF-3 with the Ru photosensitizer not only effectively inhibited the recombination of photogenerated charge carriers by providing electron transport pathways but also activated inert CO<sub>2</sub> gas. Finally, TEOA donated one electron to reduce the Ru<sup>3+</sup> (PS<sup>+</sup>) back to the initial Ru<sup>2+</sup> (PS), completing the catalytic cycle.

In a recent study, Zhou and coworkers fabricated an innovative composite material by incorporating the lanthanum nickel phenanthroline (LaNi-Phen) complex into a conjugated boronate-ester-linked covalent organic framework (COF-5) to give LaNi-Phen/COF-5 [101]. The material was designed to enable efficient production and transfer of photoinduced charges through the optically active (La site) and catalytically active (Ni site) centres for photocarrier generation and highly selective CO<sub>2</sub>-to-CO reduction. The study revealed the directional charge transfer between La–Ni double-atomic sites, leading to

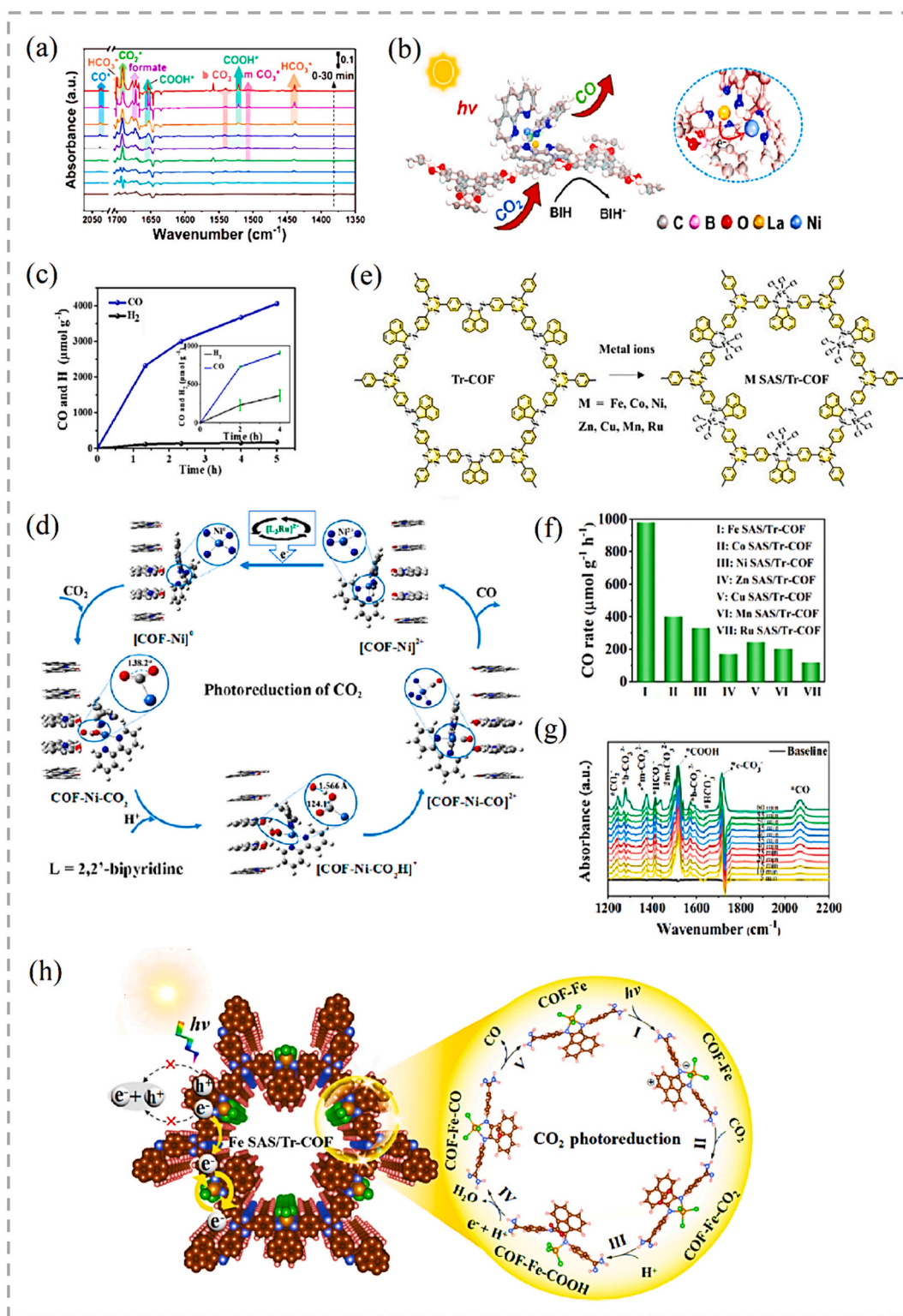
decreased reaction energy barriers of COOH\* intermediate and enhanced CO<sub>2</sub>-to-CO conversion, achieving a 15.2 times enhancement of the CO<sub>2</sub> reduction rate (605.8 μmol g<sup>-1</sup> h<sup>-1</sup>) as compared to a benchmark COF colloid (39.9 μmol g<sup>-1</sup> h<sup>-1</sup>) and an improved CO selectivity (98.2%) in the absence of photosensitizers. In this study, the catalytic activity of LaNi-Phen/COF-5 for CO<sub>2</sub> reduction was systematically evaluated under simulated solar irradiation. Comparative analysis showed that COF-5 colloid, La-Phen/COF-5, and Ni-Phen/COF-5 exhibited significantly lower catalytic activities, indicating the synergistic effect of the combined La and Ni sites. In situ isotope-labeled carbon dioxide (<sup>13</sup>CO<sub>2</sub>) reduction experiments were conducted to trace the origins of the CO<sub>2</sub> reduction products. Mass spectrometry identified three signals, primarily corresponding to <sup>13</sup>CO, confirming the reduction of CO<sub>2</sub> to CO. The reaction mechanism was further elucidated using in situ infrared spectroscopy to analyze adsorbed CO on various catalysts. The La–Ni dual-atom sites showed efficient CO adsorption, facilitating electron transfer and enhancing photoelectric performance. In situ XAFS measurements revealed changes in the oxidation states of the active sites, indicating electron transfer from Ni to CO<sub>2</sub> during adsorption and activation. Dynamic monitoring of surface species and intermediates using in situ DRIFTS identified key intermediates (e.g., CO<sub>2</sub>\*, COOH\*, and CO\*) in the CO<sub>2</sub> reduction pathway, demonstrating the role of LaNi-Phen in facilitating CO<sub>2</sub> adsorption and transformation. The results obtained above led to the proposed process of photocatalytic reduction which originates from the adsorption of CO<sub>2</sub> molecules on the LaNi-Phen/COF-5 surface, followed by the reaction with H<sup>+</sup> and the photogenerated electrons to form the intermediate COOH\*, as shown in Fig. 8 (a). The COOH\* further lead to the appearance of CO\*, and finally, CO is desorbed from the catalyst surface. DFT calculations unveiled the critical role of LaNi-Phen in the selective photoreduction of CO<sub>2</sub> to CO, whereby the appropriate electronic characteristics of the La–Ni dual-atomic sites in LaNi-Phen/COF-5 are responsible for providing the electrons for the CO<sub>2</sub> photoreduction. The HOMO energy level of LaNi-Phen is predominantly situated on Ni-Phen, while the LUMO level is situated on La-Phen, demonstrating that La-Phen is responsible for generating the required driving force for electron migration from the COF-5 colloid to the bimetallic La–Ni sites. In the system, the La atoms act as the optically active centre and electron donor, continuously supplying photogenerated electrons to the LaNi-Phen/COF-5 system, while the COF-5 colloid acts as an electron bridge, directing to Ni atoms for the CO<sub>2</sub> photoreduction. On the other hand, the Ni atoms serve as functional catalytically active sites for the adsorption of activated CO<sub>2</sub>. The charge transfer in the photocatalytic CO<sub>2</sub> reaction over LaNi-Phen/COF-5 is illustrated in Fig. 8 (b).

A new 2,2'-bipyridine-based COF was synthesized using 1,3,5-triformylphloroglucinol and 5,5'-diamino-2,2'-bipyridine [102]. The COF was incorporated with single Ni sites (Ni-TpBpy), and it showed excellent activity in reducing CO<sub>2</sub> to CO (4057 μmol g<sup>-1</sup> in a 5 h reaction) with high selectivity (96%) over H<sub>2</sub> evolution, as depicted in Fig. 8 (c). Even at a reduced CO<sub>2</sub> partial pressure of 0.1 atm, the CO production selectivity was still as high as 76%. The high activity and selectivity were attributed to the synergistic effects of the single Ni catalytic sites and TpBpy. The TpBpy acted as a host for CO<sub>2</sub> molecules and Ni catalytic sites facilitated the activation of CO<sub>2</sub> and inhibited the competitive H<sub>2</sub> evolution. To gain mechanistic insight into the photocatalytic reduction of CO<sub>2</sub> by Ni-TpBpy, CV was employed. The formation of Ni(bpy)<sub>3</sub><sup>2+</sup> was confirmed through the characteristic reduction waves observed upon the successive addition of bpy ligand to Ni(ClO<sub>4</sub>)<sub>2</sub> solution. The CVs of the Ni complex in MeCN/H<sub>2</sub>O solution revealed two irreversible reduction waves under both Ar and CO<sub>2</sub> atmospheres, corresponding to the reduction of Ni ions from Ni<sup>II</sup> to Ni<sup>I</sup> and Ni<sup>I</sup> to Ni<sup>0</sup>. The emergence of a catalytic current under a CO<sub>2</sub> atmosphere after the Ni<sup>I</sup> to Ni<sup>0</sup> reduction wave indicated the involvement of Ni<sup>0</sup> in the electrochemical reduction of CO<sub>2</sub>.

On the other hand, comparative studies using Ni-loaded TpPa (lacking bpy) and Ni-loaded TbBpy (lacking keto moieties) showed

significantly lower activity compared to Ni-TpBpy, emphasizing the importance of both bpy units and keto groups for efficient CO<sub>2</sub> reduction. Furthermore, DFT calculations identified CO<sub>2</sub> adsorption as the rate-limiting step. The presence of the keto unit in TpBpy significantly lowered the energy barrier for the key Ni-CO<sub>2</sub> adduct formation, promoting CO production. Additionally, CO<sub>2</sub> adsorption on Ni-TpBpy was more favourable than on Co-TpBpy, explaining its superior performance. Further calculations revealed a favourable pathway for CO production involving protonation of the Ni-CO<sub>2</sub> adduct followed by steps with low energy barriers. These findings suggest the suitability of Ni-TpBpy for selective CO production. Briefly, the deduced mechanism involves the excitation of the photosensitizer [Ru(bpy)<sub>3</sub>]<sup>2+</sup> upon visible light irradiation. Subsequently, it leads to the transfer of electrons to reduce the coordinated CO<sub>2</sub> molecules on Ni-TpBpy. The affinity of CO<sub>2</sub> on Ni sites over H<sup>+</sup> was crucial for inhibiting H<sub>2</sub> formation. The coordinated CO<sub>2</sub> in COF-Ni-CO<sub>2</sub> exhibited a bending configuration, indicating that CO<sub>2</sub> was activated by single Ni sites, as shown in Fig. 8 (d). The formation of a hydrogen bond between COOH and the keto group promoted the stabilization of the key intermediate, COF-Ni-CO<sub>2</sub>H, leading to enhanced CO<sub>2</sub> reduction. It was confirmed that the single Ni sites in TpBpy were catalytic active sites to coordinate, activate, and reduce CO<sub>2</sub> molecules. The TpBpy not only acted as a host for CO<sub>2</sub> molecules and single Ni sites but also contributed to the catalytic activity and selectivity of CO<sub>2</sub> reduction, in agreement with experimental observations.

Ran and colleagues studied the photocatalytic reduction of CO<sub>2</sub> using a triazine-based COF (SAS/Tr-COF) anchored with single-atom metal sites, such as Fe, Co, Ni, Zn, Cu, Mn, and Ru, with a metal–nitrogen–chlorine bridging structure as depicted in Fig. 8 (e) [103]. Incorporating single metal atoms into the photocatalysts broadens the light response range. It homogenizes atomic metal species, thereby shortening the electron transfer distance and accelerating transfer dynamics to promote efficient CO<sub>2</sub> reduction. Moreover, active metal species, e.g. Fe, maximize atomic utilization and act as highly active sites to activate CO<sub>2</sub> and generate stable intermediate configurations, endowing Fe SAS/Tr-COF with exceptional photocatalytic performance. Fig. 8 (f) demonstrated the superior CO<sub>2</sub> photoreduction performance of Fe SAS/Tr-COF photocatalyst compared to other derivatives studied. The Fe SAS/Tr-COF photocatalyst, loaded with tuneable amounts of atomic Fe species, achieved a remarkable CO generation rate of 980.3 μmol g<sup>-1</sup> h<sup>-1</sup> and a selectivity of 96.4% due to the synergistic effect of the atomically dispersed metal sites and Tr-COF host, which reduces reaction energy barriers for COOH\* intermediate formation and promotes CO<sub>2</sub> adsorption and activation as well as CO desorption. The reduction mechanism involves the participation of abundant metal active sites of Fe SAS/Tr-COF photocatalysts, a Fe–N charge bridge, and effective CO<sub>2</sub> reduction to CO on the catalyst. Notably, Fe SAS/Tr-COFs exhibited suppressed charge recombination compared to Tr-COFs, as evidenced by lower photoluminescence intensity and longer lifetime. This was further confirmed by increased charge separation and photocurrent density observed in surface photovoltage and photoelectrochemical tests. Impedance spectroscopy revealed the fastest interface charge transport in Fe SAS/Tr-COFs while femtosecond transient absorption spectroscopy showed faster decay kinetics in Fe SAS/Tr-COFs, indicating accelerated electron-hole separation. DFT calculations supported this by revealing efficient carrier migration from Tr-COFs to Fe SAS via Fe–N channels. While In-situ DRIFTS confirmed the formation of key intermediates (\*COOH, \*CO<sub>2</sub>, \*HCO<sub>3</sub>, and \*CO) during CO<sub>2</sub> reduction. DFT calculations suggest Fe SAS/Tr-COFs undergo a stepwise hydrogenation process for CO<sub>2</sub> conversion. Adsorbed \*CO<sub>2</sub> reacts with protons to form \*COOH, which further protonates to \*CO. The desorption of \*CO or its protonation to \*CHO determines the final product. The presence of single Fe sites enhances CO<sub>2</sub> adsorption, intermediate stabilization, and CO desorption, leading to selective CO production. Hence, the proposed mechanism involves the following steps: Firstly, the Fe SAS/Tr-COF photocatalysts containing atomically dispersed Fe atoms provide numerous active sites for capturing CO<sub>2</sub>



**Fig. 8.** (a) In-situ DRIFTS spectra collected in the region  $1350\text{--}2070\text{ cm}^{-1}$  for the detection of reaction intermediates in  $\text{CO}_2$  photoreduction over LaNi-Phen/COF-5 under subsequent light irradiation in the presence of  $\text{H}_2\text{O}$ , (b) a schematic illustration of the charge transfer process in the photocatalytic  $\text{CO}_2$  reaction over LaNi-Phen/COF-5, (c) the photocatalytic evolution of CO and  $\text{H}_2$  by Ni-TpBpy under varied  $\text{CO}_2$  pressure conditions (1 atm and 0.1 atm, diluted with Ar, as indicated in the inset) during a 2 h reaction, (d) a proposed reaction mechanism for the photoconversion of  $\text{CO}_2$  into CO on Ni-TpBpy, (e) synthesis process of Fe single-atom sites (SAS) incorporated into Tr-COFs, (f) incorporation of various metal ions into Tr-COFs for  $\text{CO}_2$  photoreduction in a 1 h reaction, and (g) the reaction mechanism for the photocatalytic conversion of  $\text{CO}_2$  to CO over Fe SAS/Tr-COFs. (h) Proposed mechanism for the conversion of  $\text{CO}_2$  to CO using photocatalysis over Fe SAS/Tr-COFs. Reproduced through Copyright © permission.



molecules efficiently (Fig. 8 (g)). Secondly, the formation of a Fe–N charge bridge in Fe SAS/Tr-COFs facilitates rapid electron transfer from Tr-COF units to atomically dispersed Fe centres, leading to long-lasting carrier separation. This additional electron transfer pathway can further improve the photocatalytic efficiency. Lastly, the absorbed CO<sub>2</sub> can be effectively reduced to produce CO on the Fe SAS/Tr-COF catalyst (Fig. 8 (h)).

In a study reported by Liu et al. on the ultrathin COF-367-Co NSs, which were revealed to be 2D COFs, they exhibited remarkable photocatalytic activity for converting CO<sub>2</sub> to CO under visible light irradiation. It gave a high CO production rate of 10,162 μmol g<sup>-1</sup> h<sup>-1</sup> with a selectivity of around 78% [104]. The COF-367-Co NSs acted as heterogeneous catalysts with [Ru(bpy)<sub>3</sub>]Cl<sub>2</sub> as the photosensitizer and ascorbic acid (AA) as the electron donor. To elucidate the mechanism of action in the photocatalytic reduction of CO<sub>2</sub> using COF-367-Co NSs, several control experiments were conducted to reveal the critical roles of each component in CO<sub>2</sub> photoreduction by COF-367-Co NSs. First, the absence of COF-367-Co NSs led to negligible CO production, highlighting its role as a co-catalyst. Secondly, metal-free COF-367 NSs displayed lower CO yield but higher H<sub>2</sub> production compared to COF-367-Co NSs, suggesting Co<sup>2+</sup> in CoPor sites as the active centers. Thirdly, a physical mixture of COF-367 NSs and free Co<sup>2+</sup> ions also exhibited lower activity, emphasizing the importance of the Co and Ni centers in CoPor for optimal performance. Additionally, the system only produced H<sub>2</sub> under N<sub>2</sub>, confirming CO originates from CO<sub>2</sub>. Isotopic labelling with <sup>13</sup>CO<sub>2</sub> further supported this. Delving deeper into the performance of COF-367-Co NSs, PL and ultrafast TA spectroscopy were conducted. In the former, PL spectra revealed a decrease in the intensity and lifetime of the photosensitizer at 606 nm when interacting with COF-367-Co NSs. This suggests an efficient transfer of photogenerated electrons. TA spectroscopy further confirmed these dynamics. Ru(bpy)<sub>3</sub>Cl<sub>2</sub> displayed a bleaching peak at 450 nm, indicating light excitation. Adding the sacrificial agent AA resulted in a new absorption peak at 500 nm, signifying reductive electron transfer. Notably, the TA spectra of the complete system ([Ru(bpy)<sub>3</sub>]Cl<sub>2</sub>, COF-367-Co NSs, and AA) showed the formation of [CoPor]<sup>-</sup> via electron transfer, strongly supporting the proposed CO<sub>2</sub> photoreduction mechanism as outlined below.

In this study, it was proposed the Co atom served as the site for CO<sub>2</sub> adsorption and an energy barrier of 0.47 eV associated with the formation of the adsorbed intermediate COOH\* obtained from DFT calculations represents a potential limiting step in the reduction mechanism; this energy barrier is sufficiently small to enable the reaction to occur at room temperature. On the other hand, the energy barrier for the hydrogen evolution reaction was measured to be 0.74 eV, which is significantly higher than that for CO<sub>2</sub> reduction. This result indicates that COF-367-Co NSs exhibit high selectivity for CO<sub>2</sub> reduction. The proposed mechanism in Fig. 9 (a), revealed that under visible light irradiation, the photosensitizer [Ru(bpy)<sub>3</sub>]<sup>2+</sup> undergoes excitation, followed by electron donation from AA to form [Ru(bpy)<sub>3</sub>]<sup>+</sup>. This species subsequently donates an electron to COF-367-Co NSs, initiating the CO<sub>2</sub>-to-CO conversion process on their surface. The large aspect ratio of the 2D COF-367-Co NSs yields an abundance of highly accessible active sites on their surface, significantly contributing to their enhanced photocatalytic activity in CO<sub>2</sub> reduction towards CO production.

Bi and coworkers revealed the improved photocatalytic efficiency of cobalt-modified covalent triazine-based frameworks (Co/CTFs), with a CO production rate of up to 50 μmol g<sup>-1</sup> h<sup>-1</sup>, which is 44 times higher than the pristine counterpart [105]. This improvement is attributed to the enhanced CO<sub>2</sub> capture capacity, improved visible-light absorption, and efficient charge transfer resulting from cobalt modification. The photocatalytic performances of Co/CTFs were evaluated through the photocatalytic reduction of CO<sub>2</sub> using TEOA as a sacrificial agent. The study reveals that these materials possess effective proton adsorption sites functioning as Lewis base sites, which significantly enhance CO<sub>2</sub> adsorption. The enhanced CO<sub>2</sub> adsorption in Co/CTF-1 is attributed to the nitrogen-rich framework and the affinity of cobalt ions for CO<sub>2</sub>. To understand the optical properties, UV–vis absorption spectroscopy was used, showing that Co/CTF-1 samples had better visible light absorption (450–700 nm) compared to CTF-1, indicating a strong host-guest interaction between the metal and framework. On the other hand, the PL emission intensity of Co/CTF-1 was significantly lower than that of CTF-1, indicating reduced charge carrier recombination. This was further supported by photoelectrochemical measurements, which showed a decreased radius in Nyquist plots and increased transient

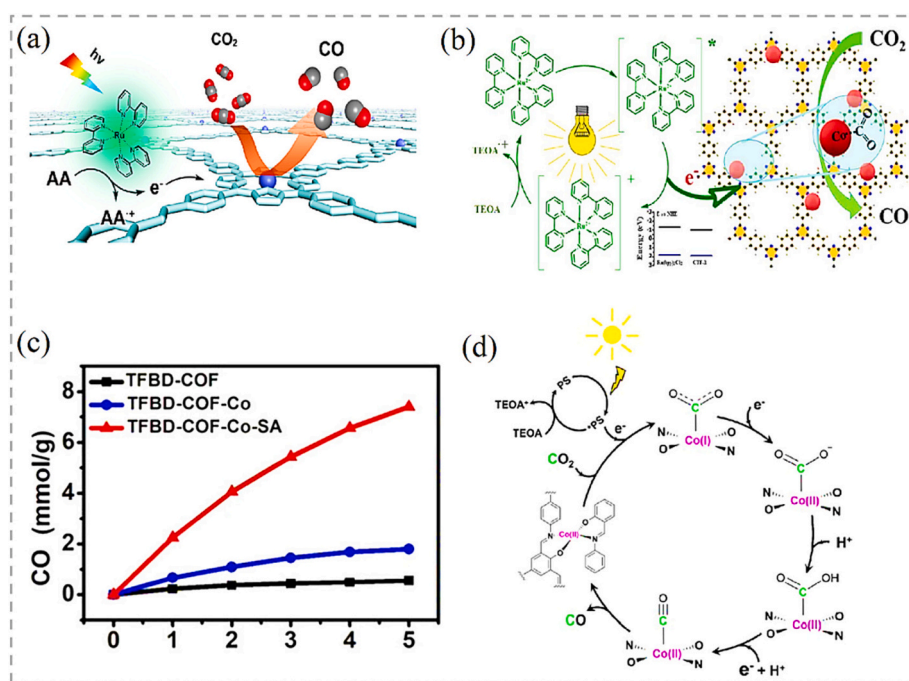


Fig. 9. (a) Elucidates the proposed mechanisms involved in the photocatalytic conversion of CO<sub>2</sub> into CO for (a) COF-367-Co NSs and (b) Co/CTF-1 under visible light, (c) the photocatalytic CO<sub>2</sub>-to-CO activities of TFBD-COF-Co-SA, TFBD-COF-Co, and TFBD-COF, highlighting their comparative performance, and (d) the photocatalytic CO<sub>2</sub> reduction mechanism of TFBD-COF-Co-SA. Reproduced through Copyright © permission.

photocurrent under visible light ( $\lambda \geq 420$  nm), suggesting improved electrical conductivity and prolonged charge carrier lifetime. Electron spin resonance (ESR) spectra of Co/CTF-1 also showed enhanced intensities, indicating more unpaired electrons facilitating the photo-reduction process. Additionally, isotope experiments with  $^{13}\text{CO}_2$  confirmed that the CO produced originated from  $\text{CO}_2$  reduction. A proposed mechanism for the photocatalytic  $\text{CO}_2$  conversion involves the excitation of the photosensitizer  $[\text{Ru}(\text{bpy})_3]^{2+}$  and CTF-1 by visible light, which generates photoinduced electron-hole pairs, as illustrated in Fig. 9 (b). The electrons are then transferred to Co active site to form  $\text{Co}^{\text{I}}$  active species.  $\text{CO}_2$  molecules are adsorbed into CTFs and interact with the photo-reduced Co species to form the transition state  $\text{Co}^{\text{I}}\text{-CO}_2$ , which favours the fixation of  $\text{CO}_2$  in the catalytic reaction. Therefore, introducing cobalt species into CTF-1 harvests more visible-light photons and produces more photogenerated carriers than pristine CTF-1, which are promptly transferred to Co active species. The adsorbed  $\text{CO}_2$  molecules are then reduced to CO through a cascade of redox reactions. The porosity of CTF-1 allows for the accommodation of photosensitizer, sacrificial agent, and  $\text{CO}_2$  molecules, which shortens the photoelectron transport time and distance between CTF-1 and  $\text{CO}_2$ , thus promoting the separation of electron-hole pairs and leads to enhancement of photo-conversion efficiency.

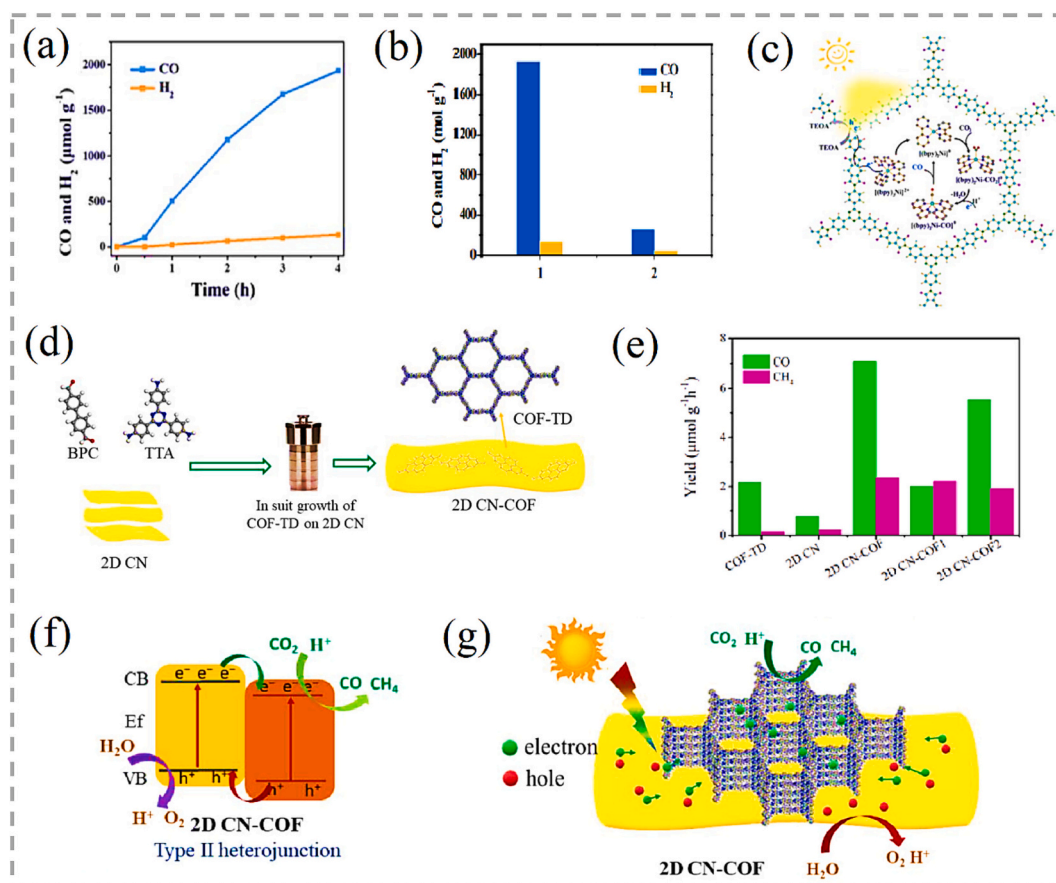
Yang et al. reported the synthesis of a Schiff-base complex-decorated COF for photocatalytic reduction of  $\text{CO}_2$  [106]. In their approach, 3,3',5,5'-Tetraformyl-4,4'-biphenyldiol-COF (TFBD-COF) was incorporated with  $\text{Co}^{2+}$  giving TFBD-COF-Co, which was then coordinated to salicylideneaniline (SA) to produce TFBD-COF-Co-SA. Among the three species evaluated, TFBD-COF-Co-SA exhibits comparatively better performance than TFBD-COF-Co (4.1 times) with excellent photocatalytic  $\text{CO}_2$  reduction activity and stability, with a  $\text{CO}_2$ -to-CO reduction activity of  $7400 \mu\text{mol g}^{-1}$  in 5 h and a 90% selectivity, as shown in Fig. 9 (c). The authors performed a series of experimental and theoretical techniques to elucidate the mechanism of action of the photocatalytic reduction of  $\text{CO}_2$ , which include room-temperature PL experiments on TFBD-COF-Co and TFBD-COF-Co-SA in a  $\text{CO}_2$ -degassed  $\text{CH}_3\text{CN}$  solution containing Ru. These experiments revealed that the quenching of the  $\text{PS}^*$  was due to the photocatalysts, and TFBD-COF-Co-SA showed more efficient photoexcited electron transfer from Ru compared to TFBD-COF-Co. This was evident as the fluorescence emission intensities of Ru decreased more significantly with TFBD-COF-Co-SA. On the other hand, EIS was used to assess charge immigration efficiency, where TFBD-COF-Co-SA demonstrated a smaller semicircular diameter on the Nyquist curves than TFBD-COF-Co, indicating higher charge migration efficiency. Transient photocurrent response characterizations further supported this, showing a significantly higher response intensity for TFBD-COF-Co-SA, suggesting improved separation of photogenerated charges. Additionally, electron paramagnetic resonance (EPR) signals were stronger for TFBD-COF-Co-SA, indicating that coordination of the SA ligand to  $\text{Co}^{2+}$  induced additional free electrons, which correlated with enhanced photocatalytic activities. On top of the above, DFT calculations provided deeper insights into the ligand effects on the  $\text{Co}^{2+}$  centers during  $\text{CO}_2$  photoreduction. The energy pathways for  $\text{CO}_2$ -to-CO reduction on these models indicated that the coordination of two SA ligands in TFBD-COF-Co-SA resulted in a lower energy barrier (0.69 eV) for the rate-limiting step ( $^*\text{COOH}$  formation) compared to TFBD-COF-Co (0.97 eV). The findings suggest an enhanced CO production rate for TFBD-COF-Co-SA. Charge analysis and density of states (DOS) calculations reveal that the Co center in TFBD-COF-Co-SA exhibits stronger binding and increased charge retention, primarily due to back-donation from the SA ligand. This interaction facilitates a delocalized charge distribution, which in turn boosts  $\text{CO}_2$  reduction activity. Cyclic voltammetry (CV) tests conducted under both  $\text{N}_2$  and  $\text{CO}_2$  conditions further elucidate the photocatalytic mechanism. The CV results show a quasi-reversible redox couple under  $\text{N}_2$  and an irreversible reduction wave peak under  $\text{CO}_2$ , highlighting the  $\text{Co}^{\text{II/I}}$  transition as a key driver of  $\text{CO}_2$  reduction. The reduction potential observed was more negative than the  $\text{CO}_2/\text{CO}$

reduction potential, thereby confirming the thermodynamic feasibility of the process. Integrating these results, the proposed photocatalytic mechanism involves the light excitation of the photosensitizer  $[\text{Ru}(\text{bpy})_3]\text{Cl}_2 \cdot 6\text{H}_2\text{O}$ , followed by the oxidative quenching of  $\text{PS}^*$  by TFBD-COF-Co-SA, which drives the reduction of  $\text{Co}^{\text{II}}$  to  $\text{Co}^{\text{I}}$  species (Fig. 9 (d)). The  $\text{Co}^{\text{I}}$  intermediate then combines with  $\text{CO}_2$  and accepts electrons and protons to generate  $\text{Co-COOH}$  intermediates, which finally cleave the C-OH bond to release CO. The formed  $\text{PS}^+$  species are reduced to the original PS by TEOA, completing the photocatalytic cycle.

#### 4.3. Synergistic effects of different components

Efforts are being channelled to enhance the photocatalytic efficiency of COFs by combining them with other materials. In a recent study, Chen et al. demonstrated the improved photocatalytic activity of polyimide COFs (PI-COFs) when paired with  $[\text{Ni}(\text{bpy})_3]^{2+}$  [107]. The single Ni sites within the hexagonal pores of PI-COFs act as active sites for  $\text{CO}_2$  activation and conversion. PI-COFs not only host single Ni sites but also generate and separate charge carriers. The optimized reaction conditions resulted in the production of  $1933 \mu\text{mol g}^{-1}$  CO with 93% selectivity over  $\text{H}_2$  in a 4 h reaction (Fig. 10 (a)) using the most prominent species, PI-COF-TT, prepared from pyromellitic dianhydride (PMDA) and 1,3,5-tris(4-aminophenyl)triazine (TAPT), in combination with  $[\text{Ni}(\text{bpy})_3]^{2+}$ . Notably, PI-COFs with direct impregnation of  $[\text{Ni}(\text{bpy})_3]^{2+}$  showed significantly lower activity than those with in situ formed  $[\text{Ni}(\text{bpy})_3]^{2+}$ , as indicated by the catalytic performance measured in Fig. 10 (b). The assembly of Ni ions and the bpy ligand occurred within the pores of PI-COFs, resulting in the uniform distribution of  $[\text{Ni}(\text{bpy})_3]^{2+}$  in PI-COFs when in situ formed, while the direct impregnation method led to inefficient catalytic activity due to the large molecular volume of  $[\text{Ni}(\text{bpy})_3]^{2+}$  that cannot diffuse effectively into the pores of PI-COFs. The elucidation of the mechanism by which PI-COF-TT promotes  $\text{CO}_2$  reduction relies on various advanced techniques. Isotopic labeling with  $^{13}\text{CO}_2$  confirmed that the product, CO, originates from  $\text{CO}_2$  conversion. UV-vis spectroscopy identified the active catalyst as  $[\text{Ni}(\text{bpy})_3]^{2+}$ . Additional analysis using NMR and HPLC confirmed the absence of byproducts such as  $\text{HCOOH}$  or  $\text{CH}_3\text{OH}$ , highlighting the selectivity of PI-COF-TT towards CO production. Furthermore, a photochromic phenomenon observed under irradiation, coupled with increased electron paramagnetic resonance (EPR) signals upon light illumination, suggested light-induced charge generation. The decrease in EPR signal intensity for  $\text{Ni}@$ PI-COF-TT confirmed the interaction between PI-COF-TT and  $[\text{Ni}(\text{bpy})_3]^{2+}$ . The control experiments conducted and further DFT calculations suggested an initial period for collisional electron transfer from the COF to Ni complexes, leading to the formation of active Ni sites. The selectivity of  $\text{CO}_2$  reduction was therefore attributed to preferential adsorption and activation on these Ni sites. Calculations showed a stronger affinity of  $\text{CO}_2$  towards  $[\text{Ni}(\text{bpy})_2]^0$  compared to  $\text{H}_2\text{O}$ , facilitated by hydrogen bonding interactions with the PI unit. This selective adsorption mechanism ultimately led to enhanced  $\text{CO}_2$  reduction activity and CO selectivity. Overall, the proposed mechanism for the selective photoreduction of  $\text{CO}_2$  over PI-COF-TT with molecular Ni complexes, as shown in Fig. 10 (c), involves the photogeneration of electron-hole pairs upon light illumination, reductive quenching of the holes by TEOA, and subsequent transfer of photogenerated electrons to the accommodated molecular  $[\text{Ni}(\text{bpy})_3]^{2+}$  complexes, which form  $[\text{Ni}(\text{bpy})_2]^0$  active sites that couple with  $\text{CO}_2$  to produce CO. The open channel of PI-COF-TT facilitates the processes of photogeneration of molecular Ni active sites and the subsequent activation and conversion of  $\text{CO}_2$ , while the strong adsorption affinity of PI-COF-TT for  $\text{CO}_2$  may increase the local concentration of  $\text{CO}_2$  in the channels, promoting the formation of  $\text{Ni-CO}_2$  adducts and facilitating the selective reduction of  $\text{CO}_2$ .

A recent study reported the fabrication and performance evaluation of a van der Waals heterojunction (vdWH) catalyst, namely 2D CN-COF, which is a composite material made of two-dimensional carbon nitride



**Fig. 10.** (a) The kinetic profile of CO production facilitated by PI-COF-TT, (b) the catalytic performance of PI-COF-TT with in-situ formation of [Ni(bpy)<sub>3</sub>]<sup>2+</sup> (designated as 1) and with direct impregnation of [Ni(bpy)<sub>3</sub>]<sup>2+</sup> (designated as 2), (c) elucidates the proposed reaction mechanism underlying the photoreduction of CO<sub>2</sub> over PI-COF-TT, (d) preparation of 2D-CN COF, (e) catalytic activities exhibited by the prepared catalysts, (f) schematic representation of the type II heterojunction of the 2D CN-COF and (g) proposed reaction mechanism of the photocatalytic reduction of CO<sub>2</sub> over the 2D CN-COF. Reproduced through Copyright © permission.

(2D CN) and a triazine-based COF (COF-TD) [108]. In the study, Song and coworkers explored the feasibility of the vdWH concept, which relies on the interaction between two different semiconductors, to form a type II heterojunction between the 2D CN and COF-TD (Figs. 10 (d) and (f)). The assessment of 2D CN-COF for its photocatalytic activity in the reduction of CO<sub>2</sub> to hydrocarbon fuels without the use of any solvents or sacrificial agents revealed the composite exhibited improved efficiency as compared to the 2D CN and COF-TD counterparts that produce CO and methane (CH<sub>4</sub>) as final gas products with low evolution rates. The 2D CN-COF composite reported CO and CH<sub>4</sub> evolution rates of 7.08 μmol g<sup>-1</sup> h<sup>-1</sup> and 2.37 μmol g<sup>-1</sup> h<sup>-1</sup>, respectively, which were 9.2 and 3.3 times higher than those of 2D CN and COF-TD, respectively (Fig. 10 (e) for evaluation of photocatalytic performance of catalysts). The authors attributed this improvement to the effective migration of photo-induced electrons from the CB of 2D CN to the CB of COF-TD and the transfer of holes on the VB of COF-TD to the VB of 2D CN. This spatial separation of electrons and holes reduced the recombination rate of electron-hole pairs, facilitating charge carrier migration. They employed several techniques to investigate the ability of 2D CN-COF to promote CO<sub>2</sub> reduction. UV-vis diffuse reflectance spectroscopy revealed that 2D CN-COF absorbs a broader range of light wavelengths compared to pristine 2D CN, indicating more efficient light utilization. This finding was further corroborated by bandgap calculations, which showed a narrower bandgap in 2D CN-COF. This narrower bandgap allows the material to be activated by lower energy light, making the CO<sub>2</sub> reduction process more energy-efficient. XPS valence band spectra provided additional insights, showing that both 2D CN and 2D CN-COF possess

valence band potentials suitable for water oxidation, and their conduction band potentials are negative enough to drive the conversion of CO<sub>2</sub> into various products.

Furthermore, the significant decrease in emission intensity observed for 2D CN-COF via PL spectroscopy suggested a reduction in the recombination of electron-hole pairs generated by light irradiation. This reduction in recombination is likely to enhance photocatalytic activity, as it allows for more efficient utilization of the generated charges, ultimately leading to a more effective CO<sub>2</sub> reduction process. EIS and transient photocurrent measurements were also employed to evaluate charge transfer efficiency within the material. The lower arc radius and higher photocurrent observed for 2D CN-COF compared to 2D CN indicated superior charge transport and separation. Control experiments evaluating the photocatalytic reduction activity of 2D CN-COF confirmed that the carbonaceous products originated from CO<sub>2</sub> and not from surface contaminants on the catalyst. The experiments demonstrated that light irradiation and the presence of electrons are essential for the reaction to proceed, validating that the observed CO<sub>2</sub> reduction is indeed a light-driven process that utilizes the photo-generated charges within the 2D CN-COF composite. This study also proposed a reaction mechanism for the photocatalytic reduction of CO<sub>2</sub> in the 2D CN-COF composite, as illustrated in Fig. 10 (g). Under light irradiation, the photo-induced electrons migrate from 2D CN to COF-TD, while the holes on the VB of COF-TD transfer to the VB of 2D CN, thereby realizing spatial separation, which remarkably reduces the recombination rate of electron-hole pairs and facilitates the charge carrier migration. The electrons in COF-TD then migrate to the active sites and react

with adsorbed  $\text{CO}_2$  and  $\text{H}^+$  to produce  $\text{CO}$  and  $\text{CH}_4$ , while the holes in 2D CN oxidize adsorbed  $\text{H}_2\text{O}$  to give  $\text{O}_2$  and  $\text{H}^+$ . In short, the active sites in 2D CN and COF-TD work synergistically to catalyse the photoreduction of  $\text{CO}_2$  to hydrocarbon fuels with high efficiency.

In another study, a composite of wide bandgap  $\beta\text{-Ga}_2\text{O}_3$  and narrow bandgap COF was used as a photocatalyst to efficiently reduce  $\text{CO}_2$  to  $\text{CO}$  under visible light irradiation [109]. Under visible light, the narrow bandgap COF was excited to generate electrons in the CB and holes in the VB. Meanwhile, the wide bandgap  $\beta\text{-Ga}_2\text{O}_3$  served as an electron transfer mediator without generating holes. This heterojunction facilitated the rapid transfer of photogenerated electrons from COF to  $\beta\text{-Ga}_2\text{O}_3$ , resulting in efficient solar energy utilization and effective  $\text{CO}_2$  reduction. Further investigations delved into the mechanistic aspects underlying the enhanced photocatalytic performance. Controlled experiments confirmed that  $\beta\text{-Ga}_2\text{O}_3$  alone remained inactive under visible light, showing the synergistic effect and essential role of the  $\beta\text{-Ga}_2\text{O}_3$ /COF heterojunction. Additionally, liquid-phase  $^1\text{H}$  NMR analysis demonstrated 100% selectivity towards  $\text{CO}$  production, while in-situ FT-IR spectroscopy identified intermediate  $\text{CO}_2$  reduction products, including monodentate and bidentate carbonates and bicarbonate species. These findings were consistent with previous studies and supported a proposed mechanism involving sequential steps from  $\text{CO}_2^*$  to  $\text{COOH}^*$  and ultimately  $\text{CO}^*$ . Physicochemical analyses revealed  $\text{CO}_2$  adsorption capacity and thermal desorption characteristics, confirming the influence of surface properties and heterojunction formation on catalytic efficiency. Photophysical studies, including PL spectroscopy, transient absorption spectra, photocurrent response, and EIS highlighted reduced charge carrier recombination and improved transport efficiency in the  $\beta\text{-Ga}_2\text{O}_3$ /COF composite compared to pure COF or  $\beta\text{-Ga}_2\text{O}_3$  alone.

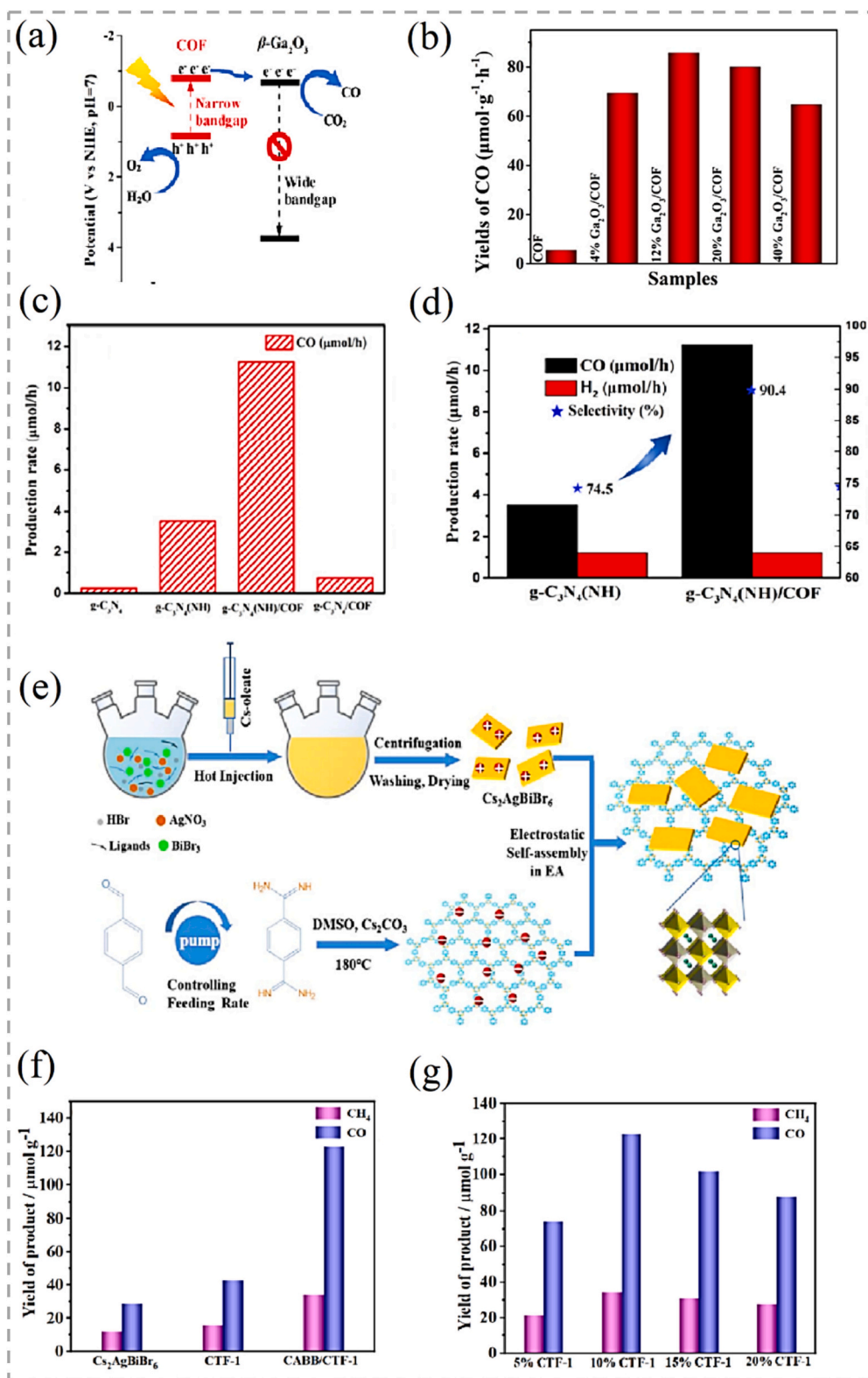
The proposed photocatalytic mechanism (Fig. 11 (a)) involves the utilization of holes on the VB of the COF to generate  $\text{O}_2$  from  $\text{H}_2\text{O}$ . This process is characterized by a consumption ratio of electrons to holes of 1.2:1. The reduction of  $\text{CO}_2$  involved the generation of  $\text{CO}_2^*$  from adsorbed  $\text{CO}_2$  under excitation light, followed by interaction with adsorbed  $\text{H}_2\text{O}$  to form  $\text{COOH}^*$  intermediates and finally protonation to form  $\text{CO}^*$  ( $\text{CO}_2 \rightarrow \text{CO}_2^* \rightarrow \text{COOH}^* \rightarrow \text{CO}^*$ ). The  $\beta\text{-Ga}_2\text{O}_3$ /COF composite overall exhibited outstanding photocatalytic  $\text{CO}_2$  reduction performance with preeminent selectivity towards  $\text{CO}$ , and the optimal composite had a  $\text{CO}$  yield 15.6 times higher than that of pure COF. By varying the concentration of  $\beta\text{-Ga}_2\text{O}_3$  within the  $\beta\text{-Ga}_2\text{O}_3$ /COF composites, a notable impact on the yield of  $\text{CO}$  production has been observed. The range of  $\text{CO}$  yield extends from  $5.5 \mu\text{mol g}^{-1} \text{h}^{-1}$  to  $85.8 \mu\text{mol g}^{-1} \text{h}^{-1}$ , with the highest yield being achieved at a composition of 12%  $\text{Ga}_2\text{O}_3$ /COF, as shown in Fig. 11 (b). DFT analysis elucidated that the superiority was attributed to the accelerated separation/transfer of charge carriers and the electron transfer pathway. The  $\beta\text{-Ga}_2\text{O}_3$ /COF system efficiently converted solar energy to fuel by hindering the recombination of electron holes in a clean and efficient narrow-wide bandgap heterojunction.

Prompted by the fact that exfoliating bulk  $\text{g-C}_3\text{N}_4$  into ultrathin nanosheets would be beneficial to both the exposure of active sites and optimization of electronic structure, a 2D/2D heterojunction photocatalyst,  $\text{g-C}_3\text{N}_4$  (NH)/COF, was developed by coupling defective  $\text{g-C}_3\text{N}_4$  nanosheets ( $\text{g-C}_3\text{N}_4$  (NH)) with Tp-Tta COF [110]. This composite exhibited enhanced photocatalytic performance for  $\text{CO}_2$  reduction due to its effective interface contact area and optimized electronic structure. The presence of nitrogen vacancies in  $\text{g-C}_3\text{N}_4$  widened the Fermi level gap between  $\text{g-C}_3\text{N}_4$  (NH) and Tp-Tta COF, promoting the recombination of invalid photogenerated carriers through an S-scheme pathway. The vdW heterostructure interface accelerated the transfer of photogenerated charges, preventing the deactivation of oxygen vacancies in  $\text{g-C}_3\text{N}_4$  (NH)/COF and providing much higher photocatalytic activity and stability. The above is supported by several methods conducted to investigate charge separation and transfer efficiency, including PL, transient photocurrent, and EIS. The results obtained showed that the  $\text{g-C}_3\text{N}_4$  (NH) exhibited weaker PL intensity compared to  $\text{g-C}_3\text{N}_4$ , and the

PL of  $\text{g-C}_3\text{N}_4$  (NH)/COF was almost completely quenched, indicating enhanced charge separation efficiency. On the other hand, transient photocurrent responses showed that  $\text{g-C}_3\text{N}_4$  (NH)/COF had a 4.7- and 1.6-times higher response than  $\text{g-C}_3\text{N}_4$  and  $\text{g-C}_3\text{N}_4$  (NH), respectively. The EIS spectra revealed a much smaller radius for  $\text{g-C}_3\text{N}_4$  (NH)/COF, implying lower interfacial charge transfer resistance. These findings demonstrated that coupling Tp-Tta COF with  $\text{g-C}_3\text{N}_4$  (NH) forms a vdW heterojunction that promotes photogenerated carrier separation and accelerates interfacial charge transfer, enhancing the photocatalytic reduction of  $\text{CO}_2$ . The mechanism of this process involves the spontaneous migration of electrons from  $\text{g-C}_3\text{N}_4$  (NH) to Tp-Tta COF upon contact, resulting in charge rearrangement, the establishment of a built-in electric field at the interfaces of  $\text{g-C}_3\text{N}_4$  (NH) and Tp-Tta COF, and the transfer of electrons along an S-scheme path under visible light irradiation. This photocatalyst exhibited a stable and highly selective  $\text{CO}$  (90.4%) generation rate of  $11.25 \mu\text{mol h}^{-1}$  under visible light irradiation, which was 45-fold and 15-fold higher than that of  $\text{g-C}_3\text{N}_4$  and  $\text{g-C}_3\text{N}_4$ /COF, respectively. Fig. 11 (c) depicts that the pristine  $\text{g-C}_3\text{N}_4$  exhibits a relatively low  $\text{CO}$  yield rate, amounting to only  $0.25 \mu\text{mol h}^{-1}$ , attributed to the rapid charge recombination process. However, introducing nitrogen vacancies onto the  $\text{g-C}_3\text{N}_4$  structure has proven highly effective in significantly enhancing the photocatalytic performance for  $\text{CO}_2$  reduction. Fig. 11 (d) shows that  $\text{g-C}_3\text{N}_4$  (NH)/COF demonstrates superior  $\text{CO}$  selectivity (90.4%) compared to  $\text{g-C}_3\text{N}_4$  (NH) (74.5%), indicating enhanced  $\text{CO}_2$  to  $\text{CO}$  conversion on  $\text{g-C}_3\text{N}_4$  (NH)/COF.

Zhang et al. developed a novel hybrid photocatalyst (CABB/CTF-1) by using electrostatic self-assembly of  $\text{Cs}_2\text{AgBiBr}_6$  (CABB) and CTF-1 [111]. This was achieved through Coulomb electrostatic attraction between the two semiconductors and the nitrogen sites in CTF-1, allowing efficient interfacial contact, as depicted in Fig. 11 (e). The resulting strong interaction between the NSs facilitated interfacial charge transfer and created an S-scheme heterojunction. This effectively promoted charge separation and produced  $\text{CO}$  and  $\text{CH}_4$  as the main carbonous product. To elucidate the interaction of  $\text{Cs}_2\text{AgBiBr}_6$  and CTF-1 for  $\text{CO}_2$  reduction, the authors employed several techniques, including XPS, which revealed electron transfer from  $\text{Cs}_2\text{AgBiBr}_6$  to CTF-1, thereby suggesting an internal electric field and an S-scheme heterojunction formation. Electron spin resonance (ESR) confirmed this S-scheme by detecting radicals indicative of the electron transfer direction. This heterojunction improved charge separation, as shown by increased photocurrent and reduced luminescence in transient and photoluminescence studies. Finally,  $\text{CO}_2$  adsorption analysis highlighted the importance of the porous structure of CTF-1 in enhancing  $\text{CO}_2$  uptake and overall photocatalytic performance. During photocatalysis, efficient charge separation led to the accumulation of electrons in the CB of  $\text{Cs}_2\text{AgBiBr}_6$  and the VB of CTF-1, both contributing to the  $\text{CO}_2$  reduction reaction. Conversely, the electrons in the CB of CTF-1 and the holes in the VB of  $\text{Cs}_2\text{AgBiBr}_6$  were effectively eliminated via an S-scheme pathway facilitated by internal electric fields, band bending, and Coulomb interaction. The CTF-1 component of the hybrid also possessed a unique porous structure, providing strong  $\text{CO}_2$  adsorption capacity and facilitating the subsequent  $\text{CO}_2$  reduction reaction. The resulting CABB/CTF-1 hybrid exhibited a significantly enhanced photocatalytic activity, with the highest total product yield of  $157.3 \mu\text{mol g}^{-1}$  ( $122.9 \mu\text{mol g}^{-1}$  for  $\text{CO}$  and  $34.4 \mu\text{mol g}^{-1}$  for  $\text{CH}_4$ ) and with the CABB/CTF-1 hybrid with 10% CTF-1 has the highest  $\text{CO}_2$  photoreduction performance, as shown in Figs. 11 (f) and (g).

In a recent report, an olefin-linked COF denoted as TTCOF, was prepared from the reaction of 2,4,6-trimethyl-1,3,5-triazine (TMT) and 1,3,5-tris(4-formylphenyl)-triazine (TFPT) as monomers [112]. The integration of TTCOF with  $\text{NH}_2$  - UiO-66 (Zr) (NUZ), a representative octahedral MOF as well as an n-type semiconductor, resulted in the formation of an olefin (C=C) linked COF (TTCOF)/ $\text{NH}_2$  - UiO-66 (Zr) (NUZ) (TTCOF/NUZ) S-type heterojunction for the evaluation of  $\text{CO}_2$  photoreduction efficiency. The 15% TTCOF/NUZ photocatalyst demonstrated superior performance in converting  $\text{CO}_2$  to  $\text{CO}$  in the



**Fig. 11.** (a) CO evolution rates of β-Ga<sub>2</sub>O<sub>3</sub>/COF composites during 4 h of visible-light irradiation, (b) a proposed photocatalytic mechanism for CO<sub>2</sub> reduction with β-Ga<sub>2</sub>O<sub>3</sub>/COF, (c) the photocatalytic CO<sub>2</sub> reduction rates of the prepared samples in [110], (d) photocatalytic yields and selectivity of CO and H<sub>2</sub> for g-C<sub>3</sub>N<sub>4</sub>(NH) and g-C<sub>3</sub>N<sub>4</sub>(NH)/COF, (e) the formation process of 2D/2D CABB/CTF-1 hybrid through electrostatic interaction, (f) a comparison of CO<sub>2</sub> photoreduction performance among CTF-1 nanosheets, C<sub>2</sub>AgBiBr<sub>6</sub> nanosheets, and CABB/CTF-1 hybrid, and (g) CO<sub>2</sub> photoreduction performance of CABB/CTF-1 hybrids with varying CTF-1 contents. Reproduced through Copyright © permission.

absence of a cocatalyst or sacrificial agent, yielding CO at a rate of  $6.56 \mu\text{mol g}^{-1} \text{h}^{-1}$ , which is 4.4 times higher than that of pristine TTCOF and 5 times higher than NUZ, as shown in Fig. 12 (a). In the study, XPS was employed to investigate the elemental composition and chemical states within TTCOF, NUZ, and their composites to understand their  $\text{CO}_2$  reduction mechanism. High-resolution spectra revealed changes in binding energies, suggesting electron transfer between the materials. Additionally, BET surface area analysis indicated more active sites for photocatalysis in the 15% TTCOF/NUZ composite. Further characterizations such as UV-vis DRS, PL spectroscopy, and photoelectrochemical tests examined optical and electrochemical properties. These techniques showed enhanced light absorption, increased photocurrent density, and

reduced charge carrier recombination, particularly in 15% TTCOF/NUZ. Time-resolved TAS measured longer lifetimes of photogenerated carriers in the hybrid materials, leading to improved photocatalytic efficiency. To gain deeper mechanistic insights, Mott-Schottky plots, EPR spectroscopy, and in situ FTIR were employed. Mott-Schottky analysis confirmed the n-type nature of both materials, while EPR spectra revealed an S-scheme charge transfer route within the 15% TTCOF/NUZ heterojunction. Finally, in situ FTIR identified intermediate products, providing clues about the  $\text{CO}_2$  reduction pathway to CO. It was postulated that the charge transfer process over the TTCOF/NUZ heterojunction followed the S-scheme route, as illustrated in Fig. 12 (b). Initially, the CB potential of TTCOF was higher than that of NUZ,

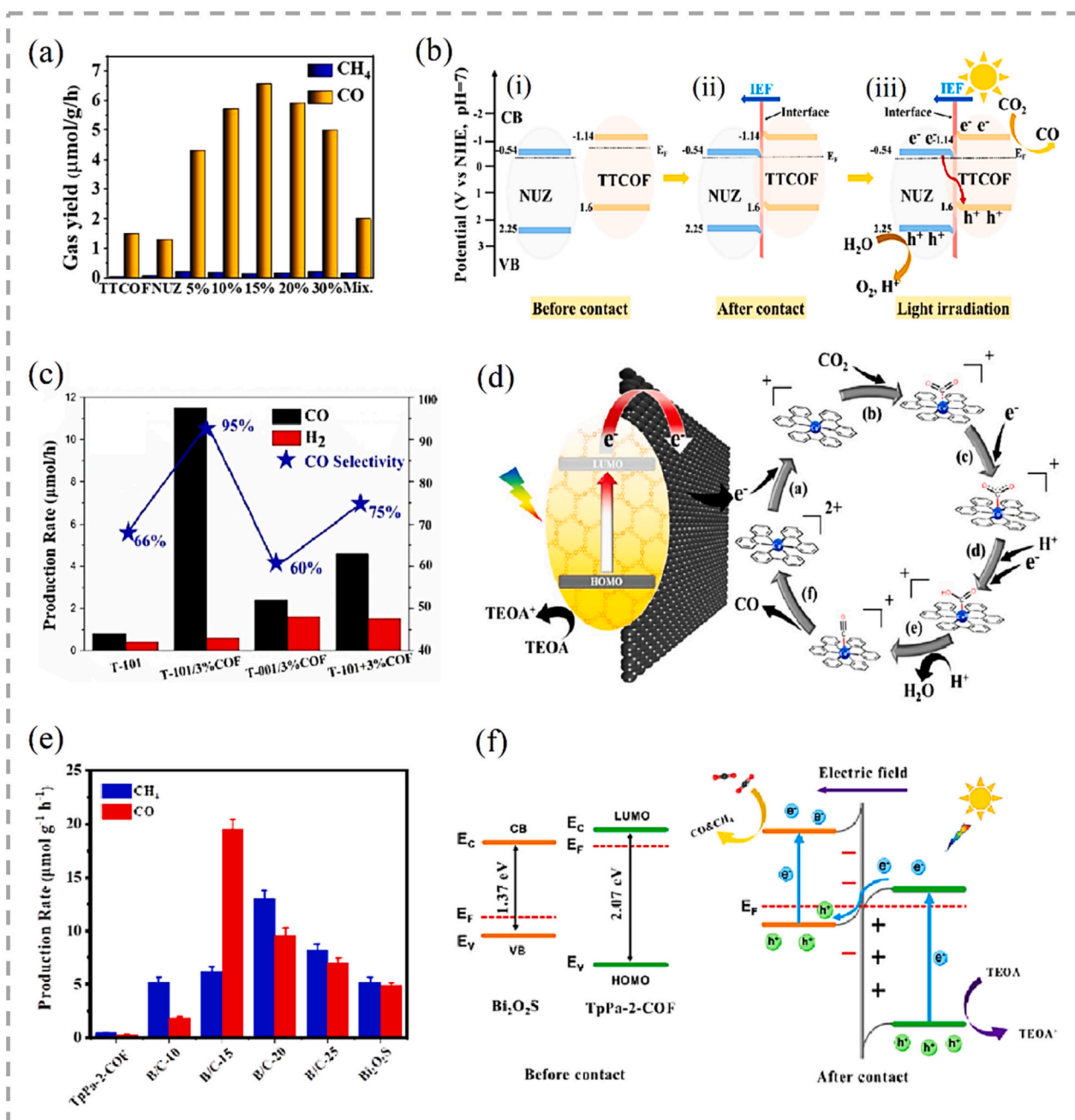


Fig. 12. (a) Photocatalytic  $\text{CO}_2$  conversion rates for TTCOF, NUZ, and x% TTCOF/NUZ (x = 5, 10, 15, 20, 30), (b) a schematic representation of the S-scheme pathway before contact (i), after contact (ii), and during light irradiation (iii) for TTCOF and NUZ samples, (c) a comparative analysis of photocatalytic  $\text{CO}_2$  reduction rates and selectivity for the prepared samples in [113], (d) a proposed mechanism for the photocatalytic  $\text{CO}_2$  reduction by  $\text{rGO}_{15}$ @TpPa-1, (e) photocatalytic  $\text{CO}_2$  reduction to  $\text{CH}_4$  performance assessed for the prepared samples in [114], and (f) the proposed mechanism underlying the enhancement of photocatalytic  $\text{CO}_2$  reduction by the  $\text{Bi}_2\text{O}_5$ @TpPa-2-COF heterojunction. Reproduced through Copyright © permission.

resulting in energy band bending upon contact. Later, after contact between TTCOF and NUZ, electrons in TTCOF tend to transfer to NUZ until the Fermi level is balanced, creating an internal electric field (IEF) at the TTCOF/NUZ interface with direction from TTCOF to NUZ. Under light irradiation, the photocatalysts are excited, generating electron-hole pairs. The photoexcited electrons of NUZ then quickly reorganize with the holes of TTCOF, facilitated by the IEF and band bending, resulting in the formation of a typical S-scheme heterojunction. This route allows TTCOF-CB to accumulate photogenerated electrons while NUZ-VB accumulates holes, resulting in hybrid materials with robust redox abilities. The photoreduction of CO<sub>2</sub> to CO over TTCOF/NUZ heterostructures follows the proposed reaction pathways: CO<sub>2</sub> → CO<sub>2</sub><sup>-</sup> → HCOOH\* → CO\* → CO.

An and colleagues investigated the impact of contact facets on the activity of heterostructures for CO<sub>2</sub> photoreduction of TiO<sub>2</sub>/Tp-Tta COF S-scheme heterojunction prepared from the self-assembly imine-linked COF built from Tta and 1,3,5-triformylphloroglucinol (Tp) onto faceted TiO<sub>2</sub> [113]. The facet engineering of T-101/3% COF S-scheme heterojunctions unveiled a CO<sub>2</sub> reduction rate of 11.6 μmol h<sup>-1</sup>, which was 14.5 times higher than that of pristine 101-TiO<sub>2</sub>, and feature a better CO selectivity at 95% as compared to T-001/3% COF (60%) and T-101 + 3% COF (75%), as depicted in Fig. 12 (c). For a better understanding of the underlying mechanisms of photocatalytic CO<sub>2</sub> reduction, UV-vis diffuse reflectance spectroscopy was employed and Tauc plots revealed the light absorption properties and bandgaps of the materials. Tp-Tta COF exhibited superior light absorption across the visible spectrum compared to T-001 and T-101, leading to enhanced light utilization. Bandgap calculations showed a narrower bandgap for Tp-Tta COF (1.68 eV) compared to T-001 (3.28 eV) and T-101 (3.22 eV). Mott-Schottky measurements, on the other hand, provided insights into the electronic band positions. The data suggested that electron transfer between Tp-Tta COF and TiO<sub>2</sub> could potentially follow either an S-scheme or type II heterojunction, promoting efficient charge separation for CO<sub>2</sub> reduction. Electron paramagnetic resonance (EPR) analysis using DMPO as a trapping agent confirmed the generation of ·OH. The presence of these radicals in T-001 and T-101 under light irradiation indicated their ability to produce oxidizing species. However, Tp-Tta COF alone did not generate ·OH due to its high hole potential energy.

Notably, the EPR signals were more pronounced in TiO<sub>2</sub>/Tp-Tta COF heterostructures compared to TiO<sub>2</sub> alone, supporting efficient charge transfer and the S-scheme mechanism. The mechanism of interfacial charge transfer and the formation of S-scheme heterojunction in T-101/COF composite was summarized as follows: The difference in Fermi level between T-101 and Tp-Tta COF led to the spontaneous transfer of electrons from the CB of Tp-Tta COF to T-101, resulting in equalization of their Fermi levels. As a result, Tp-Tta COF became positively charged, while T-101 became negatively charged. This charge redistribution induced the formation of an IEF and band edge bending at the interface. Under illumination, both T-101 and COF were excited into their CB. Due to coulombic forces generated by the IEF and band bending, photoinduced electrons in the CB of T-101 recombined with photoinduced holes in the VB of COF produced photogenerated electrons with strong reduction ability.

Inspired by the exceptional properties of graphene and its derivatives, Gopalakrishnan and coworkers sought to enhance CO<sub>2</sub> reduction by minimizing the recombination of photogenerated carriers. Their approach focused on improving CO<sub>2</sub> adsorption and activation, enhancing light absorption, and increasing photostability [115]. They constructed a keto-enamine COF incorporated with varying concentrations of reduced graphene oxide, denoted as rGO<sub>x</sub>@TpPa-1 (x = 5%, 10%, 15%, and 20%), to improve charge separation and enhance the efficiency of CO<sub>2</sub> photoreduction. The rGO<sub>15</sub>@TpPa-1 nanocomposite demonstrated exceptional photocatalytic efficiency for CO<sub>2</sub> reduction under visible light irradiation, producing CO at a rate of approximately 200 μmol g<sup>-1</sup> h<sup>-1</sup> with a selectivity of 89%. This selectivity was 1.57 and 6.97 times higher than the bare COF and rGO counterparts, respectively.

To confirm that the produced CO originated from the photocatalytic process, the authors employed carbon isotopic measurements using GC-IRMS; the presence of the dominant <sup>13</sup>CO<sub>2</sub> peak confirmed that the evolved CO stemmed directly from the CO<sub>2</sub> reduction reaction. Furthermore, control experiments lacking the cocatalyst or sacrificial agent also showed reduced or no CO formation, highlighting their necessity for forming active sites and removing holes during the photoreduction process. Photoelectrochemical studies provided valuable insights into the redox properties and reaction mechanism. Transient photocurrent responses under visible light showed a significant enhancement in rGO15@TpPa-1 compared to bare TpPa-1. This indicates improved photogenerated carrier density due to strong light absorption and reduced recombination rates within the composite material. EIS further revealed better electron mobility within rGO15@TpPa-1. Additionally, Mott-Schottky plots provided information about the LUMO energy levels of the material. These analyses confirmed the n-type semiconductor characteristics and appropriate redox potentials essential for the CO<sub>2</sub> reduction process. PL spectra and time-resolved PL decay data were analysed to understand charge carrier dynamics. The reduced PL intensity and shorter excited electron lifetime observed in rGO15@TpPa-1 suggest efficient electron transfer and reduced recombination. This ultimately translates to enhanced photocatalytic activity for CO<sub>2</sub> reduction. As shown in Fig. 12 (d), the authors proposed a possible mechanism for the photocatalytic reduction of CO<sub>2</sub> to CO. In the study, cocatalyst [Co(bpy)<sub>3</sub>]<sup>2+</sup> acts as an aqueous electron mediator, promoting intramolecular charge transfer. Upon visible light exposure, TpPa-1 COF becomes excited and generates electrons, which migrate to rGO and then to [Co(bpy)<sub>3</sub>]<sup>2+</sup>, reducing it to [Co(bpy)<sub>3</sub>]<sup>+</sup>, which then reacts with CO<sub>2</sub> to form the transition-state intermediate [Co(bpy)<sub>3</sub>CO<sub>2</sub>]<sup>+</sup> via η<sup>1</sup>-CO<sub>2</sub> coordination, followed by electron transfer to form [Co(bpy)<sub>3</sub>(CO<sub>2</sub>)<sup>-</sup>]<sup>+</sup>. The electron transfer from Co<sup>I</sup> to CO<sub>2</sub> in [Co(bpy)<sub>3</sub>(CO<sub>2</sub>)<sup>-</sup>]<sup>+</sup> leads to the formation of [Co(bpy)<sub>3</sub>(CO<sub>2</sub>)<sup>-</sup>]<sup>+</sup> and the subsequent protonation and reduction in successive steps generate CO and [Co(bpy)<sub>3</sub>]<sup>2+</sup>. In this hybrid heterogeneous photocatalyst, the Co sites act as catalytic active sites, effectively coordinating and activating CO<sub>2</sub> molecules. rGO anchored onto TpPa-1 serves as a host for effective CO<sub>2</sub> adsorption, contributing to enhanced catalytic activity and selectivity towards CO<sub>2</sub> reduction. The holes created in the HOMO of TpPa-1 oxidize TEOA to TEOA<sup>+</sup>.

A recent study demonstrated the use of Bi<sub>2</sub>O<sub>2</sub>S nanosheets to enhance the separation efficiency of photogenerated carriers in COF [114]. To achieve this, TpPa-2-COF was grown in situ on Bi<sub>2</sub>O<sub>2</sub>S nanosheets to form a p-n heterojunction, Bi<sub>2</sub>O<sub>2</sub>S@TpPa-2-COF-15, through covalent bonding. The resulting hybrid material exhibited improved and maximum photocatalytic activity for CO<sub>2</sub> reduction at the ratio of Bi<sub>2</sub>O<sub>2</sub>S: TpPa-2-COF = 15%, with a CO yield of 19.5 μmol g<sup>-1</sup> h<sup>-1</sup>. This represents a significant increase of 66.8 and 3.96 times compared to pure TpPa-2-COF and Bi<sub>2</sub>O<sub>2</sub>S, respectively, as depicted in Fig. 12 (e). To elucidate the mechanism of the photocatalytic reduction of CO<sub>2</sub> of Bi<sub>2</sub>O<sub>2</sub>S@TpPa-2-COF composites, key characterizations were performed, including the Tauc curve, which indicated that the band gap widths of TpPa-2-COF and Bi<sub>2</sub>O<sub>2</sub>S were 1.37 and 2.07 eV, respectively. Additionally, the Mott-Schottky curve was used to determine the positions of the conduction bands of these materials. XPS valence band spectra of both TpPa-2-COF and Bi<sub>2</sub>O<sub>2</sub>S were obtained, and the energy band positions were analysed, confirming the formation of a p-n heterojunction. Bi<sub>2</sub>O<sub>2</sub>S exhibited low stability due to its narrow band gap and easy recombination of photo-generated electron-hole pairs; however, the B/C-15 composite demonstrated good photocatalytic stability and prevented the mixing of photogenerated carriers. The enhanced photocatalytic CO<sub>2</sub> reduction observed in the p-n heterojunction of Bi<sub>2</sub>O<sub>2</sub>S and TpPa-2-COF is attributed to the following mechanism: Initially, the Fermi energy level of TpPa-2-COF is higher compared to that of Bi<sub>2</sub>O<sub>2</sub>S, as illustrated in Fig. 12 (f). Upon interaction, electrons migrate from TpPa-2-COF to the surface of Bi<sub>2</sub>O<sub>2</sub>S. This charge transfer results in the alignment of the Fermi energy levels at the interface, thereby

establishing a balanced p-n junction. This redistribution of charge created an inner electric field that flowed directionally from TpPa-2-COF to Bi<sub>2</sub>O<sub>2</sub>S, resulting in the formation of an enclosed charge area at the junction of the two materials. The energy bands of TpPa-2-COF and Bi<sub>2</sub>O<sub>2</sub>S were then bent up and down to attain thermodynamic and kinetic equilibrium. In the presence of visible light, photogenerated electrons were stimulated from the VB of Bi<sub>2</sub>O<sub>2</sub>S and TpPa-2-COF to their conduction bands. To promote electron-hole separation, a significant number of electrons were concentrated in the VB of TpPa-2-COF, and the IEF facilitated their transfer to the VB of Bi<sub>2</sub>O<sub>2</sub>S where they recombined with the holes generated by light excitation. This resulted in the conversion of CO<sub>2</sub> to CO and CH<sub>4</sub> through the action of electrons enriched in the CB of Bi<sub>2</sub>O<sub>2</sub>S, while the holes accumulated in the VB of TpPa-2-COF were eliminated by the sacrificial agent TEOA. Table 1 summarises the photocatalytic reduction of CO<sub>2</sub> utilizing COFs as photocatalysts, as discussed in this section. An evaluation of the effectiveness of the three pathways discussed above will be addressed in the subsequent section.

## 5. Mechanistic comparison of photocatalytic reduction of CO<sub>2</sub> in COFs

Understanding the underlying mechanism of photocatalytic CO<sub>2</sub> reduction in COFs is crucial for designing more efficient COF materials. Although the goal of reducing CO<sub>2</sub> is common to different reduction mechanisms, the differences between them are worth noting to optimize the design of COFs. In one mechanism, COFs rely solely on their intrinsic properties to generate photogenerated charge carriers and promote electron transfer for catalytic activity upon light absorption. Meanwhile, incorporating catalytic active sites by introducing metal ions such as Ni [100], Cu [103], and Co [106] into the COF structure can significantly enhance photocatalytic activity. The active sites create additional redox centres, leading to a higher density of active sites, and facilitate charge separation and transfer, improving catalytic efficiency. The metal ions in the active sites act as electron donors and acceptors, promoting transfer of photogenerated charge carriers to CO<sub>2</sub> molecules, ultimately producing reduced CO<sub>2</sub> products such as CO and/or CH<sub>4</sub>.

Furthermore, active sites can enhance COF stability under photocatalytic conditions by acting as anchoring points to stabilize the COF structure and prevent degradation of the framework during photocatalysis, which is critical for sustained catalytic performance. Compared to the mechanism based on photogenerated charge carriers, the mechanism involving catalytic active sites provides an alternative pathway for CO<sub>2</sub> reduction that is not solely dependent on charge separation and transfer efficiency. This can be particularly advantageous under conditions where the photoexcited charge carriers are limited, such as in low-light environments or when the COF has a low light absorption capacity.

Researchers have also explored synergistic materials to create heterojunctions to enhance the photocatalytic activity of COFs. This approach involves combining COFs with other materials, such as metal oxides, graphene, and MOF, to form heterojunctions that improve the separation and transfer of photogenerated charge carriers. While incorporating catalytic active sites into COFs has proven effective in enhancing CO<sub>2</sub> reduction by promoting active intermediate formation and increasing CO<sub>2</sub> adsorption, the use of heterojunctions has shown more versatility in achieving high photocatalytic activity with a wider range of materials and in optimizing band structure and charge transfer properties. Specifically, heterojunctions contribute to the better separation of photogenerated charge carriers and facilitate the transfer of electrons and holes to the CO<sub>2</sub> reduction sites.

The analysis of the three mechanistic pathways discussed in the earlier section reveals distinct characteristics. As shown in Table 1, majority of reactions employing photogenerated charge carriers do not use additives and predominantly result in the formation of CO and CH<sub>3</sub>OH as the primary products, with the reported yields for these major

products being  $\leq 156 \mu\text{mol g}^{-1} \text{h}^{-1}$ . On the other hand, when catalytic active sites are incorporated into the COFs, a noticeable enhancement in production yield becomes evident. For instance, Co@COF-TVBT-Bpy attains a remarkable  $1132.7 \mu\text{mol g}^{-1} \text{h}^{-1}$  of CO and  $1158.4 \mu\text{mol g}^{-1} \text{h}^{-1}$  of H<sub>2</sub> production upon inclusion of a Co active site. Similarly, COF-367-Co NSs with a Co active site also exhibit a notably high CO production rate of  $10,162 \mu\text{mol g}^{-1} \text{h}^{-1}$ , with a selectivity of approximately 78%, implying the significance of Co in enhancing the photocatalytic reduction performance of COFs. It is worth highlighting that the combination of Co and Ni within CoNi-COF-3 gives rise to the substantial CO production rate of  $2567 \mu\text{mol g}^{-1} \text{h}^{-1}$ , emphasizing the synergistic effects that can be harnessed when these metal elements are used in tandem. When employing catalytic active sites for photocatalytic reduction study of COFs, [Ru(bpy)<sub>3</sub>]Cl<sub>2</sub> commonly serves as a photosensitizer and TEOA is frequently used as a proton acceptor. The photocatalytic products obtained from this approach primarily consist of CO and are often accompanied by trace amounts of H<sub>2</sub>. In some cases, HCOOH is produced as the major product. Comparatively, the utilization of synergistic materials such as [Ni(bpy)<sub>3</sub>]<sup>2+</sup>, when paired with PI-COF-TT, results in a notable CO production rate of  $1933 \mu\text{mol g}^{-1}$  in a 4 h reaction. While this surpasses the yields observed for photogenerated charge carriers, other COFs, combined with synergistic components listed in Table 1, give rise to a photocatalytic production rate below  $200 \mu\text{mol g}^{-1} \text{h}^{-1}$ . Therefore, it is essential to highlight that the introduction of catalytic active sites stands out as a particularly effective strategy for enhancing the photocatalytic efficiency of COFs among the three approaches.

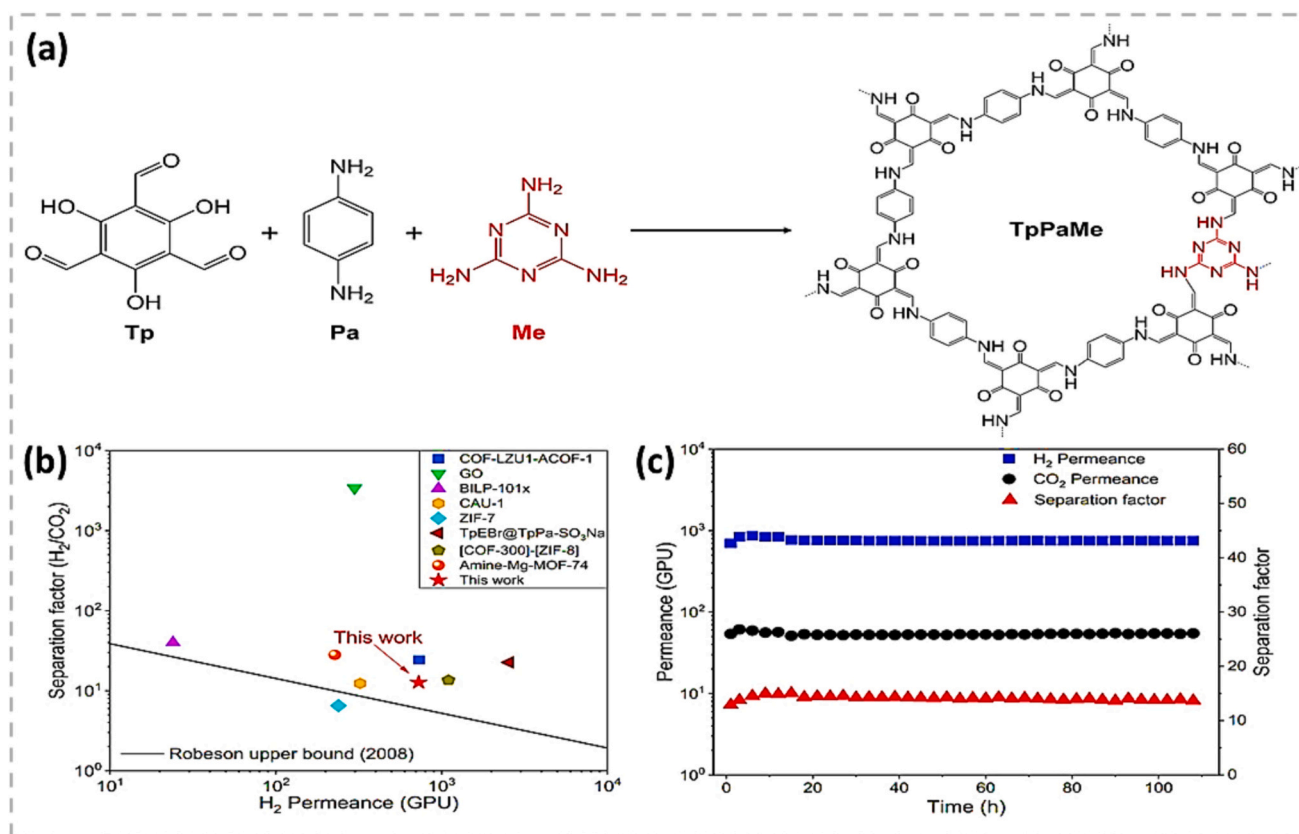
In addition to the differences between the approaches outlined, it is important to consider their respective drawbacks. For instance, while catalytic active sites can enhance electron transfer rates and boost CO<sub>2</sub> conversion efficiency, they are susceptible to deactivation over time. This deactivation can result from issues such as metal leaching or the aggregation of catalytic particles. In contrast, heterojunctions can enhance the separation and transfer of charge carriers to CO<sub>2</sub> reduction sites, but the stability and compatibility of the heterojunction materials may limit their efficacy.

## 6. Different strategies used to enhance the performance of COFs for CO<sub>2</sub>

### 6.1. Doping

The doping strategy in COFs aims to enhance the CO<sub>2</sub> reduction process. By introducing specific dopants into the COF structure, researchers seek to improve its catalytic activity and selectivity towards CO<sub>2</sub> reduction reactions. These dopants can be metals, metal ions, or other functional groups interacting with COF molecules and altering their electronic properties [117]. The goal is to create COFs with higher efficiency and selectivity for converting CO<sub>2</sub> into valuable products, such as fuels or chemical feedstocks. Zhu et al. [118] offered several techniques for introducing lithium (Li) metal into Covalent Organic Framework-102 (COF-102), a porous material recognized for its enormous surface area and low density, in recent research. Charge exchange, O-Li<sup>+</sup> dipolar interaction, and O-Li + chemical bonding were among the strategies used. The results showed that dipole doping was the most effective method for improving CO<sub>2</sub> adsorption performance. Furthermore, the researchers substituted the COF-102 ligands with extended aromatic moieties such as diphenyl and pyrene. They studied CO<sub>2</sub> and CH<sub>4</sub> adsorption capability as well as CO<sub>2</sub>/CH<sub>4</sub> selectivity using ligand-modified COF-102. In addition, Zheng et al. [116] did research in which they produced a membrane employing chemically doped melamine (Me) in a COF termed TpPa. The TpPa COF is generated via the interfacial polymerization of monomers of 1,3,5-triformylphloroglucinol (Tp) and *p*-phenylenediamine (Pa) (Fig. 13 (a)). Adding the melamine monomer may change the composition and surface features of the pores in the TpPa COF membrane, resulting in increased hydrogen





**Fig. 13.** (a) The TpPaMe membrane is created and transferred using a specific fabrication process. (b) The separation performance of the TpPaMe membrane in separating H<sub>2</sub>/CO<sub>2</sub> is compared to that of other membranes. (c) The TpPaMe membrane demonstrates long-term operational stability in the process of H<sub>2</sub>/CO<sub>2</sub> separation [116]. Reproduced through Copyright © permission.

purification capabilities. Surprisingly, the melamine-doped TpPa COF (TpPaMe COF) membrane has a separation factor of 12.7 for the H<sub>2</sub>/CO<sub>2</sub> gas combination and a hydrogen permeance of 727 GPU. This contrasts sharply with the undoped TpPa membrane, which has a smaller separation factor (7.5) and gas permeance (618 GPU). Furthermore, the TpPaMe COF membrane exhibits outstanding operational stability, exceeding the performance threshold established by Robeson in 2008 for H<sub>2</sub>/CO<sub>2</sub> separation, as shown in Fig. 13 (b). Long-term performance data for H<sub>2</sub> and CO<sub>2</sub> separation, illustrated in Fig. 13 (c), further confirms the membrane's comparative stability [116]. Kang et al. [119] made an unexpected finding on CO<sub>2</sub> sorption employing metal ion (Fe<sup>3+</sup>, Cr<sup>3+</sup>, or In<sup>3+</sup>)-doped Schiff-base two-dimensional (2D) COFs, specifically Py-1P, Py-TT, and Py-Py. Their study revealed that these doped COFs exhibited distinct CO<sub>2</sub> sorption isotherms, characterized by one or more tuneable hysteresis stages. Notably, the ion-doped Py-1P COF's CO<sub>2</sub> adsorption capacity increased by 89.5% compared to the undoped Py-1P COF. This unique CO<sub>2</sub> sorption process provides a promising and simple method for increasing the CO<sub>2</sub> capture capacity of COF-based adsorbents. These results provide important insights for advancing chemistry to enhance CO<sub>2</sub> collection and conversion processes. The CO<sub>2</sub> capture properties of 2D squaraine-bridged covalent organic polymers (SQ-COPs) are investigated in a study utilizing first-principles calculations and grand canonical Monte Carlo (GCMC) simulations. These SQ-COPs possess precisely oriented open oxygen sites in the squaric-acid unit, which are doped with Li atoms quantitatively. The research findings reveal that due to the strong affinity between Li atoms and squaraine units within SQ-COPs, the gas adsorption capacity of Li-doped SQ-COPs (SQ-COP-Li) is significantly increased, reaching three times that of pristine SQ-COPs. The presence of Li—O bonds between squaraine units and Li atoms enhances the electrostatic interaction between the framework and CO<sub>2</sub> molecules. Consequently, the adsorption capacity of CO<sub>2</sub> in SQ-COP-Li

demonstrates exceptional performance, reaching extraordinarily high values of 83.4 mmol g<sup>-1</sup> at 298 K and 100 bar for 1-Li (SQ-COP-1-Li) and 202.0 mmol g<sup>-1</sup> for 3-Li (SQ-COP-3-Li). These results indicate that the CO<sub>2</sub> uptake of 3-Li surpasses the best-performing three-dimensional covalent organic framework (COF-05) materials reported to date and even exceeds the capacities of MOF-177 and IRMOF-10, with the uptake being twice as high [120]. Stegbauer et al. [121] provide AB-COF and ATFG-COF, two structurally similar azine-linked COFs. These COFs are built of 1,3,5-triformyl benzene and 1,3,5-triformylphloroglucinol, as well as hydrazine building units. By deliberately engineering the chemical properties of the pore walls, the sorption characteristics of these COFs may be accurately tuned. The researchers show that the COFs' CO<sub>2</sub> sorption performance may be tailored through polarity engineering. In both equilibrium (sorption isotherm) and kinetic circumstances, the more polar ATFG-COF showed significant CO<sub>2</sub> uptake at low pressures (1 bar) (flow TGA, breakthrough). The apolar AB-COF, on the other hand, exhibits extraordinarily strong CO<sub>2</sub> over N<sub>2</sub> selectivity (IAST: 88). Furthermore, metal salts such as lithium and zinc acetate were incorporated into the pore walls of both COFs. At 273 K, the zinc-doped AB-COF has a high CO<sub>2</sub> uptake of 4.68 mmol g<sup>-1</sup>. These results emphasize the possibility of precisely tailoring the sorption capabilities of COFs by modifying the chemical composition of the pore walls. Additionally, incorporating metal dopants offers a promising avenue for enhancing CO<sub>2</sub> capture efficiency in COFs. Such progress is crucial for advancing the development of effective catalysts and materials aimed at reducing carbon emissions and improving sustainable CO<sub>2</sub> capture and conversion technologies.

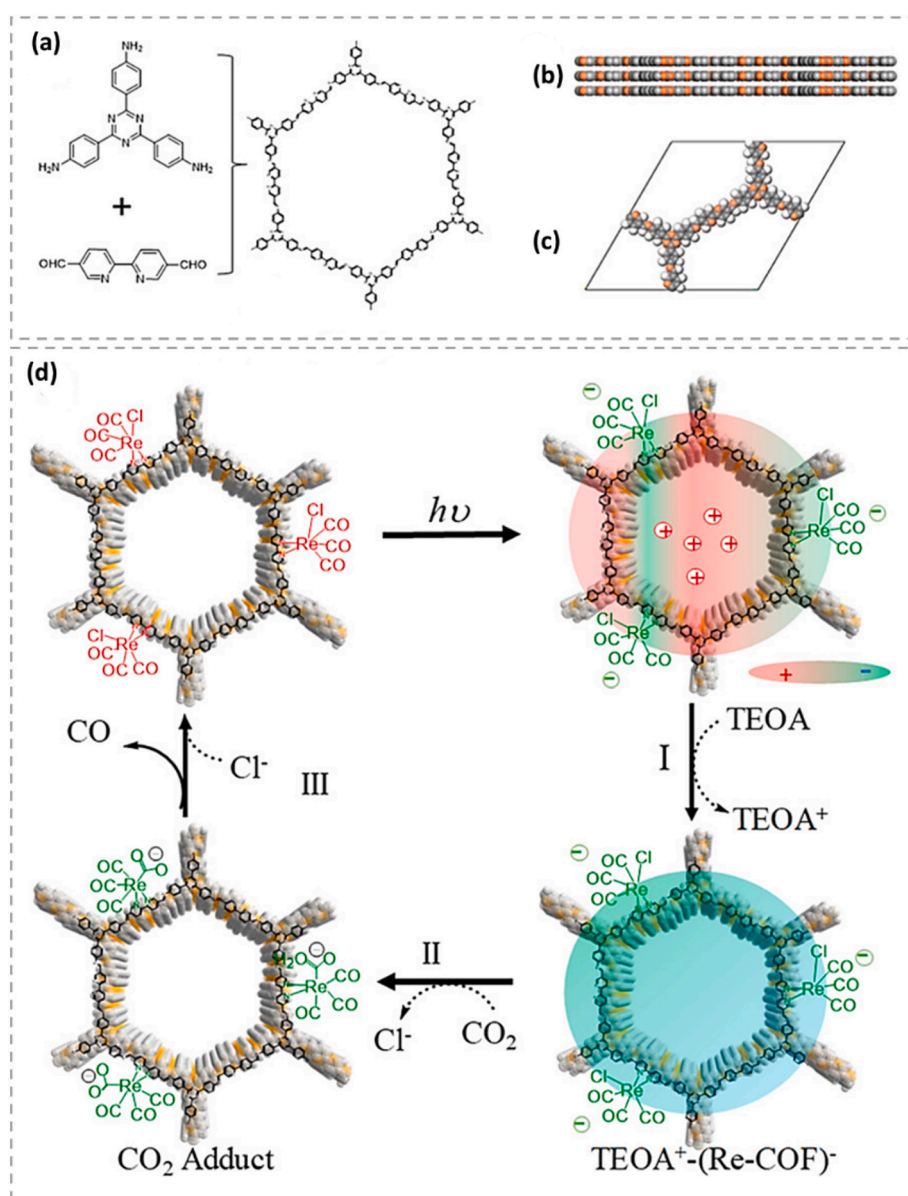
## 6.2. Cocatalytic strategy

The cocatalytic technique has emerged as a potential option for

improving the performance of COFs for CO<sub>2</sub> reduction. Synergistic effects may be produced by integrating cocatalysts into COF-based photocatalytic systems, resulting in increased catalytic activity and selectivity. Platinum (Pt) is a frequent cocatalyst utilized in COF-based CO<sub>2</sub> reduction because it acts as a co-catalyst for the HER. Pt nanoparticles may be placed on COF surfaces, creating active sites for HER and allowing for efficient electron transmission. This cocatalytic system improves the overall CO<sub>2</sub> reduction process by encouraging CO<sub>2</sub> conversion to useful compounds like formate or methane. In addition, additional cocatalysts, such as metal oxides or metal sulfides, have been investigated to promote certain chemical pathways or charge separation [122,123]. These cocatalysts may operate as electron acceptors or donors, enabling charge carrier transfer and decreasing recombination, boosting the overall efficiency of COF-based photocatalysis. The cocatalytic method allows for tremendous flexibility in modifying the parameters of the COF photocatalyst and enhancing its efficacy for CO<sub>2</sub> reduction [124]. Researchers may develop COF-based systems with better catalytic activity, improved stability, and more selectivity by carefully choosing and adding appropriate cocatalysts, opening the path

for efficient and sustainable CO<sub>2</sub> conversion technologies.

In contrast, Yang et al. [125] introduced a novel 2D COF that incorporates a rhenium (Re) complex, resulting in a hybrid catalyst with inherent light absorption and charge separation (CS) properties. The researchers demonstrate that this hybrid catalyst displays remarkable efficiency in reducing CO<sub>2</sub> to form CO under visible light illumination. Notably, the catalyst exhibits high selectivity (98%) and outperforms its homogeneous Re counterpart in terms of activity. By incorporating the Re complex within the COF framework, the hybrid catalyst combines intrinsic light absorption and CS capabilities, leading to enhanced performance in CO<sub>2</sub> reduction (Fig. 14 (a)–(d)). Gopalakrishnan et al. [126] developed a unique method for producing a composite material by combining a hollow nano spherical keto-enamine TpPa-1 COF using single-atom Co-1 T-MoS<sub>2</sub> (TpPa-1/Co-1 T-MoS<sub>2</sub>). This combination has various favourable features, including an appropriate band edge potential and improved charge separation, which significantly increases CO<sub>2</sub> photoreduction efficiency under visible light exposure. The photocatalytic CO<sub>2</sub> reduction efficiency of the TpPa-1/Co-1 T-MoS<sub>2</sub> nano-composite is outstanding, generating about 196 mol g<sup>-1</sup> h<sup>-1</sup> of CO with



**Fig. 14.** (a) The process of synthesising COF and Re-COF is carried out. (b) A perspective from the side and (c) the unit cell structure of COF with AA stacking are presented. (d) The proposed catalytic mechanism for reducing CO<sub>2</sub> is depicted [125]. Reproduced through Copyright © permission.

a high selectivity of 93%. In contrast, the CO production rates of the bare TpPa-1 and Co-1 T-MoS<sub>2</sub> components are roughly 1.23 and 1.6 times lower, respectively, than the TpPa-1/Co-1 T-MoS<sub>2</sub> composite. This demonstrates that the TpPa-1 COF and Co-1 T-MoS<sub>2</sub> have a considerable cumulative impact in improving the specificity and effectiveness of CO<sub>2</sub> photoreduction to CO. The creation of the TpPa-1/Co-1 T-MoS<sub>2</sub> composite demonstrated the potential for synergistic interactions between COF and their transition metal dichalcogenide equivalents to significantly improve CO<sub>2</sub> photocatalytic conversion.

### 6.3. Surface modification

Surface modification is critical in improving COF overall CO<sub>2</sub> reduction efficacy. Key strategies for improving CO<sub>2</sub> emission reductions through surface alteration include: (i) incorporating additional catalytic sites into the COF structure [127]. Metal nanoparticles, metal complexes, and functional groups can act as active sites for CO<sub>2</sub> reduction processes. For example, silver, gold, and copper nanoparticles are commonly used as catalytic sites due to their large surface areas and unique catalytic properties at the nanoscale. These features enhance their ability to activate and reduce CO<sub>2</sub> effectively [128,129]. These nanoparticles also possess high surface energy, which creates numerous reactive sites that enhance CO<sub>2</sub> adsorption and activation. Once CO<sub>2</sub> is captured, it undergoes various reduction processes, resulting in valuable compounds such as methanol, formic acid, and methane [130]. Moreover, it is crucial for these NPs to handle redox events during the catalytic process, as these events significantly influence their activity and stability. Metal complexes play a pivotal role in catalysis within COFs. Typically, these complexes consist of a metal core bonded with organic ligands. The metal center facilitates the active sites for CO<sub>2</sub> activation and adsorption, while the ligands regulate the electrical properties and enhance the stability of the metal complex [131,132]. Additionally, the presence of these catalytic sites improves CO<sub>2</sub> adsorption and activation, resulting in more efficient conversion. (ii) Electron-donating compounds such as amines or hydroxyl groups may be functionalized on the surface of COFs [133]. Among them, amines, carboxylates, and hydroxyl groups can be used as catalytic sites in the COF structure. These groups can connect with CO<sub>2</sub> molecules using a variety of methods, including hydrogen bonding, electrostatic interactions, and chemical bonding. Amines, for example, can react with CO<sub>2</sub> to create carbamate intermediates, which facilitates their activation and subsequent reduction. These functional groups can also boost the electron density surrounding the COF framework, allowing for more efficient electron transfer during the reduction process. These groups boost the electron density of the COF structure, allowing it to interact more effectively with CO<sub>2</sub> molecules. This adjustment improves CO<sub>2</sub> adsorption capability and speeds up the following reduction process. (iii) Surface modification might include the incorporation of redox-active moieties into the COF structure. These moieties may undergo reversible redox reactions, allowing for CO<sub>2</sub> reduction through electrochemistry [134]. However, introducing redox-active functionalities into COF structures is a promising method for improving their ability to eliminate CO<sub>2</sub> by electrochemical route [135]. Redox-active moieties are molecular entities or functional groups capable of reversible oxidation and reduction methods [136]. When incorporated into COFs, these molecular functionalities work as active electron transfer sites, advancing CO<sub>2</sub> conversion. Whereas the insertion of redox-active moieties in COFs may act in various functions. Initially, these moieties can act as localized locations for CO<sub>2</sub> adsorption and activation. Whilst the electrochemical potential of the redox-active centers can be tailored to accommodate the redox potential necessary for CO<sub>2</sub> reduction, enabling efficient catalysis and highly selective specific processes [137,138]. Furthermore, organic radicals, metal-organic complexes, and conjugated polymers, like can serve as redox-active centers when embedded in COFs. These redox active moieties can absorb electrons from an external circuit during the reduction mechanism, permitting CO<sub>2</sub> to be transformed into products such as methane,

carbon monoxide, or formic acid, respectively [139]. Adding more redox-active sites makes the COF more efficient in converting CO<sub>2</sub> to desired products. (iv) During CO<sub>2</sub> reduction processes, COFs can experience degradation or loss of structural integrity. To mitigate these issues, surface modification strategies may include applying protective coatings, functionalizing with stabilizing agents, or employing interfacial engineering techniques. These approaches aim to prevent structural collapse and chemical deterioration of the COFs. (v) Surface modification can improve COF porosity and surface area [140]. Increased surface area means more active sites for CO<sub>2</sub> adsorption, while increased porosity means effective diffusion and transport of reactants and products within the COF structure. These improvements enable COFs to more efficiently absorb, activate, and selectively reduce CO<sub>2</sub>, thereby advancing CO<sub>2</sub> capture and conversion technologies.

## 7. Structural linkage variation in COFs

COFs are commonly categorized based on the covalent bonds formed during synthesis or the constituent building blocks (Fig. 15 and Table 2). These classifications include imine-linked,  $\beta$ -keto-enamine-linked, azine-linked, and conjugated-linked COFs, delineated by the specific type of covalent bond established during their synthesis. On the other hand, triazine- and porphyrin-based COFs are classified according to their building block component. These various categories facilitate the customisation of the structure and properties of COFs to specific applications, making them highly adaptable materials.

### 7.1. Imine-linked COFs

In principle, imine-linked COFs are generated via a condensation synthesis process in which carbonyl-containing aldehydes and ketones react with primary amine precursors to produce imine bonds (-C=N-) [182]. Imine bonds in COFs promote a strong affinity for CO<sub>2</sub>, thereby allowing for better CO<sub>2</sub> absorption [183,184]. Furthermore, imine bonds are exceptionally stable under mild conditions, contributing to the overall stability of the synthesized COFs [184]. Even though imine bonds are susceptible to rehydration and subsequent disintegration under acidic conditions [70], the extended conjugated structure of imine-linked COFs allows for efficient light absorption and the formation of electron-hole pairs [182]. Considering the aforementioned benefits offered by imine bonds, this type of COFs remains of interest for photocatalytic CO<sub>2</sub> reduction under mild conditions.

Two of the imine-linked COFs, TpPa and TpPa-SO<sub>3</sub>H with chemical structures shown in Fig. 16 (a), stand out prominently in their enhanced photocatalytic CO<sub>2</sub> reduction performance. Under identical conditions, the absence of CO<sub>2</sub> yielded no CO production in the COFs (Fig. 16 (b)). However, when subjected to photocatalysis without the presence of CO<sub>2</sub>, the COFs exhibited remarkably low photocatalytic activity. In a more detailed comparison, after 4 h of simulated sunlight irradiation, the CO yields with TpPa-SO<sub>3</sub>H and TpPa were identified at 416.61 and 380.68 mmol g<sup>-1</sup> (Fig. 16 (c)), respectively. This significant increase in CO yield with metalation highlights the efficacy of incorporating -SO<sub>3</sub>H substituents into synthetic materials' monomers. Moreover, the introduction of -SO<sub>3</sub>H substituents not only enhances the CO<sub>2</sub> photoreduction efficiency but also contributes to the overall stability of the photocatalyst. The photodegradation efficiency of TpPa-SO<sub>3</sub>H showed no significant change, and after two reaction cycles, it maintained a constant CO yield (Fig. 16 (d) and (e)). This result indicates the exceptional photocatalytic stability of TpPa-SO<sub>3</sub>H.

### 7.2. $\beta$ -keto-enamine-linked COFs

The tautomerization of an imine bond in the presence of enol functional groups results in the formation of  $\beta$ -keto-enamine-linked COFs. When compared to imine-linked COFs,  $\beta$ -keto-enamine linkages (-C(=O)-C=C-NH-) are more chemically stable as a result of this transition

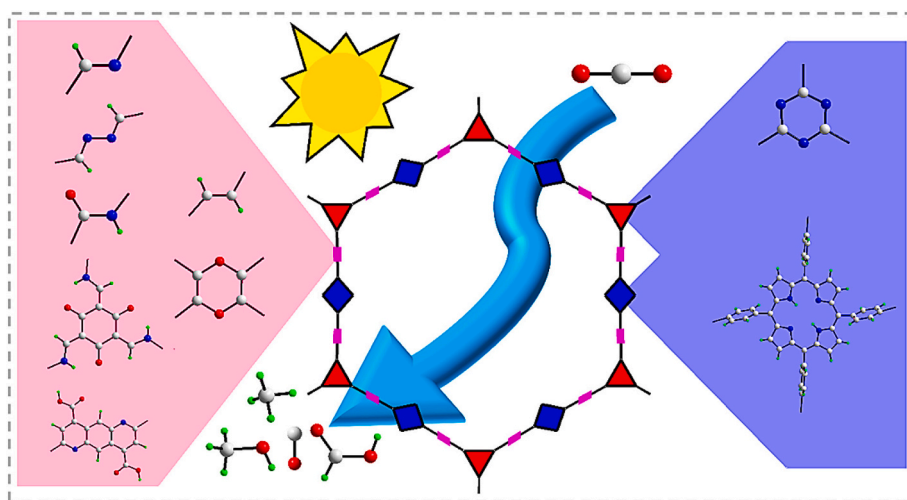


Fig. 15. Categorization of reported COFs with photocatalytic CO<sub>2</sub> reduction functionality.

[141]. The observed improved stability is achieved by the presence of  $\beta$ -keto-enamine linkages, thereby preventing the hydrolysis of the imine bond back to amine and carbonyl compounds [110,151,181,185]. Given their excellent stability,  $\beta$ -keto-enamine-linked COFs are highly sought-after for photocatalytic CO<sub>2</sub> reduction applications because they can act as reliable and persistent photocatalysts.

The series of  $\beta$ -keto-enamine-linked TpBD-X COFs, where X = (OCH<sub>3</sub>)<sub>2</sub>, H<sub>2</sub>, (CH<sub>3</sub>)<sub>2</sub>, and (NO<sub>2</sub>)<sub>2</sub>, exhibit notable photocatalytic activity in the reduction of CO<sub>2</sub> to formic acid (HCOOH). The chemical structures of these COFs are illustrated in Fig. 17 (a). This process is distinctly demonstrated by the absence of a photocatalyst or in the dark, emphasizing the true photocatalytic behaviour. Among the various TpBD-X COFs, TpBD-H<sub>2</sub>, TpBD-(OCH<sub>3</sub>)<sub>2</sub>, and TpBD-(CH<sub>3</sub>)<sub>2</sub> emerge as standout performers, showcasing significantly higher photocatalytic activities of 45.7, 108.3 and 86.3  $\mu\text{mol g}^{-1} \text{h}^{-1}$ , respectively (Fig. 17 (b)). In contrast, TpBD-(NO<sub>2</sub>)<sub>2</sub> exhibits a relatively lower photocatalytic activity of 22.2  $\mu\text{mol g}^{-1} \text{h}^{-1}$  under visible-light irradiation. This variance in performance highlights the impact of the specific functional groups on the ability of COFs to catalyse CO<sub>2</sub> reduction. Furthermore, the stability and reproducibility of TpBD-(OCH<sub>3</sub>)<sub>2</sub> as an illustrative example were investigated through a series of five-run and 30 h experiments, as demonstrated in Fig. 17 (c) and (d). The photocatalyst demonstrates a consistent and reproducible activity across successive runs, highlighting its durability in the CO<sub>2</sub> reduction system. This stability is further supported by the lack of discernible differences in various analytical measurements, including TGA patterns, as shown in Fig. 17 (e), between the fresh and used catalyst samples. Such uniformity indicates the superior stability and reusability of TpBD-(OCH<sub>3</sub>)<sub>2</sub> during the reaction. The electron-donating ability of substituent groups in the TpBD framework follows an order of -OCH<sub>3</sub> > -CH<sub>3</sub> > -H > -NO<sub>2</sub>. This observation leads to the conclusion that an electron-donating substituent group in the TpBD framework significantly enhances the photocatalytic reduction of CO<sub>2</sub> by improving the photogenerated charge, contributing to the overall efficacy of the process. In essence, the metalation of COFs introduces not only enhanced photocatalytic activity but also stability and reproducibility, paving the way for more efficient and sustainable CO<sub>2</sub> reduction strategies.

### 7.3. Azine-linked COFs

Azine-linked COFs are highly porous materials formed from the condensation of hydrazine and aldehyde-containing building blocks via covalent bonds [162,186]. The distinctive properties of these COFs are closely related to the nitrogen-rich azine linkages that increase the efficiency in capturing CO<sub>2</sub>. Furthermore, including a conjugated system

in these frameworks facilitates effective electron delocalization and improved exciton separation [91]. However, similar to imine bonds, azine bonds may be susceptible to hydrolysis. This should be carefully considered in the design of COFs to prepare highly stable and durable azine-linked COFs.

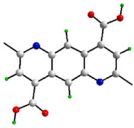
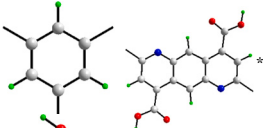
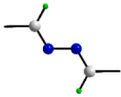
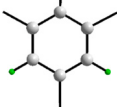
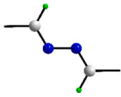
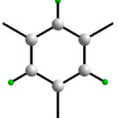
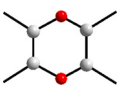
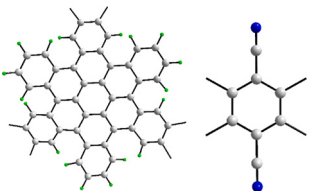
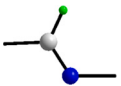
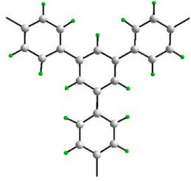
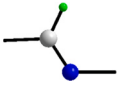
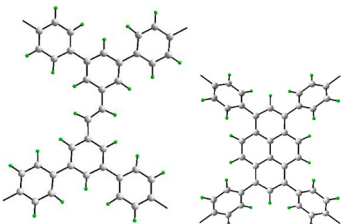
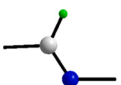
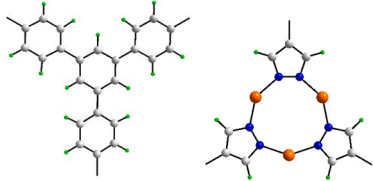
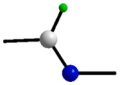
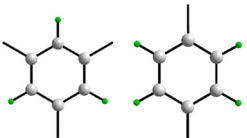
ACOF-1 (Fig. 18 (a)) and N<sub>3</sub>-COF (Fig. 18 (b)) are examples of COFs that effectively transform CO<sub>2</sub> into valuable CH<sub>3</sub>OH in the gas phase. The outcomes of their experiments are truly remarkable: over 24 h of photo irradiation, N<sub>3</sub>-COF exhibited an impressive CH<sub>3</sub>OH yield of 13.7  $\mu\text{mol g}^{-1}$ , significantly outperforming ACOF-1, which yielded 8.8  $\mu\text{mol g}^{-1}$  (Fig. 18 (c)). In addition, both ACOF-1 and N<sub>3</sub>-COF proved to be superior to gC<sub>3</sub>N<sub>4</sub>, which generated 4.8  $\mu\text{mol g}^{-1}$  of CH<sub>3</sub>OH within the same time frame. This disparity in the performance of N<sub>3</sub>-COF and ACOF-1 can be attributed to their higher adsorption affinity, owing to their azine-based COF structure, facilitating more efficient CO<sub>2</sub> conversion. Even when faced with reduced CO<sub>2</sub> concentrations, as low as 1% and diluted by nitrogen, N<sub>3</sub>-COF continued to exhibit remarkable results, with a yield of 9.9  $\mu\text{mol g}^{-1}$  CH<sub>3</sub>OH (Fig. 18 (d)), demonstrating the exceptional selective adsorption capabilities of the catalysts. Moreover, the eco-friendly aspect of these catalysts shines through their reusability, as evidenced by a five-run cycling test (Fig. 18 (e-f)). Although there was a slight decrease in CH<sub>3</sub>OH production during the initial two cycles, the recyclability of the catalyst was unmistakably confirmed, offering a sustainable approach to CO reduction.

### 7.4. Olefin-linked COFs

Knoevenagel or Aldol condensation processes are commonly employed to prepare olefin-linked covalent organic frameworks (COFs) [187–190]. These reactions culminate in forming olefin bonds, essential for endowing olefin-linked COFs with distinctive characteristics. Notably, these COFs exhibit excellent chemical stability, facilitating them to tolerate severe conditions and maintain structural integrity over long periods [19,187,191]. Aside from their structural stability, olefin-linked COFs have a  $\pi$ -conjugated system within their structure that facilitates the efficient delocalization of  $\pi$ -electrons [179,192], resulting in better charge transfer and light absorption [54,55]. The enhanced light harvesting capacity of these COFs is especially beneficial for photocatalytic CO<sub>2</sub> reduction, as efficient light utilization is essential for optimal CO<sub>2</sub> conversion into useful substances. However, it is important to note that the synthesis of olefin-linked COFs is challenging because it requires precise control over the formation of olefin bonds [150]. Despite this limitation, the notable stability and elevated photocatalytic capabilities of olefin-linked COFs make them highly appealing for a variety of applications. More research and development are necessary to

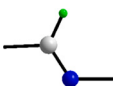
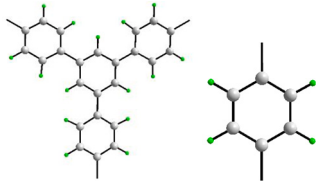
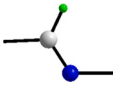
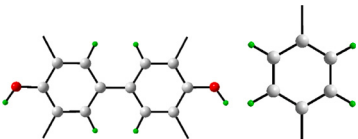
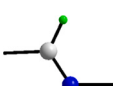
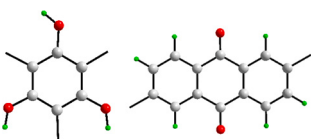
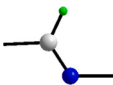
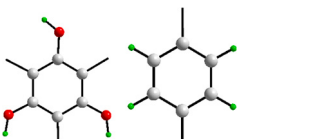
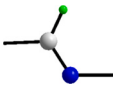
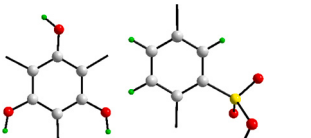
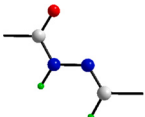
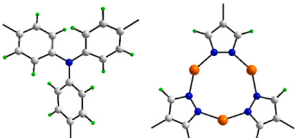
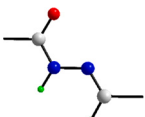
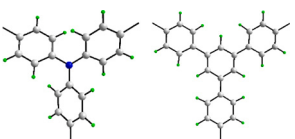
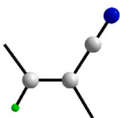
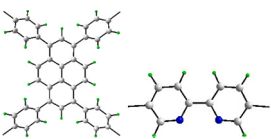
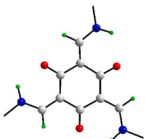
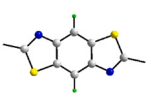
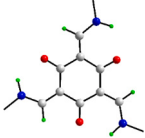
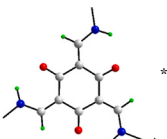
**Table 2**

Classification of COFs based on linkages and building blocks. Color code: H (green), C (grey), N (blue), O (red), S (yellow), Cl (purple), Br (oliver), Co (brown), Ni (pink), Cu (orange), Ru (teal) and Zn (light blue).

COFs	Category	Linkage	Building Block	Ref	Performance
QL-COF	4-Carboxylquinoline-linked			[94]	156 mmol g <sup>-1</sup> h <sup>-1</sup> CO production
HCOF-1	Azine-linked			[141]	202.4 and 57 μmol g <sup>-1</sup> production of Co and CH <sub>4</sub> respectively
ACOF-1	Azine-linked			[91,142]	8.8 μmol g <sup>-1</sup> MeOH production within 24 h
HBC-TFPN	Dioxin-linked			[92]	15.4 μmol g <sup>-1</sup> of CO production within 2 h
0 N-COF	Imine-linked			[143]	No CO <sub>2</sub> reduction
EPPT-COF	Imine-linked			[144]	14.7 μmol g <sup>-1</sup> h <sup>-1</sup> CH <sub>4</sub> production
JNM-1	Imine-linked			[145]	7150 μmol g <sup>-1</sup> h <sup>-1</sup> HCOOH and 592 μmol g <sup>-1</sup> h <sup>-1</sup> CO production
LZU1-COF	Imine-linked			[94]	25 mmol g <sup>-1</sup> h <sup>-1</sup> CO production

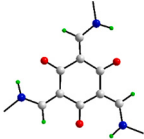
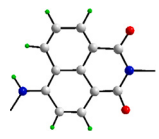
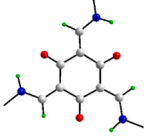
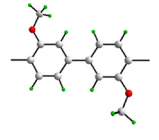
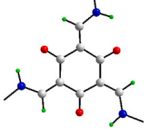
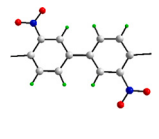
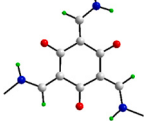
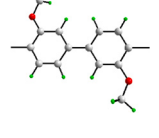
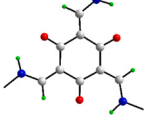
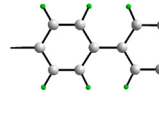
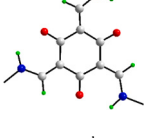
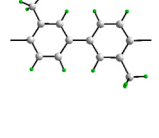
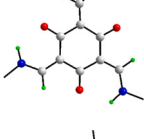
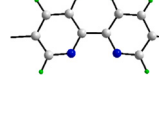
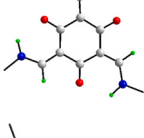
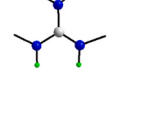
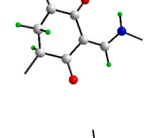
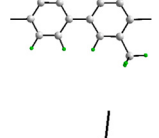
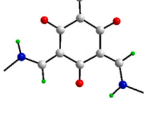
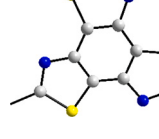
(continued on next page)

Table 2 (continued)

COFs	Category	Linkage	Building Block	Ref	Performance
PDA-TAB	Imine-linked			[146]	31.4 $\mu\text{mol g}^{-1} \text{h}^{-1}$ HCOOH and 23.9 $\mu\text{mol g}^{-1} \text{h}^{-1}$ CO production
TFBD-COF	Imine-linked			[106]	N/A
TFPG-DAAQ COF	Imine-linked			[147]	36 TON HCOOH production
TpPa	Imine-linked			[148]	380.68 $\text{mmol g}^{-1}$ CO production
TpPa-SO <sub>3</sub> H	Imine-linked			[148]	416.61 $\text{mmol g}^{-1}$ CO production (4 h irradiation)
USTB-11(Cu)	N-Acylhydrazone-linked			[149]	274 $\mu\text{mol g}^{-1} \text{h}^{-1}$ CO production
USTB-12	N-Acylhydrazone-linked			[149]	308 $\mu\text{mol g}^{-1} \text{h}^{-1}$ CO production
Bpy-sp2c-COF or sp2c-COFdpy	Olefin-linked			[19,150]	0.03 $\text{mmol g}^{-1} \text{h}^{-1}$ CO production
TpBb-COF/ BTzTp	$\beta$ -keto-enamine-linked			[93,151]	89.9 $\mu\text{mol g}^{-1} \text{h}^{-1}$ CO production [69], 1002 $\mu\text{mol g}^{-1} \text{h}^{-1}$ CO production [134]
HCOF-3	$\beta$ -keto-enamine-linked			[141]	215.68 and 66.9 $\mu\text{mol g}^{-1}$ production of CO and CH <sub>4</sub> respectively

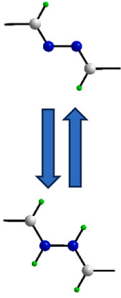
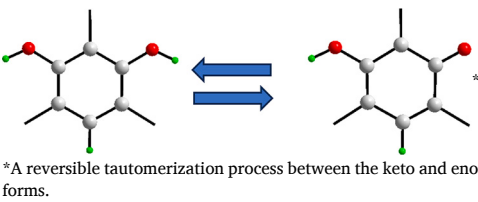
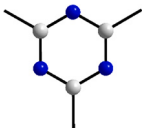
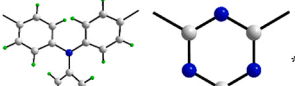
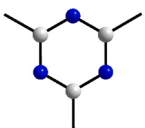
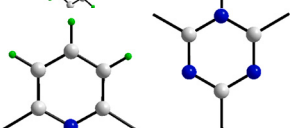
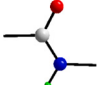
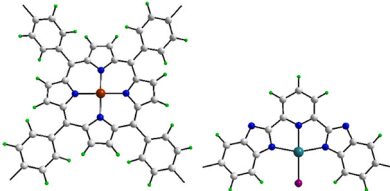
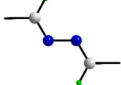
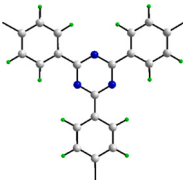
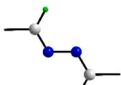
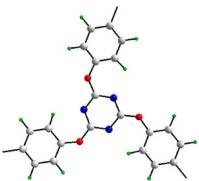
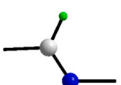
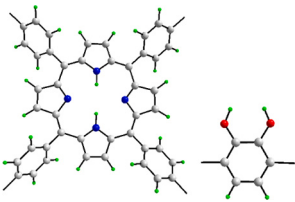
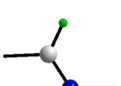
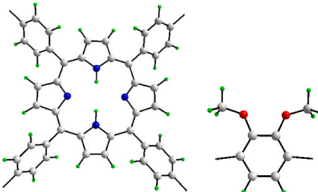
(continued on next page)

Table 2 (continued)

COFs	Category	Linkage	Building Block	Ref	Performance
NAHN-Tp	$\beta$ -keto-enamine-linked			[152]	88.6 $\mu\text{mol}$ within 1 h
TFP-DM COF	$\beta$ -keto-enamine-linked			[153]	0.019 mol HCOOH production (8 h irradiation) and 0.47 mol HCHO (8 h irradiation)
TpBD-(NO <sub>2</sub> ) <sub>2</sub>	$\beta$ -keto-enamine-linked			[154]	22.2 $\mu\text{mol g}^{-1} \text{h}^{-1}$ HCOOH production
TpBD-(OCH <sub>3</sub> ) <sub>2</sub>	$\beta$ -keto-enamine-linked			[154]	108.3 $\mu\text{mol g}^{-1} \text{h}^{-1}$ HCOOH production
TpBD-H <sub>2</sub>	$\beta$ -keto-enamine-linked			[154]	45.7 $\mu\text{mol g}^{-1} \text{h}^{-1}$ HCOOH production
TpBD-(CH <sub>3</sub> ) <sub>2</sub>	$\beta$ -keto-enamine-linked			[154]	86.3 $\mu\text{mol g}^{-1} \text{h}^{-1}$ HCOOH production
TpBpy or COF	$\beta$ -keto-enamine-linked			[102,155,156]	No CO <sub>2</sub> reduction
TP-CON	$\beta$ -keto-enamine-linked			[157]	N/A
TR-OT COF	$\beta$ -keto-enamine-linked			[158]	28% yield of $\alpha$ -Carboxylation and $\beta$ -Carboxylation from styrene
TTzTp	$\beta$ -keto-enamine-linked			[151]	586 $\mu\text{mol g}^{-1} \text{h}^{-1}$ CO production

(continued on next page)

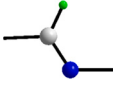
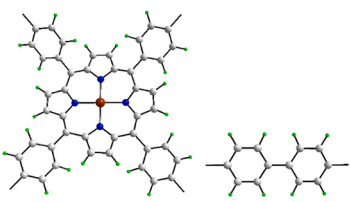
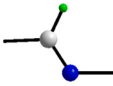
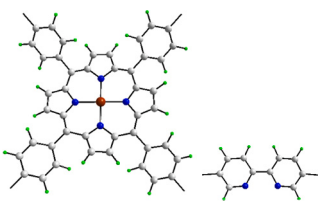
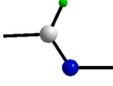
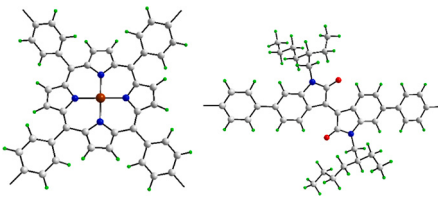
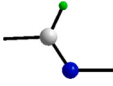
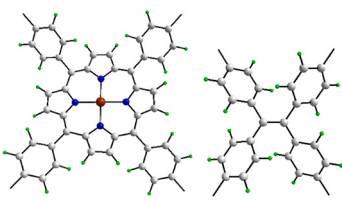
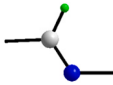
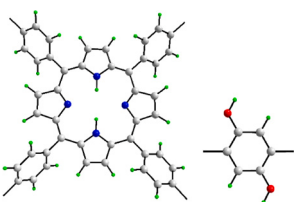
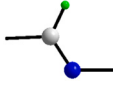
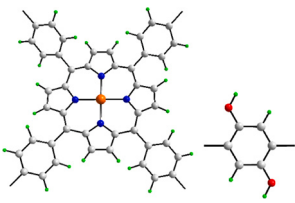
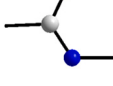
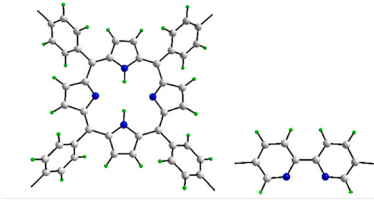
Table 2 (continued)

COFs	Category	Linkage	Building Block	Ref	Performance
HCOF-2	Azine-linked, $\beta$ -keto-enamine-linked	 *Reversible tautomerization	 *A reversible tautomerization process between the keto and enol forms.	[141]	309 and 96 $\mu\text{mol g}^{-1}$ production of CO and $\text{CH}_4$ respectively
DA-CTF	Triazine-based			[159]	9.3 $\mu\text{mol CO}$ production in 2 h
CTF-py	Triazine-based			[160]	13.4 $\mu\text{mol g}^{-1} \text{h}^{-1}$ CO production
CoPor-RuN <sub>3</sub>	Amide-linked, Porphyrin-based			[161]	37.1 $\mu\text{mol g}^{-1} \text{h}^{-1}$ CO and 1.57 $\mu\text{mol g}^{-1} \text{h}^{-1}$ $\text{CH}_4$ production
N <sub>3</sub> -COF	Azine-linked, Triazine-based			[91,162]	13.7 $\mu\text{mol g}^{-1}$ MeOH production within 24 h
TPHH-COF	Azine-linked, Triazine-based			[163]	179 $\mu\text{mol g}^{-1}$ CO production
2,3-DhaTph COF	Imine-linked, Porphyrin-based			[164]	56.6 $\mu\text{mol g}^{-1} \text{h}^{-1}$ CO production
2,3-DmaTph COF	Imine-linked, Porphyrin-based			[164]	71.6 $\mu\text{mol g}^{-1} \text{h}^{-1}$ CO production

(continued on next page)

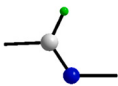
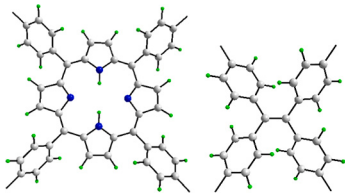
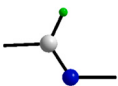
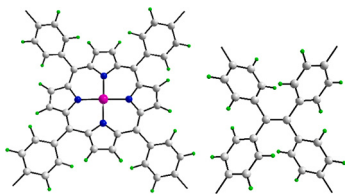
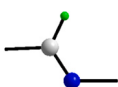
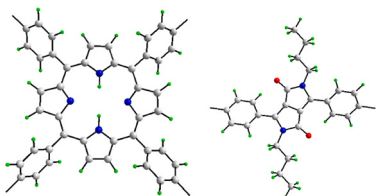
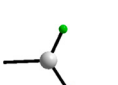
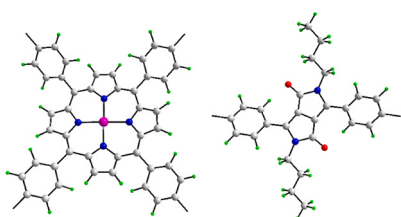
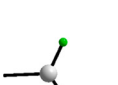
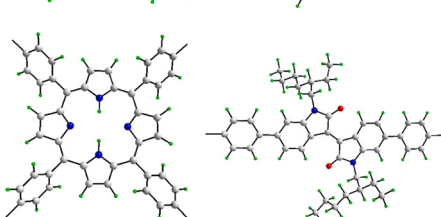
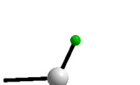
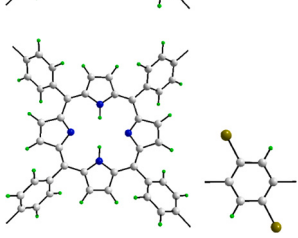

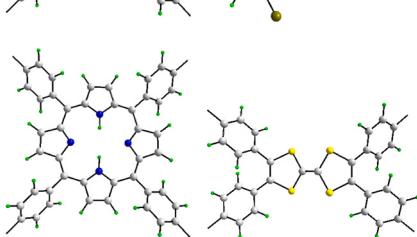


Table 2 (continued)

COFs	Category	Linkage	Building Block	Ref	Performance
COF-367-Co	Imine-linked, Porphyrin-based			[165]	COF-367-Co <sup>II</sup> 48.6 ± 9.25 μmol g <sup>-1</sup> h <sup>-1</sup> HCOOH, 16.5 ± 1.88 μmol g <sup>-1</sup> h <sup>-1</sup> CO, and 12.8 ± 1.88 μmol g <sup>-1</sup> h <sup>-1</sup> CH <sub>4</sub> productions COF-367-Co <sup>III</sup> 93.0 ± 4.63 μmol g <sup>-1</sup> h <sup>-1</sup> HCOOH, 5.5 ± 0.88 μmol g <sup>-1</sup> h <sup>-1</sup> CO, and 10.1 ± 1.12 μmol g <sup>-1</sup> h <sup>-1</sup> CH <sub>4</sub> productions
COF-Bpy-Co	Imine-linked, Porphyrin-based			[96]	No CO <sub>2</sub> reduction
Co-PI-COF	Imine-linked, Porphyrin-based			[99]	50 μmol g <sup>-1</sup> h <sup>-1</sup> HCOO <sup>-</sup> production
CoP-TPE-COF	Imine-linked, Porphyrin-based			[166]	2414 μmol g <sup>-1</sup> h <sup>-1</sup> CO production
DhaTph Tubes	Imine-linked, Porphyrin-based			[167]	8.6 μmol g <sup>-1</sup> h <sup>-1</sup> CO production
DhaTph-Cu Tubes	Imine-linked, Porphyrin-based			[167]	15.9 μmol g <sup>-1</sup> h <sup>-1</sup> CO production
H <sub>2</sub> PBpy-COF	Imine-linked, Porphyrin-based			[168]	No CO <sub>2</sub> reduction

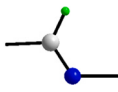
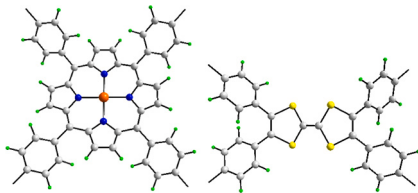
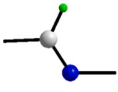
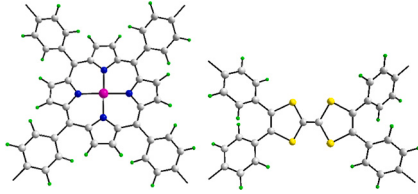
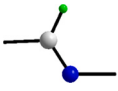
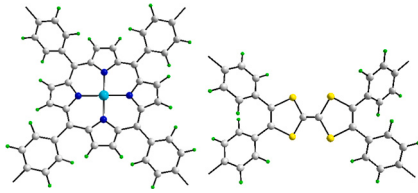
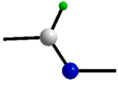
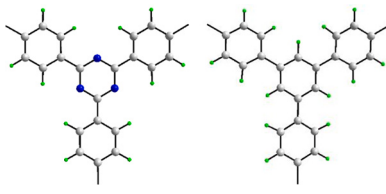
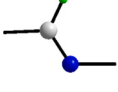
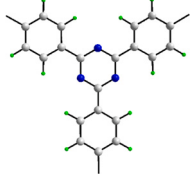
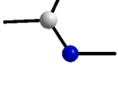
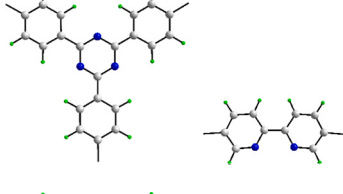
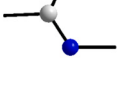
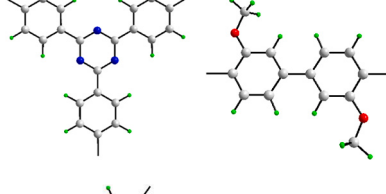
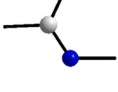
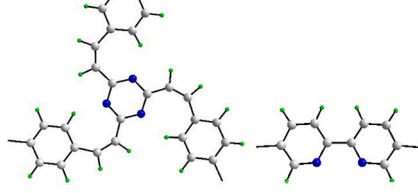
(continued on next page)

Table 2 (continued)

COFs	Category	Linkage	Building Block	Ref	Performance
H <sub>2</sub> P-TPE-COF	Imine-linked, Porphyrin-based			[166]	No CO <sub>2</sub> reduction
NiP-TPE-COF	Imine-linked, Porphyrin-based			[166]	525 μmol g <sup>-1</sup> h <sup>-1</sup> CO production
PD-COF-23	Imine-linked, Porphyrin-based			[169]	20.9 μmol g <sup>-1</sup> h <sup>-1</sup> CO production
PD-COF-23-Ni	Imine-linked, Porphyrin-based			[169]	40 μmol g <sup>-1</sup> h <sup>-1</sup> CO production
PI-COF	Imine-linked, Porphyrin-based			[99]	N/A
TAPBB	Imine-linked, Porphyrin-based			[170]	24.6 μmol g <sup>-1</sup> h <sup>-1</sup> CO production
TTCOF-2H	Imine-linked, Porphyrin-based			[171]	N/A

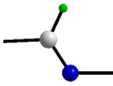
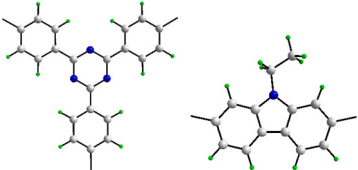
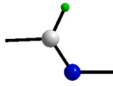
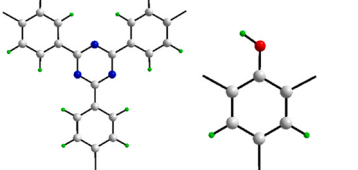
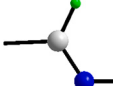
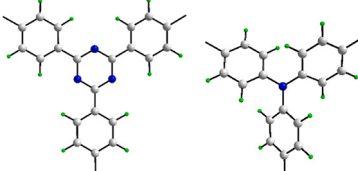
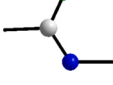
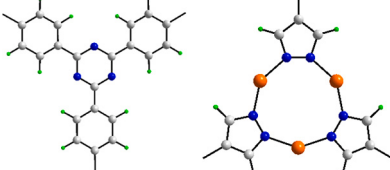
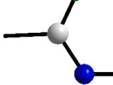
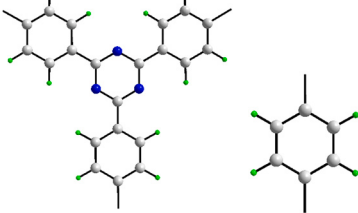
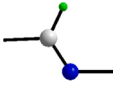
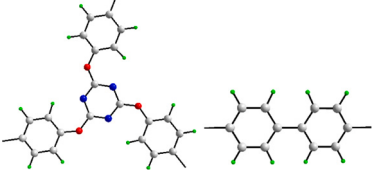
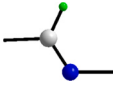
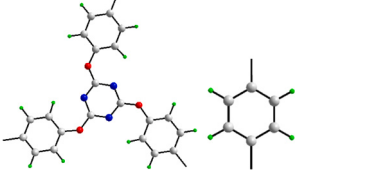
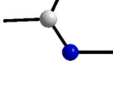
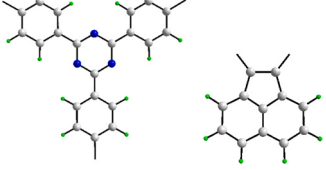
(continued on next page)

Table 2 (continued)

COFs	Category	Linkage	Building Block	Ref	Performance
TTCOF-Cu	Imine-linked, Porphyrin-based			[171]	1.44 $\mu\text{mol g}^{-1} \text{h}^{-1}$ CO production
TTCOF-Ni	Imine-linked, Porphyrin-based			[171]	N/A
TTCOF-Zn	Imine-linked, Porphyrin-based			[171]	2.06 $\mu\text{mol g}^{-1} \text{h}^{-1}$ CO production
1 N-COF TtaTpa	Imine-linked, Triazine-based			[143,145]	89 $\mu\text{mol g}^{-1} \text{h}^{-1}$ (membrane), 32 $\mu\text{mol g}^{-1} \text{h}^{-1}$ (powder) CO production
2 N-COF	Imine-linked, Triazine-based			[143]	310 $\mu\text{mol g}^{-1} \text{h}^{-1}$ (membrane), 98 $\mu\text{mol g}^{-1} \text{h}^{-1}$ (powder) CO production
Bpy-COF TTA-COF	Imine-linked, Triazine-based			[103,172]	3.25 $\mu\text{mol g}^{-1} \text{h}^{-1}$ CO and 11.5 $\mu\text{mol g}^{-1} \text{h}^{-1}$ CH <sub>4</sub> production
COF	Imine-linked, Triazine-based			[173]	30 $\mu\text{mol g}^{-1} \text{h}^{-1}$ CO production
COF-TVBT-Bpy	Imine-linked, Triazine-based			[95]	No CO <sub>2</sub> reduction

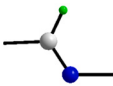
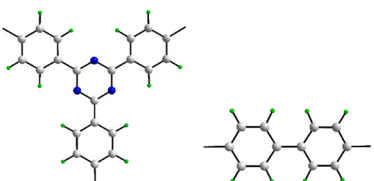
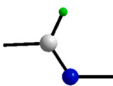
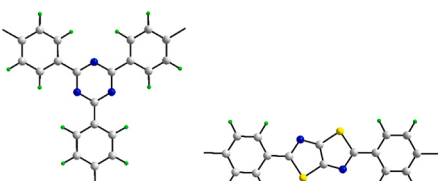
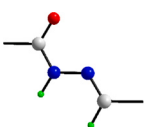
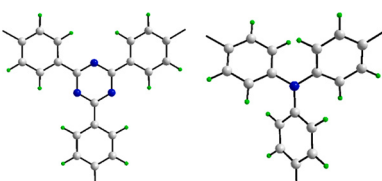
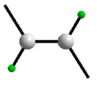
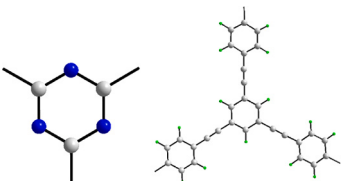
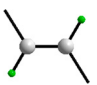
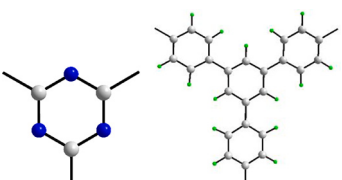
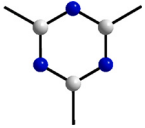
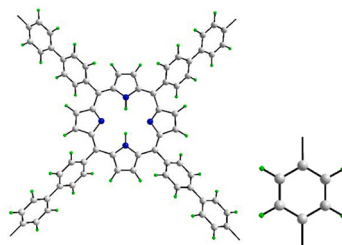
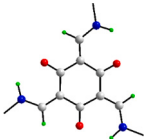
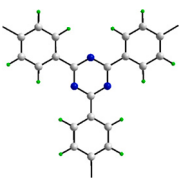
(continued on next page)

Table 2 (continued)

COFs	Category	Linkage	Building Block	Ref	Performance
CT-COF	Imine-linked, Triazine-based			[174]	102.7 $\mu\text{mol g}^{-1} \text{h}^{-1}$ CO production
HB-TAPT	Imine-linked, Triazine-based			[175]	7.4 $\mu\text{mol g}^{-1} \text{h}^{-1}$ CO production
I-COF	Imine-linked, Triazine-based			[176]	N/A
JNM-2	Imine-linked, Triazine-based			[145]	9019 $\mu\text{mol g}^{-1} \text{h}^{-1}$ HCOOH and 835 $\mu\text{mol g}^{-1} \text{h}^{-1}$ CO production
PDA-TTA	Imine-linked, Triazine-based			[146]	65.7 $\mu\text{mol g}^{-1} \text{h}^{-1}$ HCOOH and 30.5 $\mu\text{mol g}^{-1} \text{h}^{-1}$ CO production
TPBD-COF	Imine-linked, Triazine-based			[163]	653 $\mu\text{mol g}^{-1}$ CO production
TPPD-COF	Imine-linked, Triazine-based			[163]	951 $\mu\text{mol g}^{-1}$ CO production
Tr-COF	Imine-linked, Triazine-based			[103]	37.7 $\mu\text{mol g}^{-1} \text{h}^{-1}$ CO production

(continued on next page)

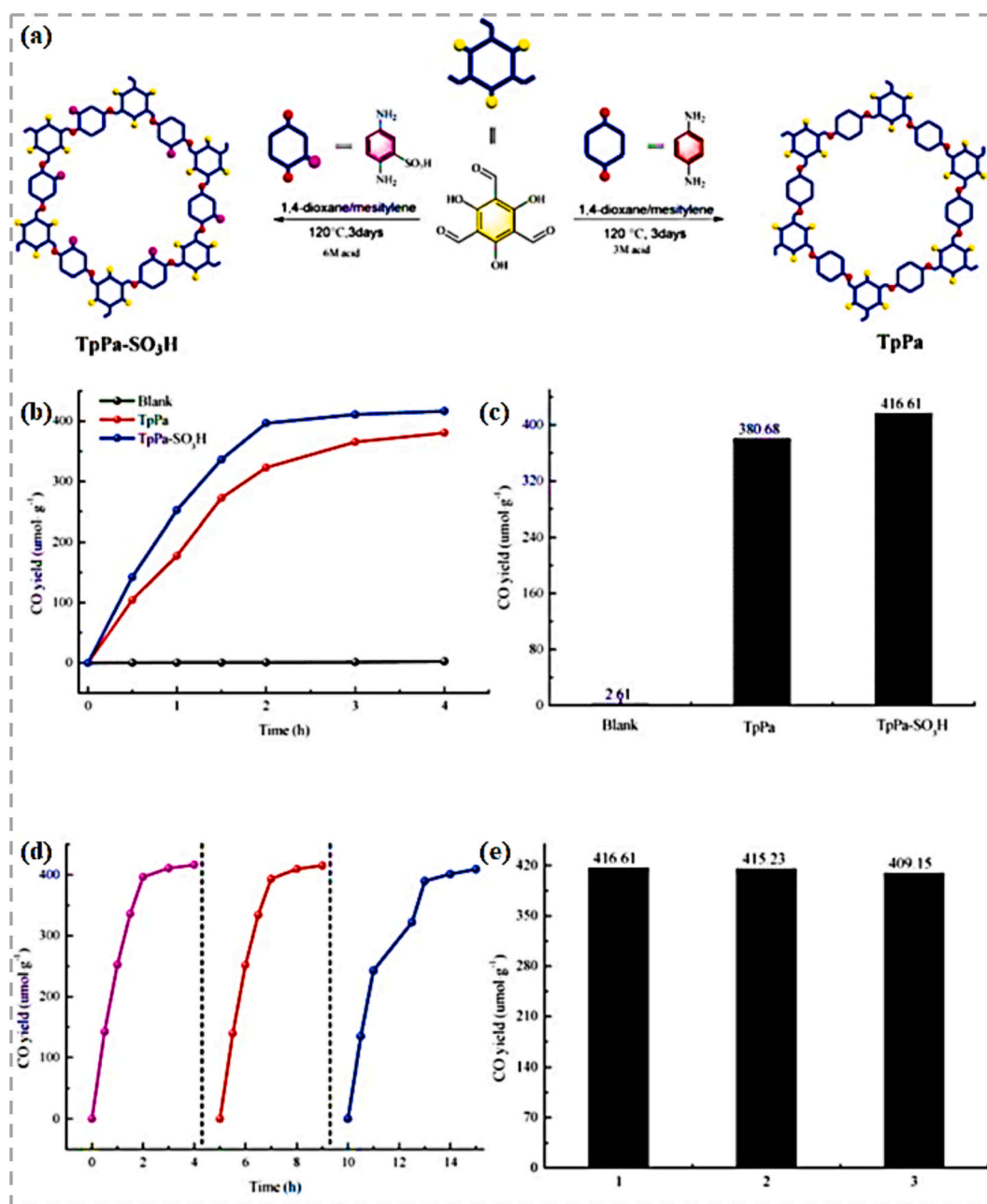
Table 2 (continued)

COFs	Category	Linkage	Building Block	Ref	Performance
TRITER-2	Imine-linked, Triazine-based			[177]	141 TON MeOH, 42 TON HCOOH, and 21 TON HCOH production
Tz-TTA COF	Imine-linked, Triazine-based			[178]	82 $\mu\text{mol g}^{-1} \text{h}^{-1}$ CO production, 0.2 $\mu\text{mol g}^{-1} \text{h}^{-1}$ CH <sub>4</sub> production
H-COF	N-acylhydrazone- linked, Triazine-based			[176]	N/A
BTE-TBD-COF	Olefin-linked, Triazine-based			[179]	382.0 $\mu\text{mol g}^{-1} \text{h}^{-1}$ CO production
TFPB-COF	Olefin-linked, Triazine-based			[179]	109.8 $\mu\text{mol g}^{-1} \text{h}^{-1}$ CO production
Por-CTF	Triazine-linked, Porphyrin-based			[180]	0.21 $\mu\text{mol g}^{-1} \text{h}^{-1}$ CO production
TpTta	$\beta$ -keto-enamine- linked, Triazine-based			[181]	3.5 $\mu\text{mol h}^{-1}$ CO production

address the synthesis issues to exploit the full potential of these materials in a variety of areas.

BTE-TBP-COF and TFPB-COF were synthesized through a base-promoted aldol condensation reaction (Fig. 19 (a)), introducing 2,4,6-trimethyl-*s*-triazine (TMT) and 4,4',4''-(benzene-1,3,5-triyltris(ethyne-2,1-diyl))tribenzaldehyde (BTE-TBD) or 2,4,6-tris(4-formylphenyl)-

1,3,5-benzene (TFPB), respectively. The study aimed to investigate the photocatalytic activity of COFs by varying the degree of  $\pi$ -conjugation. The resulting COFs were characterized using CP/MAS <sup>13</sup>C NMR and FTIR, revealing  $sp^2$ -carbon resonances and distinctive vibrational peaks associated with olefin bonds. Pawley refinement of PXRD patterns confirmed the structural details of the COFs and the introduction of



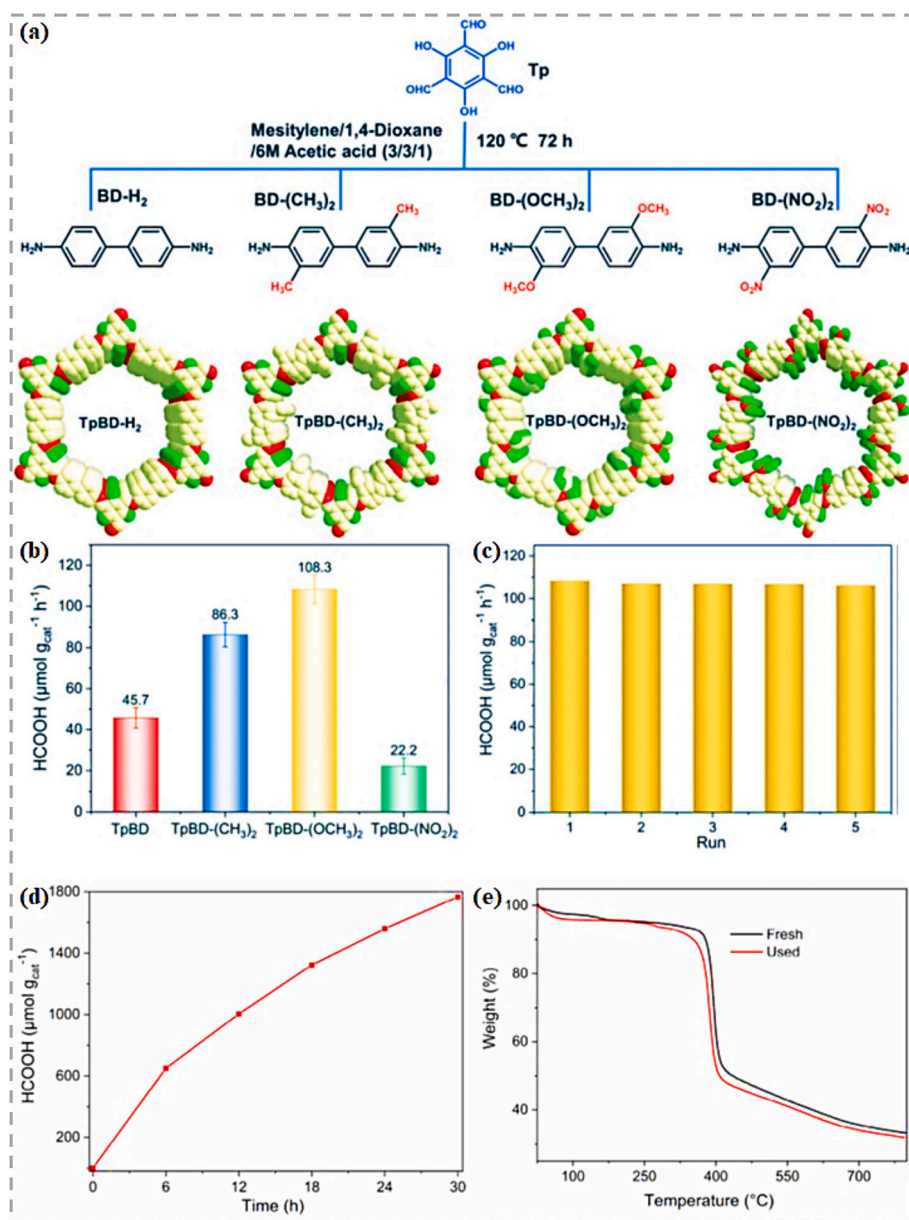
**Fig. 16.** (a) Schematic diagram of the preparation of TpPa-SO<sub>3</sub>H and TpPa photocatalysts. (b) and (c) demonstrates the photocatalytic activity of the samples, while (d) and (e) are the repetitive testing of the CO<sub>2</sub> photoreduction process using TpPa-SO<sub>3</sub>H under simulated solar light irradiation. Reproduced through Copyright © permission.

ethynyl moieties into the  $\pi$ -conjugation system was validated by diffuse reflectance and X-ray photoelectron spectrometry, providing a controllable means to modulate the conjugation degree within the aromatic framework. The olefin-linked  $sp^2$ c-COFs exhibited high thermal stability, as demonstrated by thermogravimetry analysis. Fig. 19 (b) shows the mass spectrum of <sup>13</sup>CO obtained from the photocatalytic CO<sub>2</sub> reduction under <sup>13</sup>CO<sub>2</sub> atmosphere using BTE-TBD-COF. Photocatalytic CO<sub>2</sub> reduction experiments showed that both BTE-TBP-COF and TFPB-COF are good in the reduction and yielding CO with rates of 382.03 and 109.80  $\mu\text{mol g}^{-1} \text{h}^{-1}$  (Fig. 19 (c) and (d)), respectively, under light irradiation in the wavelength range of 320 to 780 nm. Furthermore, the chemical stability of BTE-TBD-COF was well-preserved throughout the catalysis process, as confirmed by XRD patterns, FT-IR spectra, and UV-vis DRS results. Remarkably, the catalytic performance remained as high as 96% even after three cycles (Fig. 19 (e)), demonstrating the

durability and efficiency of this COF in photocatalytic CO<sub>2</sub> reduction.

### 7.5. Amide-linked COFs

The incorporation of amide bonds in amide-linked COFs that connect the building blocks renders these materials unique properties and potential applications. Surprisingly, the development of synthesis methods for this class of COFs has been scarce, leading to limited studies in this domain [22]. Nevertheless, recent work has highlighted the relevance of amide-linked COFs in this application and illustrated their potential capabilities in photocatalytic CO<sub>2</sub> reduction [161]. A two-step procedure is generally used to create amide-linked COFs. Imine-linked COFs are initially formed and then oxidised to produce the required amide-linked COFs [193–195]. The COF framework can incorporate amide bonds using this traditional method. Particularly noteworthy is the



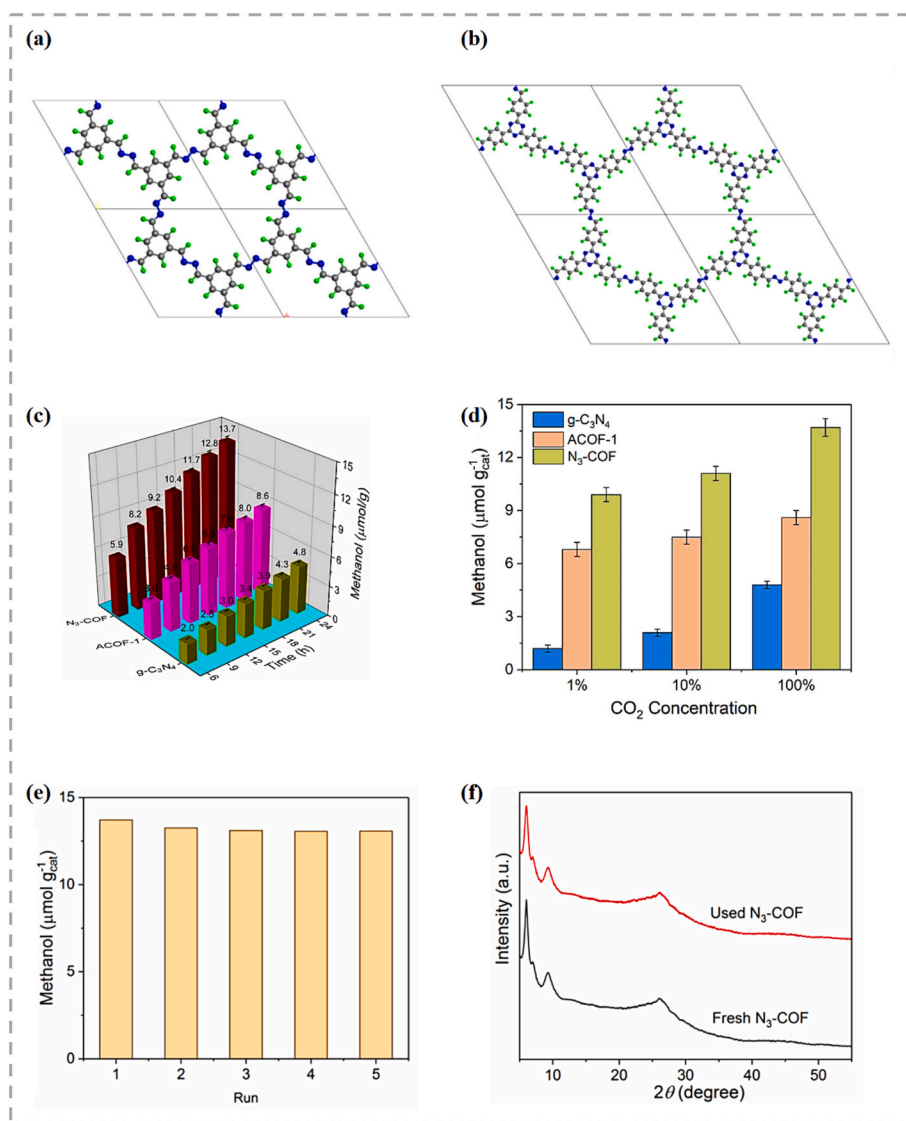
**Fig. 17.** (a) Schematic diagram of the synthetic path for TpBD-X with X = H<sub>2</sub>, (CH<sub>3</sub>)<sub>2</sub>, (OCH<sub>3</sub>)<sub>2</sub>, and (NO<sub>2</sub>)<sub>2</sub>. (b) Amounts of the produced HCOOH over the prepared catalysts upon 6 h of visible-light irradiation (800 nm ≥ λ ≥ 420 nm) (c) Reusability of TpBD-(OCH<sub>3</sub>)<sub>2</sub> in CO<sub>2</sub> reduction upon visible-light irradiation. (d) Long-term stability test of TpBD-(OCH<sub>3</sub>)<sub>2</sub> photocatalytic CO<sub>2</sub> reduction to produce HCOOH and (e) TGA curves of the fresh (black) and the used TpBD-(OCH<sub>3</sub>)<sub>2</sub> after the 5<sup>th</sup> run photocatalytic reaction (red). Reproduced through Copyright © permission. (For interpretation of the references to color in this figure legend, the reader is referred to the web version of this article.)

recent investigation into an alternate one-step technique using liquid nitrogen to directly synthesise amide-linked COFs [196]. Although this innovative method streamlines and expedites synthesis, it is critical to recognise the additional cryogenic dangers connected to working with liquid nitrogen.

Amide-linked COFs demonstrate exceptional chemical stability in various solvent environments, making them suitable for vast applications [193]. This inherent stability safeguards its structural integrity and allows it to endure various reactions and environmental factors. However, there are several significant downsides to using amide-linked COFs. The lengthy reaction times required for their synthesis present a considerable obstacle. In addition, high pressures and temperatures are frequently needed in the preparation, which introduces complexity and raises energy expenses. Additionally, the yield of the final product is typically low, which hinders practical scalability [194]. Overcoming

these obstacles is crucial to fully exploiting the potential of amide-linked COFs in various applications.

The CoPor-RuN<sub>3</sub> COF, a remarkable representative, exhibits an average CO/CH<sub>4</sub> yield of 37.1/1.57 μmol g<sup>-1</sup> h<sup>-1</sup>, showcasing an exceptional total photoactivity of 86.8 μmol g<sup>-1</sup> h<sup>-1</sup>, being 25.5 and 4.5 times higher than the individual CoPor and RuN<sub>3</sub> monomers, respectively (Fig. 20 (a) and (b)). Crucially, in the absence of the photocatalyst, CO<sub>2</sub> gas, or visible light illumination, no observable reduction product of CO<sub>2</sub> is detected, implying that the CO/CH<sub>4</sub> yields result from the photoreduction of CO<sub>2</sub>. The stability of CoPor-RuN<sub>3</sub> is a key highlight, evidenced by the investigation involving four consecutive runs, each lasting 3 h under λ ≥ 400 nm light irradiation. The cumulative CO/CH<sub>4</sub> yields reveal a mere 5.4% deactivation after these four runs, showcasing excellent photostability. Furthermore, the post-cycling analysis confirms the durability of CoPor-RuN<sub>3</sub>. The FESEM image of



**Fig. 18.** Structures of (a) ACOF-1 and (b) N<sub>3</sub>-COF. (c) Amount of the CH<sub>3</sub>OH produced as a function of irradiation time using g-C<sub>3</sub>N<sub>4</sub>, ACOF-1 or N<sub>3</sub> – COF as photocatalyst. (d) Effects of CO<sub>2</sub> concentration on the photocatalytic performance of g-C<sub>3</sub>N<sub>4</sub>, ACOF-1 or N<sub>3</sub> – COF under visible light irradiation. (e) Reusability of N<sub>3</sub>-COF in the photocatalytic reduction of CO<sub>2</sub> upon visible light irradiation. (f) XRD patterns of the fresh (black) and used N<sub>3</sub>-COF after the 5th run photocatalytic reaction (red). Reproduced through Copyright © permission. (For interpretation of the references to color in this figure legend, the reader is referred to the web version of this article.)

the COF after the cycling test indicates no discernible change in morphology and microstructure as compared to its original state (Figs. 20 (c) and (d)). Additionally, the high-resolution XPS spectra (Fig. 20 (e–i)) of the recovered CoPor-RuN<sub>3</sub> after a 12 h illumination closely resembles that of the fresh counterpart. These findings collectively affirm the potential of amide-linked COFs, particularly exemplified by CoPor-RuN<sub>3</sub>, for prolonged and robust photocatalytic applications, rendering them promising candidates for addressing the challenges of CO<sub>2</sub> reduction.

### 7.6. Dioxin- and 4-carboxyquinoline-linked COFs

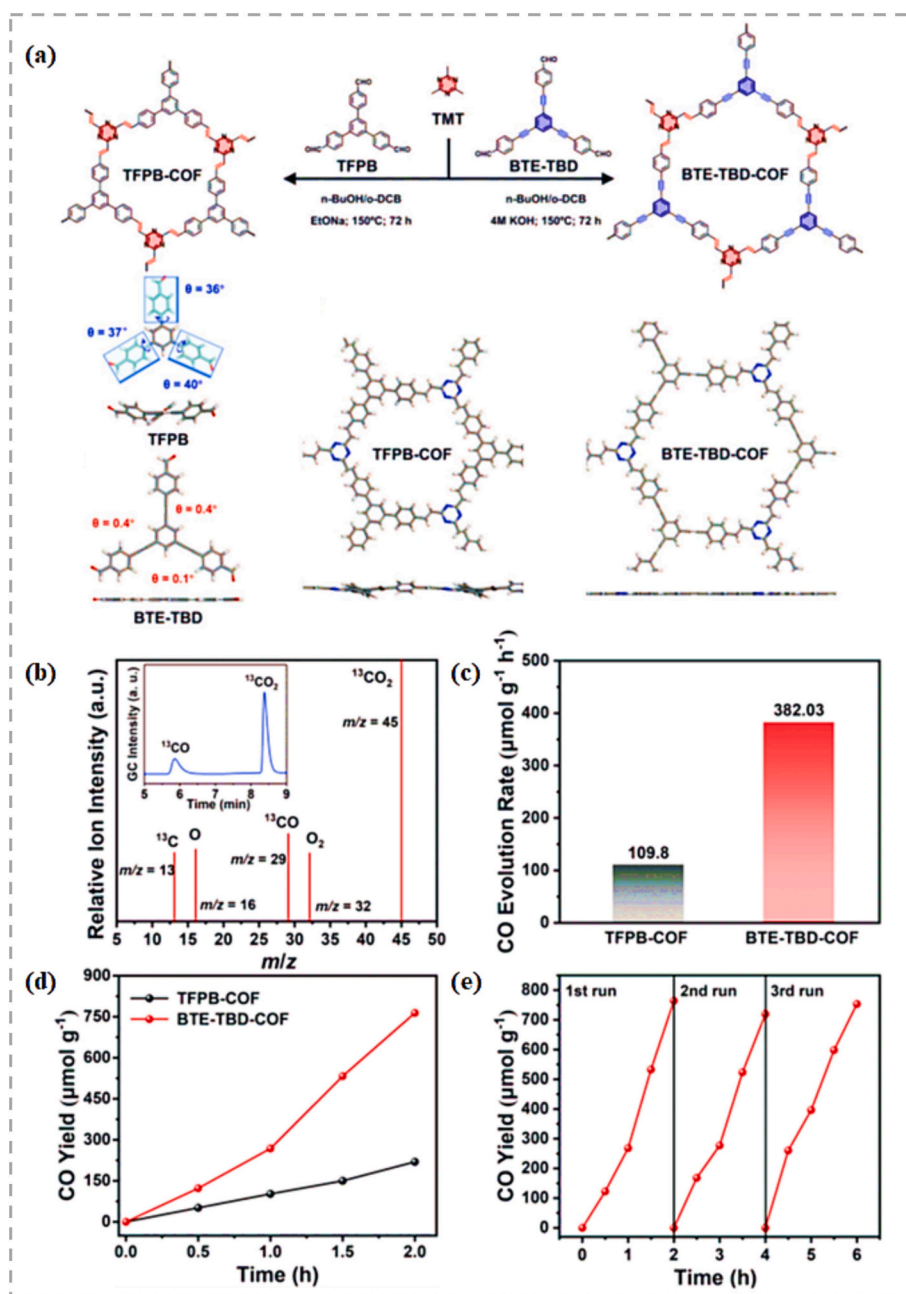
Two additional types of covalent organic frameworks that have been mentioned in relation to photocatalytic CO<sub>2</sub> reduction are those that are dioxin-linked and 4-carboxylquinoline-linked. Due to the formation of robust linkages with ring structures, these frameworks are renowned for their remarkable stability. It is important to note that these COFs are rarely discussed, implying their limited exploration in the field. In the former, the dioxin-linked COFs are prepared from the reaction of

2,3,10,11,18,19-hexahydroxy-cata-hexabenzocoronene and tetrafluorophthalonitrile. Based on the concept of electron donation and acceptance, the building blocks were selected to enhance the photocatalytic activity of the COFs. Despite being one of the strongest links in COFs, generating dioxin-linked COFs is a challenging process [92].

On the other hand, the previously mentioned 4-carboxylquinoline-linked COFs are produced by the Doebner reaction, which involves the interaction of 1,3,5-triformylbenzene with 1,4-diaminobenzene in the presence of glacial acetic acid. The presence of integrated heteroaromatic rings in the COFs greatly enhances their structural robustness [94]. Furthermore, the stability of the linkage is promoted by the multicomponent structure [197]. Similar to that of dioxin-linked COFs, synthesising 4-carboxylquinoline-linked COFs is equally challenging and has restricted their application in other aspects.

LZU1-COF and QL-COF emerge as promising contenders (Fig. 21 (a)), demonstrating significant prowess in photocatalytic reduction of CO<sub>2</sub>. These catalysts exhibit remarkable photocatalytic activities, converting CO<sub>2</sub> into CO as the primary product, accompanied by trace amounts of CH<sub>4</sub>, as validated by the analysis of the GC spectrum (Fig. 21





**Fig. 19.** (a) Synthesis routes for  $\text{sp}^2\text{c-COFs}$  (TFPB-COF and BTE-TBD-COF) and theoretical models of aldehyde monomers and COF structure. (b) Mass spectrum of  $^{13}\text{CO}$  obtained from the photocatalytic  $\text{CO}_2$  reduction under  $^{13}\text{CO}_2$  atmosphere using BTE-TBD-COF. (c) CO evolution rate of photocatalytic carbon dioxide reduction performance of TFPB-COF and BTE-TBD-COF. (d) Time courses of CO production during 2 h experiment. (e) Cycling production of CO using BTE-TBD-COF as the photocatalyst. Reproduced through Copyright © permission.

(b) and (c). Among the two, QL-COF exhibits significantly superior photocatalytic performance, achieving a CO production rate of  $156 \text{ mmol g}^{-1} \text{ h}^{-1}$ , which is six times higher than the  $25 \text{ mmol g}^{-1} \text{ h}^{-1}$  achieved by LZU1-COF (Fig. 21 (d)). This superior performance of QL-COF can be attributed to its enhanced capabilities in capturing  $\text{H}_2\text{O}$  and  $\text{CO}_2$ , coupled with superior carrier transfer efficiency. Additionally, the  $\text{CO}_2$  photoreduction capacity of QL-COF exceeds that of traditional photocatalysts such as  $\text{g-C}_3\text{N}_4$  and  $\text{TiO}_2$ , as illustrated in Fig. 21 (e) with the reported data.

### 7.7. Triazine-based COFs

Triazine-based COFs can be synthesized via various techniques, including Friedel-Crafts alkylation, amidine-based polycondensation,

and trimerization of nitrile-containing building blocks [198–200]. These methods lead to synthesising triazine-containing COFs, which exhibit beneficial features. For example, triazine-based COFs are nitrogen-rich, facilitating effective  $\text{CO}_2$  trapping within their porous frameworks [174,201,202]. Triazine-based COFs are potentially useful in carbon capture and storage (CCS) applications due to the presence of nitrogen atoms that improve carbon dioxide adsorption and retention.

Furthermore, given that the triazine moiety has a high electron affinity, it is an effective electron-accepting group within the COF structure [62,203,204]. In conjunction with the COF's fully conjugated building block, this property increases electron mobility within the material [159,174,205]. Electron transport efficiency is critical for various applications, including photocatalytic processes. On top of the above, triazine-based COFs demonstrate excellent chemical stability,

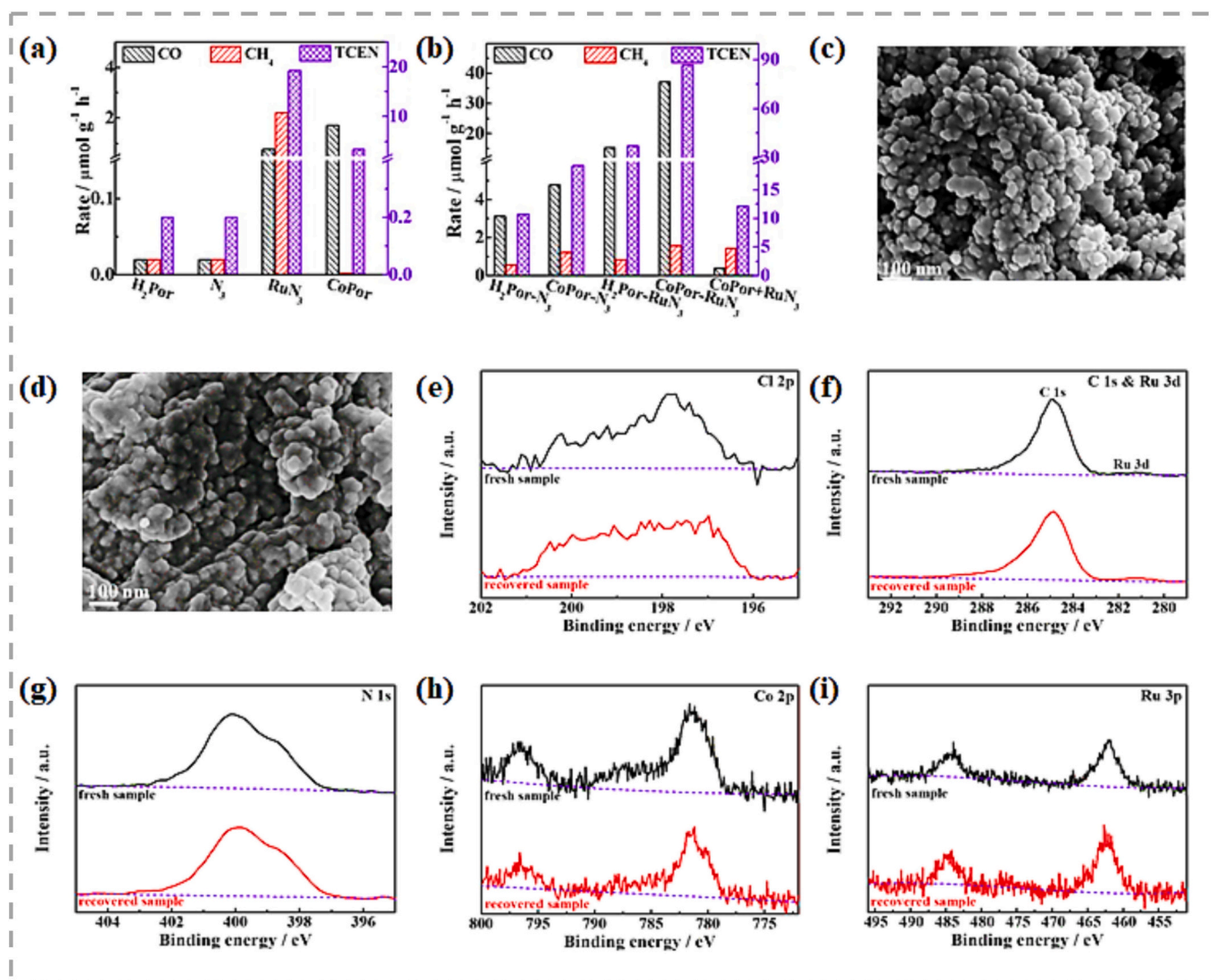


Fig. 20. Comparison of photoreduction of CO<sub>2</sub> activity of (a) various monomers and (b) COFs. FESEM images of the CoPor-RuN<sub>3</sub> (c) before and (d) after cycles test. High resolution XPS spectra of the fresh CoPor-RuN<sub>3</sub> polymer and its recovered sample after 16 h visible light ( $\lambda \geq 400$  nm) illumination for (e) Cl 2p, (f) C 1s & Ru 3d, (g) N 1s, (h) Co 2p, (i) Ru 3p. Reproduced through Copyright © permission.

ensuring their long-term functionality and durability. These COFs can tolerate sturdy chemical conditions [203,206], making them suitable for a wide range of applications requiring degradation and corrosion resistance.

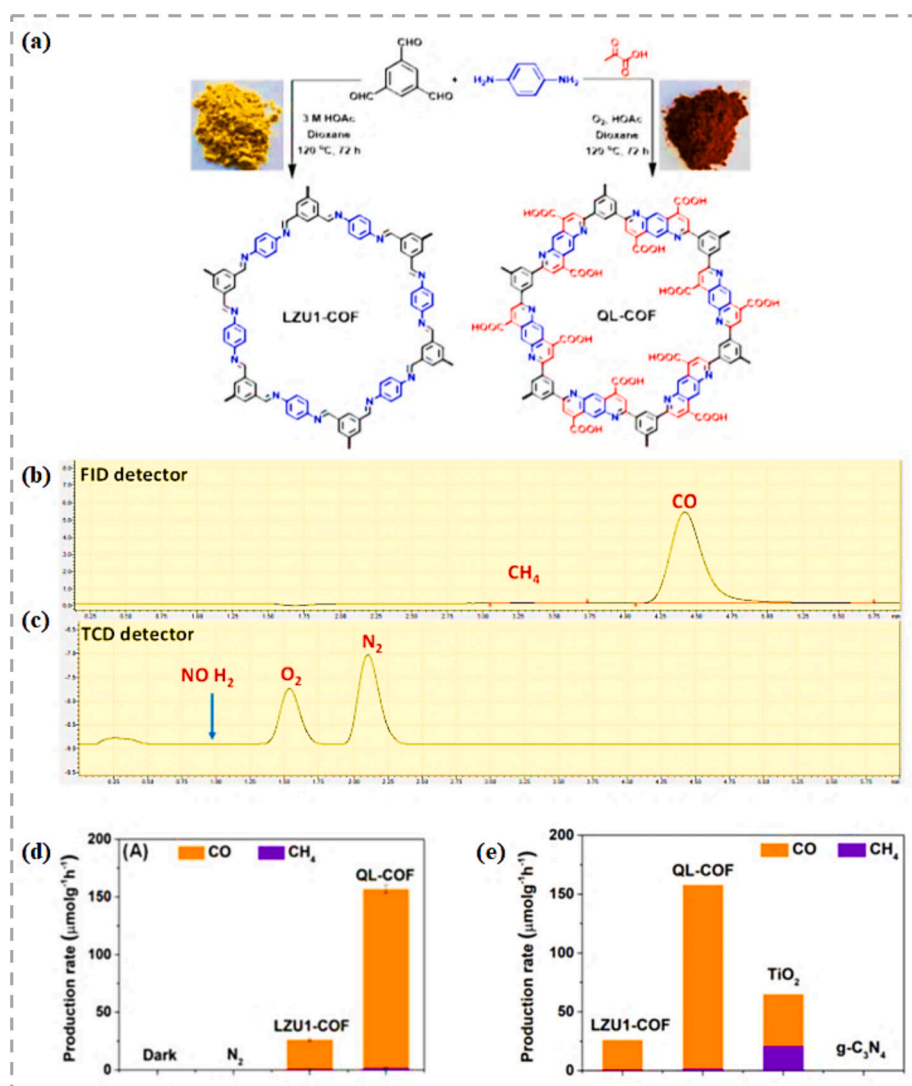
The preparation of 2 N-COF, 1 N-COF, and 0 N-COF (Fig. 22 (a)) involves the polycondensation of amine and aldehyde monomers and strategically manipulates the triazine moiety in the aforementioned COFs. Specifically, 2 N-COF incorporates both amine and aldehyde reactants containing triazine, while 1 N-COF is crafted with only amine monomers featuring triazine, and 0 N-COF omits the triazine moiety altogether. The investigation aims to establish the relationship between triazine content in COFs and the implications on CO<sub>2</sub> adsorption (Fig. 22 (b)). The 2 N-COF, featuring triazine in both amine and aldehyde reactants, exhibits the highest CO<sub>2</sub> uptake at 25 °C, showcasing the direct correlation between triazine concentration and adsorption capacity. The concentration of HOMO orbital on triazine and benzene moieties, as illustrated in Fig. 22 (c), offers insights into the role of triazine as an electron donor. Incorporating electron acceptors, such as imine moieties, enhances electron delocalization within the material, paving the way for improved performance.

The 2 N-COF exhibited a notable reduction rate of 310  $\mu\text{mol g}^{-1} \text{h}^{-1}$ ,

surpassing its counterparts, with 1 N-COF showing a rate of 98  $\mu\text{mol g}^{-1} \text{h}^{-1}$ , and 0 N-COF displaying no reduction activity, as depicted in Fig. 22 (d). Additional confirmation was derived from experiments conducted under dark conditions, revealing the absence of CO<sub>2</sub> reduction in 2 N-COF. This observation emphasizes the critical role of triazine in promoting photocatalytic processes, as illustrated in Fig. 22 (e). Notably, 2 N-COF can endure 16 cycles of 4 h photocatalysis processes. It maintains high stability, as confirmed by PXRD and FTIR analyses, although the CO production rate experiences a slight drop to 287  $\mu\text{mol g}^{-1} \text{h}^{-1}$  after cycling experiments.

### 7.8. Porphyrin-based COFs

COFs based on porphyrin comprised of a porphyrin component capable of forming covalent bonds with other building blocks such as imine [171], amide [161], triazine [180], etc. The electron donor or acceptor properties of the porphyrin component vary in accordance with its interactions with other framework components. When an electron donor component is present, porphyrin serves as an electron acceptor [166]. When combined with an electron acceptor component, porphyrin can act as an electron donor [207]. The COF environment strongly



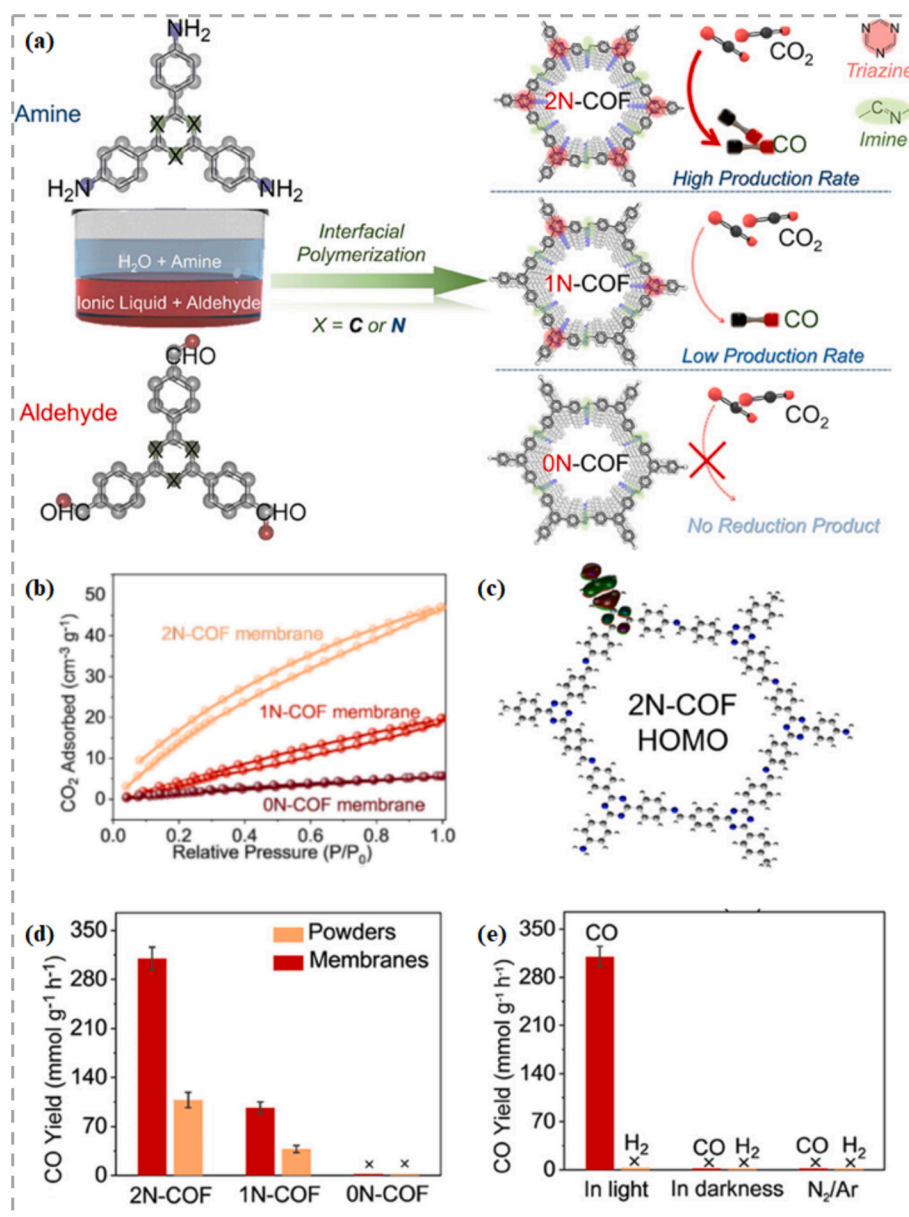
**Fig. 21.** (a) Preparation routes of LZU-COF and QL-COF. (b) GC-FID spectrum photocatalytic reaction of CO<sub>2</sub> over QL-COF. (c) GC-TCD spectrum photocatalytic reaction of CO<sub>2</sub> over QL-COF. (d) Photocatalytic production rates of CO<sub>2</sub> reduction under various reaction conditions (e) Average production rates from CO<sub>2</sub> photoreduction over LZU1-COF, QL-COF, TiO<sub>2</sub> and g-C<sub>3</sub>N<sub>4</sub> for 5 h. Reproduced through Copyright © permission.

influences the donor-acceptor nature of porphyrin in COFs, and this characteristic enables the development of a robust electron transport system, which improves the COF's overall performance.

On the other hand, the coordinated metal ion within the porphyrin unit is capable of functioning as a catalytic active site, allowing for a diverse spectrum of catalytic processes [165]. The judicious selection of metal ions for coordination in porphyrin-based COFs enables delicate control over the photophysical and electrical properties of the materials, allowing for the production of COFs with tailored functionality [208]. The porphyrin component of the COF structure may also function as a photosensitizer, thereby increasing the efficiency of energy transfer processes and allowing for more effective light harvesting [168]. Porphyrin-based COFs are emerging as highly promising materials for photocatalytic CO<sub>2</sub> reduction. Their enhanced light absorption and energy conversion capabilities significantly boost the efficiency of CO<sub>2</sub> conversion processes.

The introduction of Co<sup>II</sup> and Co<sup>III</sup> that coordinated 5,10,15,20-tetra(4-aminophenyl)-porphyrins, resulting in COF-367-Co<sup>II</sup> and COF-367-Co<sup>III</sup> (Fig. 23 (a)), has proven to be a noteworthy advancement. These cobalt-coordinated COFs, synthesized through a condensation reaction between the Co-porphyrin and 4,4'-biphenyldicarboxaldehyde, present a compelling model for investigating the impact of the spinning state of

metal centre on photocatalytic CO<sub>2</sub> reduction performance. When subjected to photoirradiation, both COF-367-Co<sup>II</sup> and COF-367-Co<sup>III</sup> exhibit the capability to reduce CO<sub>2</sub> to HCOOH, CO, and CH<sub>4</sub>. COF-367-Co<sup>II</sup> demonstrates a reduction rate of  $48.6 \pm 9.25 \mu\text{mol g}^{-1} \text{h}^{-1}$  for HCOOH,  $16.5 \pm 1.88 \mu\text{mol g}^{-1} \text{h}^{-1}$  for CO, and  $12.8 \pm 1.88 \mu\text{mol g}^{-1} \text{h}^{-1}$  for CH<sub>4</sub>. On the other hand, COF-367-Co<sup>III</sup> exhibits a distinct reduction pattern with rates of  $93.0 \pm 4.63 \mu\text{mol g}^{-1} \text{h}^{-1}$  for HCOOH,  $5.5 \pm 0.88 \mu\text{mol g}^{-1} \text{h}^{-1}$  for CO, and  $10.1 \pm 1.12 \mu\text{mol g}^{-1} \text{h}^{-1}$  for CH<sub>4</sub>. This observed variation in reduction rates is attributed to the different spin states of Co coordination. The spin state of Co plays a pivotal role in influencing the reduction activity. COF-367-Co<sup>II</sup>, with its spin state, produces a higher yield of CO and CH<sub>4</sub>, while COF-367-Co<sup>III</sup>, with a distinct spin state, yields higher amounts of HCOOH compared to its counterpart. The interaction of CO<sub>2</sub> and HCOOH with Co<sup>II</sup> and Co<sup>III</sup> differs, primarily influenced by the spin state, as depicted in Fig. 23 (b). Notably, COF-367-Co<sup>III</sup> involves fewer orbitals in the catalysis process, rendering the release of HCOOH comparatively easier. This observation is further substantiated by the calculated potential energy (Fig. 23 (c)).



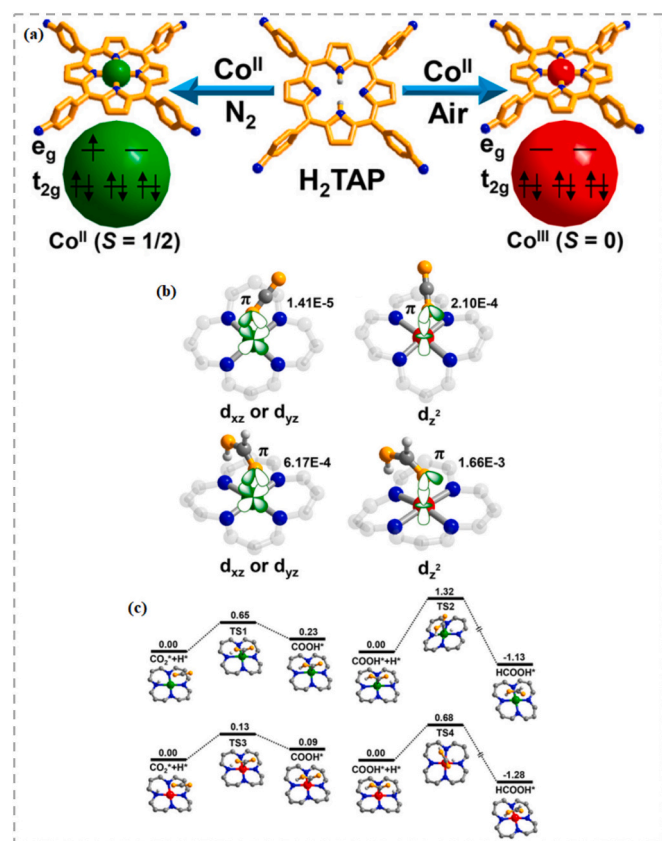
**Fig. 22.** (a) Schematic illustration for synthesising 0 N-COF, 1 N-COF and 2 N-COF membranes at the ionic liquid–H<sub>2</sub>O interface. (b) CO<sub>2</sub> adsorption isotherms of different COF membranes at 25 °C. (c) HOMO of the 2N-COF membrane. (d) Catalytic activity of different COF membranes. (e) The catalytic activity of the 2N-COF membrane under various reaction conditions. Reproduced through Copyright © permission.

## 8. Approaches for enhanced photocatalytic CO<sub>2</sub> reduction of COF via structural and property modification

Photocatalytic CO<sub>2</sub> reduction utilizing COFs has considerable potential in tackling climate change concerns, but several crucial parameters govern its effectiveness. To begin, efficient CO<sub>2</sub> capture is vital for ensuring an adequate supply of reactant molecules for the reduction process [209,210]. Furthermore, the light-absorbing capability of COFs plays a vital role in generating photoelectrons, which are required for catalytic activity [211]. Effective separation of electron-hole pairs is also required to reduce recombination and maximize reactive species availability [212]. Other manipulating factors, such as rapid electron transport within COFs, are essential for efficient electron delivery to catalytic active sites and optimum reduction processes [96,213,214]. In addition, for the requisite reduction processes to occur, well-defined catalytic active sites inside COFs are essential [101]. Finally, COF stability is critical for ensuring longevity and resistance to degradation under

particular operating circumstances [19]. The full potential of photocatalytic CO<sub>2</sub> reduction utilizing COFs can be exploited by fully comprehending and optimizing these parameters, paving the path for sustainable and effective conversion of carbon dioxide into value-added products. The following discussion offers insight into approaches to tailoring COFs with improved photocatalytic performance.

Considering the factors mentioned above, several solutions can be employed to generate COFs with optimized photocatalytic performance. By carefully selecting linkages and building units, one tactic entails rationally modifying COF structure and attributes [168]. With this method, porosity can be altered to enhance CO<sub>2</sub> affinity [210], stimulate the separation and formation of electron-hole pairs in an effective manner [215,216], and expedite electron transfers [211,217]. Additional catalytic sites may be provided by including COFs with greater surface areas or by integrating a porphyrin component, both of which may improve overall photocatalytic activity [218]. Another successful strategy is the incorporation of desired derivatives into building blocks



**Fig. 23.** (a) Preparation of COF-367-Co featuring different spin states. (b) Different coupling modes of  $\text{CO}_2$  and  $\text{HCOOH}$  interacting with Co site at different spin states for  $\text{CO}_2$ -adsorbed  $\text{COF-367-Co}^{\text{II}}$ ,  $\text{CO}_2$ -adsorbed  $\text{COF-367-Co}^{\text{III}}$ ,  $\text{HCOOH}$ -interacted  $\text{COF-367-Co}^{\text{II}}$ , and  $\text{HCOOH}$ -interacted  $\text{COF-367-Co}^{\text{III}}$ . The numerical values represent the corresponding OPDOS intensities. (c) Calculated potential energy profile of  $\text{CO}_2$  reduction reaction to  $\text{HCOOH}$  catalysed by  $\text{COF-367-Co}^{\text{II}}$  (top) and  $\text{COF-367-Co}^{\text{III}}$  (bottom). Reproduced through Copyright © permission.

of COFs. Numerous studies have shown that derivative position substantially impacts photocatalytic activity. This method allows for precise band gap tuning of the material [148,154,163], which improves photoelectron generation and light absorption [148,154]. Therefore, the photocatalytic activity of COFs can be optimized, unleashing their greater potential for effective  $\text{CO}_2$  removal through photocatalytic mechanisms.

Metalation is another well-established method for improving COF photoreduction performance (Table 3). Within the COF framework, there are two strategies to accomplish the aforementioned. The first approach involves coordination chemistry at the porphyrin component, which uses accessible coordination vacancies. As previously mentioned, the metal ion employed in coordination greatly impacts the photo-physical and electronic properties of COFs, consequently influencing the intended catalytic performance [208]. The second method involves coordinating the metal onto the open ligating atoms of the frameworks, such as bipyridine. These approaches enable reliable light absorption control by coordinating a photosensitizer, resulting in better separation of electron-hole pairs [96]. The coordinated metal ion can also modulate the coordinating electron deficiency of the building block and alter the flow of delocalized electrons [223–225]. Furthermore, metal ions can serve as catalytic active sites to enhance the overall efficiency of COFs in  $\text{CO}_2$  reduction [103,226].

$\text{M@COF-TVBT-Bpy}$  represents a series of COFs that leverage a metalation approach to enhance their functionality. In comparison to the pristine COF (Fig. 24 (a)), which lacks any anchored metal, metalated

COFs exhibit remarkable advantages. For instance,  $\text{Co@COF-TVBT-Bpy}$  (Fig. 24 (b)) demonstrates significantly improved production rates of CO at  $1835.3 \text{ mmol g}^{-1} \text{ h}^{-1}$ , highlighting the catalytic capability imparted by metal incorporation. Similarly,  $\text{Ni@COF-TVBT-Bpy}$  showcases a substantial generation of CO at  $1141.9 \text{ mmol g}^{-1} \text{ h}^{-1}$ , underlining the efficiency gained through metalation. Moreover, the introduction of various metal ions (Cu, Zn, Mn) in  $\text{M@COF-TVBT-Bpy}$  results in adjustable catalytic activity, influencing the selectivity of CO production within the range of 48.4% to 64.8%, as demonstrated in Fig. 24 (c). This variability shows the significant role played by metal active sites in dictating the outcome of the  $\text{CO}_2$  reduction process. Contrastingly, the pristine COF-TVBT-Bpy, lacking efficient active sites within its framework, exhibits almost negligible activity in CO production. The metal ions anchored in COF-TVBT-Bpy not only act as catalytic centres for  $\text{CO}_2$  conversion but also enable the regulation of the syngas ratio by adjusting the type of metal ion. The absence of either  $\text{CO}_2$  or light irradiation results in a limited reduction of CO, as illustrated in Fig. 24 (d), emphasizing the interdependence of these factors in the photocatalytic conversion process. Control experiments further confirm the indispensability of  $\text{CO}_2$ , light irradiation, photocatalyst, and photosensitizer for efficient syngas production (Fig. 24 (e)). Moreover, the exceptional reusability of  $\text{Co@COF-TVBT-Bpy}$  is demonstrated through five successive cycling experiments (Fig. 24 (f)), which show no notable decline in photocatalytic activity. This highlights the enhanced stability and durability of metalated COFs, demonstrating their effectiveness in the photocatalytic reduction of  $\text{CO}_2$ . Consequently, this reinforces their potential as promising catalysts for sustainable energy conversion applications.

Finally, post-synthetic alteration is an effective method for tailoring the chemical environment of COFs, hence improving their structure and photocatalytic properties [227–229]. Through post-synthetic modification, functional groups containing nitrogen or oxygen can be included to enhance the  $\text{CO}_2$  affinity of COFs, resulting in better  $\text{CO}_2$  trapping within their cavities for effective photoreduction [72]. Furthermore, post-synthetic modifications are implemented to improve the stability of COFs. Converting the imine bond to an amide bond is one effective approach for mitigating hydrolysis in high humidity conditions [194,230]. These post-synthetic alterations are critical for fine-tuning COFs, allowing for greater  $\text{CO}_2$  capture and improved stability and facilitating successful photocatalysis.

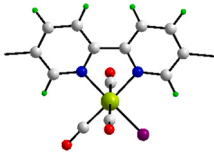
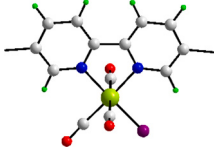
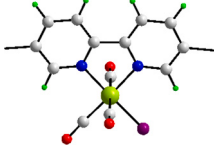
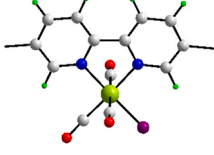
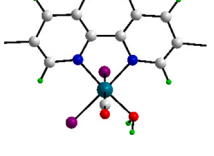
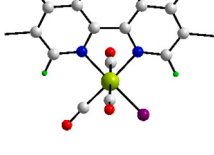
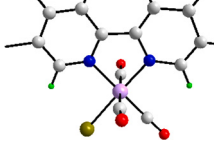
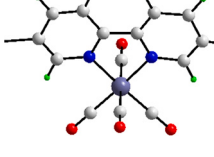
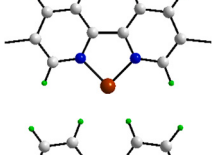
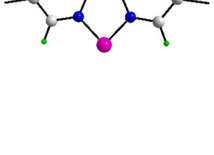
## 9. Factors affecting the photocatalytic activity of COFs for $\text{CO}_2$ reduction

It is essential to comprehend the elements that impact the photocatalytic capability of COFs in reducing  $\text{CO}_2$  to produce prominent materials for sustainable development. Several factors affect the performance of COFs in this process, including their structure and composition, incorporation of metal ions as catalytic sites, and selection of co-catalysts, among others. This section aims to provide an understanding of these factors that can enhance the photocatalytic efficiency of COFs. A fundamental principle modulating the photocatalytic activity of COFs is the bandgap of the material. COFs with a narrow bandgap efficiently absorb visible light, leading to enhanced photocatalytic activity, while those with a wide bandgap absorb UV light, resulting in lower photocatalytic activity. Thus, tuning the bandgap is a critical factor in enhancing the photocatalytic performance of COFs.

The structure and composition of the COF also play a crucial role in its photocatalytic performance. The choice of donor and acceptor units, as well as the type of covalent linkage used to assemble the framework, can influence its electronic properties and surface area. A recent study showed that N-acylhydrazone-linked COFs (H-COF) that contain a triphenylamine donor and a triphenyl-1,3,5-triazine acceptor and incorporated Ni ions into the framework produced H-COF-Ni that exhibited higher photocatalytic activity for  $\text{CO}_2$  reduction than their imine-linked counterparts due to the stronger affinity between  $\text{CO}_2$  molecules and Ni


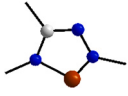
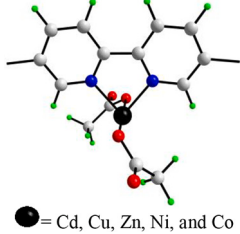
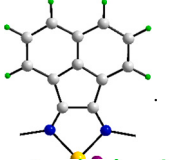
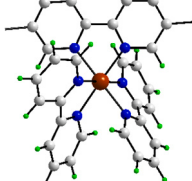
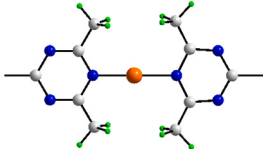
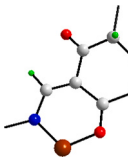
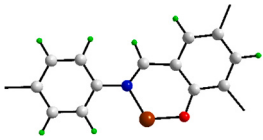
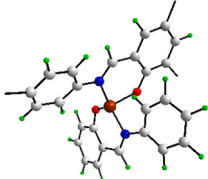
**Table 3**

Metalation of COFs for desired functionality. Color code: H (green), C (grey), N (blue), O (red), S (yellow), Cl (purple), Br (oliver), Co (brown), Ni (pink), Cu (orange), Mo (blue-grey), Ru (teal), Re (lime) and Fe (gold).

COF	Type	Coordination component	Functionality	Ref	Performance
H <sub>2</sub> PreBpy-COF	Imine-linked, Porphyrin-based		Catalytic active site	[168]	1200 $\mu\text{mol g}^{-1} \text{h}^{-1}$ CO and 447 $\mu\text{mol g}^{-1} \text{h}^{-1}$ HCOOH production
Re-Bpy-sp2c-COF	Olefin-linked		Catalytic active site	[19]	1040 $\mu\text{mol g}^{-1} \text{h}^{-1}$ CO production
Re-CTF-py	Triazine based		Enhanced electron-holes separation; enhanced charge transfer; catalytic active site	[160]	353.05 $\mu\text{mol g}^{-1} \text{h}^{-1}$ CO production
Re-TpBpy	$\beta$ -keto-enamine-linked		Catalytic active site	[155]	N/A
Ru-CTF	Triazine-based		Catalytic active site	[219]	2090 $\mu\text{mol g}^{-1} \text{h}^{-1}$ HCOO <sup>-</sup> production
ZnPor@Re	Conjugated-based, Porphyrin-based		Enhanced electron-holes separation; enhanced charge transfer; catalytic active site	[220]	66.2 $\text{mmol g}^{-1}$ CO production
Mn-TTA-COF	mine-linked, triazine-based		Enhanced electron-holes separation; Enhanced charge transfer	[172]	1.7 $\text{mmol g}^{-1}$ CO production
Mo-COF	$\beta$ -keto-enamine-linked		Enhanced electron-holes separation; enhanced CO <sub>2</sub> affinity	[156]	6.19 $\mu\text{mol g}^{-1} \text{h}^{-1}$ CO, 3.57 $\mu\text{mol g}^{-1} \text{h}^{-1}$ C <sub>2</sub> H <sub>4</sub> and 1.08 $\mu\text{mol g}^{-1} \text{h}^{-1}$ CH <sub>4</sub> production
Co@COFTVBT-Bpy	Imine-linked, triazine-based		Enhanced electron-holes separation; enhanced charge transfer; catalytic active site	[95]	1835 $\mu\text{mol g}^{-1} \text{h}^{-1}$ CO production
Ni-TpBpy	$\beta$ -keto-enamine-linked		Catalytic active site	[155]	N/A

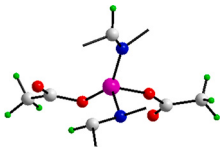
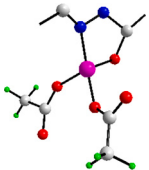
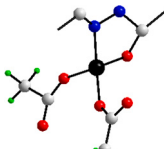
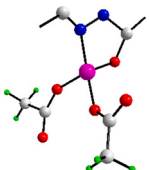
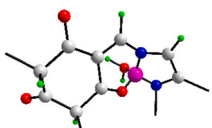
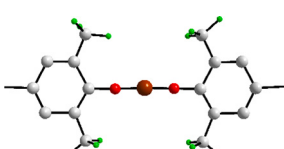
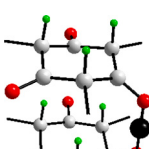
(continued on next page)

Table 3 (continued)

COF	Type	Coordination component	Functionality	Ref	Performance
Sp <sup>2</sup> c-COFdpy-Co	Olefin-linked		Enhanced charge transfer	[150]	1.00 mmol g <sup>-1</sup> h <sup>-1</sup> CO production
Co-TPTG <sub>Cl</sub>	β-keto-enamine-linked		Enhanced electron-holes separation; enhanced charge transfer; catalytic active site	[221]	14,641 μmol g <sup>-1</sup> h <sup>-1</sup> CO production
Cd-Bpy-COF Cu-Bpy-COF Zn-Bpy-COF Ni-Bpy-COF Co-Bpy-COF	Imine-linked, Triazine-based	 ● = Cd, Cu, Zn, Ni, and Co	Catalytic active site	[222]	17.5 μmol g <sup>-1</sup> h <sup>-1</sup> CO and 1.6 μmol g <sup>-1</sup> h <sup>-1</sup> CH <sub>4</sub> production * Cu-Bpy-COF
Fe SAS/Tr-COF	Imine-linked, Triazine-based		enhanced charge transfer	[103]	980.3 μmol g <sup>-1</sup> h <sup>-1</sup> CO production
COF-RuBpy-Co	Imine-linked, Porphyrin-based		Photosensitizer	[96]	547 μmol g <sup>-1</sup> h <sup>-1</sup> CO production
Cu-COF	Imine-linked, Triazine-based		Catalytic active site; enhanced light absorption	[173]	206 μmol g <sup>-1</sup> h <sup>-1</sup> CO production
Co@TpTta	β-keto-enamine-linked, Triazine-based		Catalytic active site	[181]	37.3 μmol h <sup>-1</sup> CO production
TFBD-COF-Co	Imine-linked		Catalytic active site; enhanced charge transfer	[106]	1804 μmol h <sup>-1</sup> CO production
TFBD-COF-Co-SA	Imine-linked		Catalytic active site; enhanced charge transfer	[106]	7400 μmol g <sup>-1</sup> h <sup>-1</sup> CO production

(continued on next page)

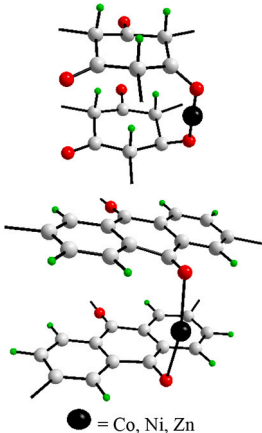
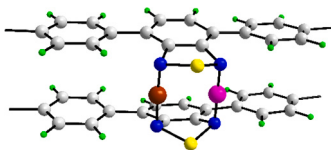
Table 3 (continued)

COF	Type	Coordination component	Functionality	Ref	Performance
I-COF-Ni	Imine-linked		Enhanced electron-holes separation; enhanced charge transfer	[176]	1960 $\mu\text{mol g}^{-1}$ CO production in 2 h
H-COF-Ni	N-acylhydrazone-linked		Enhanced electron-holes separation; enhanced charge transfer	[176]	2312 $\mu\text{mol g}^{-1} \text{h}^{-1}$ CO production
USTB-11(Cu, Ni)	N-acylhydrazone-linked	 ● = Cu or Ni	Enhanced electron-holes separation; catalytic active site	[149]	22,130 $\mu\text{mol g}^{-1} \text{h}^{-1}$ Co production
USTB-12(Ni)	N-acylhydrazone-linked		Enhanced electron-holes separation; catalytic active site	[149]	3120 $\mu\text{mol g}^{-1} \text{h}^{-1}$ CO production
Ni-TP-CON	$\beta$ -keto-enamine-linked		Enhanced selectivity of $\text{CO}_2$ towards $\text{N}_2$	[157]	4361 $\mu\text{mol g}^{-1} \text{h}^{-1}$ CO production
HB-TAPT+Co	Imine-linked, Triazine-based		Enhanced electron-holes separation; enhanced charge transfer	[175]	19.6 $\mu\text{mol g}^{-1} \text{h}^{-1}$ CO production
DATP COF-M	$\beta$ -keto-enamine-linked	 ● = Co, Ni, Zn	Enhanced electron-holes separation; catalytic active site	[98]	10.37 $\mu\text{mol g}^{-1} \text{h}^{-1}$ CO and 8.72 $\mu\text{mol g}^{-1} \text{h}^{-1}$ HCOOH production

(continued on next page)



Table 3 (continued)

COF	Type	Coordination component	Functionality	Ref	Performance
DQTP COF-M	$\beta$ -keto-enamine-linked		Enhanced electron-holes separation; catalytic active site	[98]	Co: 1200 $\mu\text{mol g}^{-1} \text{h}^{-1}$ CO; Zn: 152.5 $\mu\text{mol g}^{-1} \text{h}^{-1}$ HCOOH production
CoNi-COF-3	$\beta$ -keto-enamine-linked		Catalytic active site; enhanced charge transfer	[100]	2567 $\mu\text{mol g}^{-1} \text{h}^{-1}$ CO production

sites enabled by the linkage microenvironment [176]. The study revealed the crucial role of N-acylhydrazone linkage in stabilizing Ni ions in H-COF-Ni and creating the active species, Ni-bpy adduct, formed by adding bpy. The adduct was cooperatively stabilized by H-COF-Ni, resulting in higher photocatalytic activity for CO<sub>2</sub> reduction compared to the imine linkage in the imine-linked counterpart (I-COF-Ni).

Porosity and surface area are other critical factors to consider in the design of COFs for photocatalytic CO<sub>2</sub> reduction. A highly porous COF can provide more active sites for CO<sub>2</sub> adsorption and increase the gas diffusion rate, leading to higher CO<sub>2</sub> reduction efficiency. The surface area of COFs also plays a critical role in photocatalytic activity since it determines the number of active sites available for catalysis. A COF with a high surface area exhibited a higher CO<sub>2</sub> reduction rate than a COF with a low surface area due to increased active sites for catalysis. Previous studies have also demonstrated that combining COFs with other photocatalysts, such as g-C<sub>3</sub>N<sub>4</sub> [110], significantly enhances the photocatalytic activity for CO<sub>2</sub> reduction due to efficient electron-hole separation, facilitated separation of photogenerated electron-hole pairs, and the presence of additional redox centres.

By better understanding the factors that influence the photocatalytic activity of COFs, researchers can tailor the structure and composition of COFs to enhance their performance for CO<sub>2</sub> reduction. This can lead to the development of more efficient and sustainable methods for converting CO<sub>2</sub> into useful chemicals, essential for mitigating the effects of climate change and transitioning towards a more sustainable future. Fig. 25 presents an overview of the mechanism and factors influencing the photocatalytic reduction of CO<sub>2</sub> using COFs.

## 10. Comparison of COFs with other photocatalysts for CO<sub>2</sub> reduction

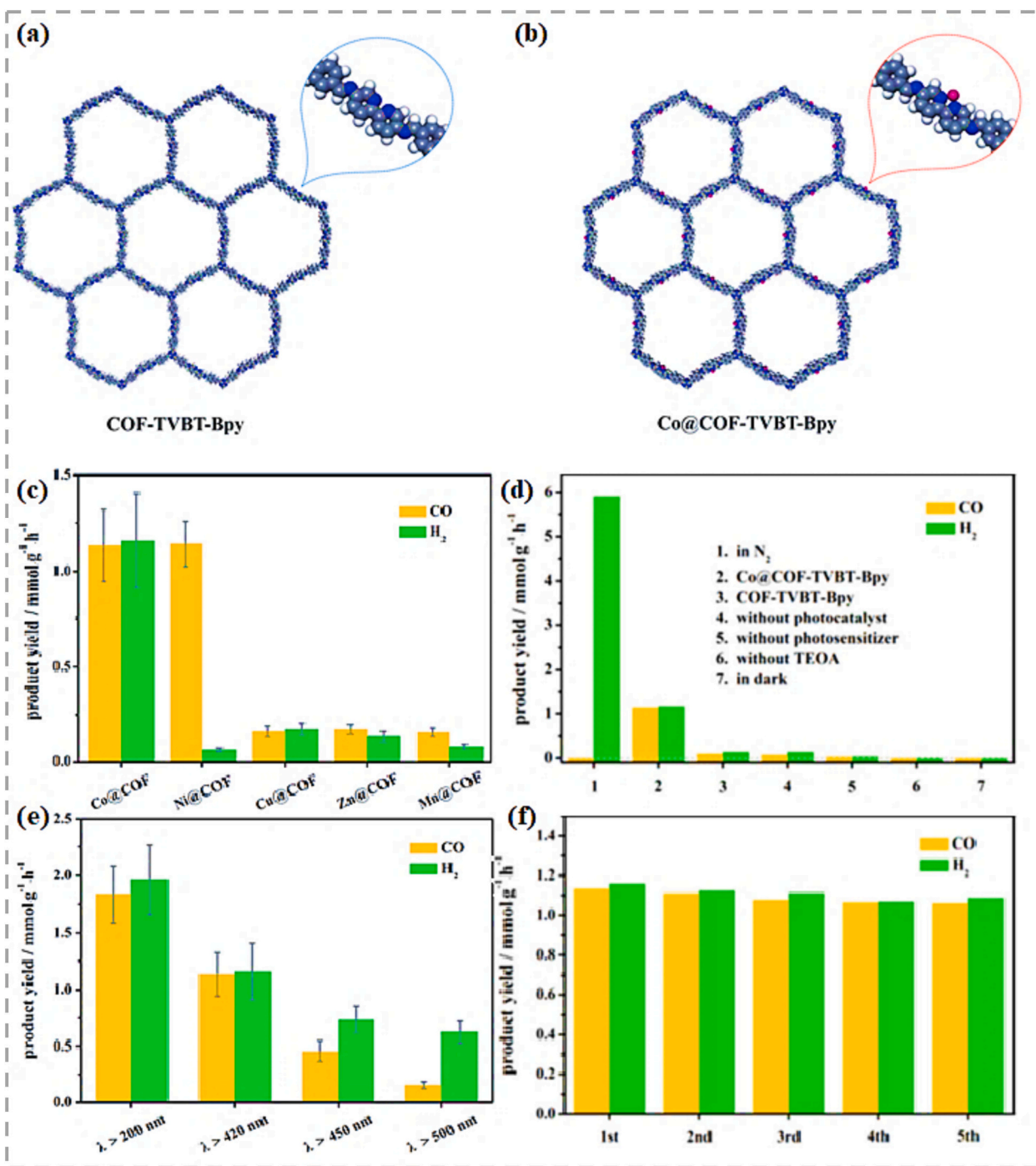
While COFs have shown tremendous promise as photocatalysts for CO<sub>2</sub> reduction, it is critical to comprehend the benefits of alternatives. Due to their potential for CO<sub>2</sub> reduction, alternative photocatalysts such as metal oxides, metal-organic frameworks (MOFs), and quantum dots have received much attention (Fig. 26). These materials offer distinct advantages that may improve the efficiency and selectivity of the

photocatalytic CO<sub>2</sub> reduction process. Hence, it is essential to evaluate the advantages of these alternative photocatalysts over COFs, as well as any potential limitations associated with their use.

Among these, metal oxides, such as TiO<sub>2</sub>, WO<sub>3</sub>, ZnO, Cu<sub>2</sub>O, and CeO<sub>2</sub>, offer substantial advantages as CO<sub>2</sub> reduction photocatalysts. These materials presented exceptional performance in driving the CO<sub>2</sub> conversion process, rendering them ideal for this application [231]. Furthermore, metal oxides are inexpensive, long-lasting, and efficient, making them economically viable for large-scale implementation [232]. Nevertheless, there are some limitations associated with its use. One such constraint is the occurrence of photo-corrosion, which can result in the oxidation or reduction of semiconductors or active metal centres, leading to reduced photocatalytic activity [233]. Another example includes the insufficiently negative electron flat-band potential of TiO<sub>2</sub> to reduce CO<sub>2</sub>, thereby impeding the CO<sub>2</sub> conversion efficiency effectively [234].

MOFs and COFs share similarities as porous materials with tuneable structures and properties. The key distinction, however, is the presence of metal in MOFs that provides prospective benefits for photocatalytic CO<sub>2</sub> reduction. Incorporating judiciously selected metals during MOF synthesis permits light absorption properties and active reduction sites, resulting in improved photocatalytic performance [235]. Nonetheless, the presence of metals imposes some constraints. For instance, the dative bond in MOFs is weaker than covalent bonds, which can affect the material's overall stability [236].

Compared to COFs, quantum dots (QDs) offer numerous benefits in photocatalytic CO<sub>2</sub> reduction. For instance, QDs exhibit remarkable turnover numbers, as exemplified by a reported CuInS<sub>2</sub> QD system with a turnover number over 80,000 for CO<sub>2</sub> reduction to CO [237]. The above implied their outstanding catalytic effectiveness and capability for significant CO<sub>2</sub> conversion. Secondly, excellent light absorption across a wide spectrum of wavelengths is a property of QDs that renders it possible for them to harness more solar energy during the photocatalytic process [238]. Compared to COFs, their greater photocatalytic activity results from their greater light absorption. In addition, the tunability of QDs enables precise control over their size and composition, enabling the optimisation of their photocatalytic characteristics for



**Fig. 24.** Chemical structures of (a) COF-TVBT-Bpy and (b) Co@COF-TVBT-Bpy. (c) Photocatalytic performances of M@COF-TVBT-Bpy (M = Co/Ni/Cu/Zn/Mn). (d) Photocatalytic CO<sub>2</sub> reduction under various reaction conditions. (e) Effect of incident light wavelength on the photocatalytic performance of Co@COF-TVBT-Bpy and (f) Reusability test of Co@COF-TVBT-Bpy in photocatalytic reaction. Reproduced through Copyright © permission.

particular applications [239,240]. Nevertheless, it is crucial to identify the limitations of QDs. The potential toxicity of QDs containing heavy metals like cadmium or lead is one of the major issues [241,242]. Due to the possible risks to the environment and human health associated with these metals, it is imperative to handle QD-based photocatalysts carefully. Additionally, QDs are susceptible to stability issues, including oxidation and degradation, which can significantly diminish their photocatalytic activity over time [243]. The stability issues must be overcome to ensure the long-term performance and practical applicability of QD-based photocatalytic materials.

On the other hand, COFs offer several beneficial properties over the

mentioned materials. For instance, COFs feature well-defined porous structures, similar to MOFs, that facilitate the efficient trapping of CO<sub>2</sub>. Moreover, the porosity of COFs can be carefully tuned to accommodate more CO<sub>2</sub>. Meanwhile, COFs demonstrate noteworthy stability and resistance to light-induced degradation due to their covalent bonding framework, which enables their use in a wide range of light-driven applications, including photocatalysis and solar energy conversion. Unlike QDs, COFs pose minimal environmental impact because they are non-toxic materials. However, there are some drawbacks to using COFs, such as having a relatively lower capacity for light absorption than the materials previously discussed, which may reduce

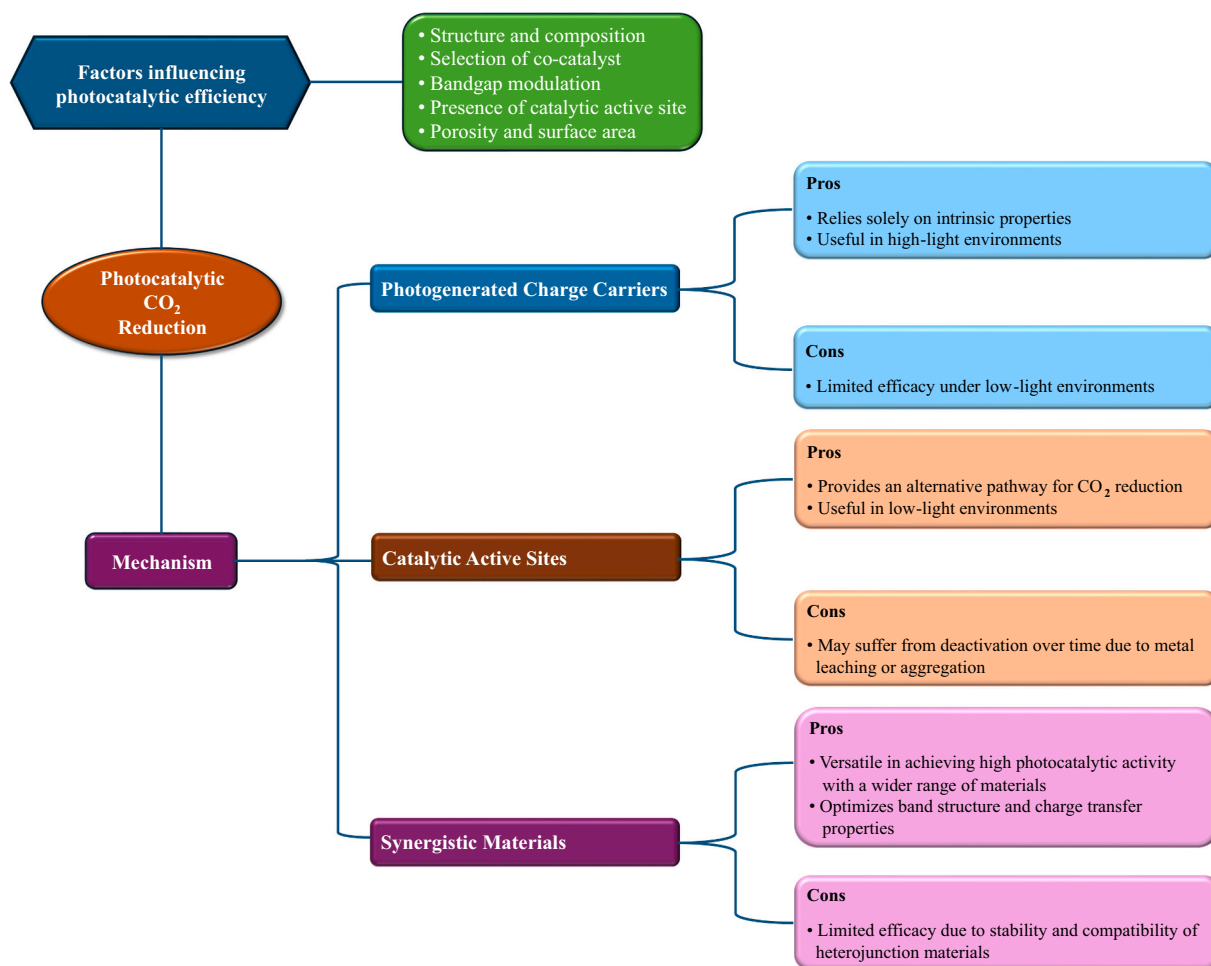


Fig. 25. Overview of the mechanism(s) and factors influencing the photocatalytic reduction of CO<sub>2</sub> using COFs.

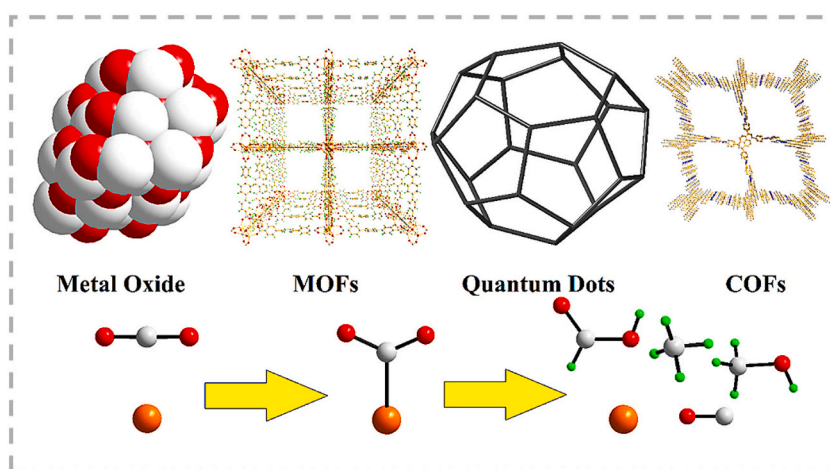


Fig. 26. Selected materials for photocatalytic CO<sub>2</sub> reduction.

their photocatalytic effectiveness. To overcome this limitation, the incorporation of a photosensitizer is often employed.

The synergistic effect of combining COFs and other photocatalytic materials holds significant promise. This approach enables the development of photocatalytic systems that are both highly effective and specifically engineered to address climate-related issues. By integrating COFs with complementing materials, limitations are eliminated, and new opportunities are made possible. For instance, combining

semiconductor materials like metal oxides or quantum dots with the high porosity and adjustable architectures of COFs for improved CO<sub>2</sub> capture, charge separation, and solar energy utilization. The integration of COFs with cocatalysts or photosensitizers may also optimize light absorption, electron transfer, and targeted chemical transformation. Synergistic strategies, therefore, offer opportunities for the design of hybrid systems that demonstrate robust stability, catalytic selectivity, and surface modification capabilities, thereby paving the door for long-

term CO<sub>2</sub> reduction and a low-carbon future.

## 11. Challenges and future directions

While COFs show great promise as photocatalysts for CO<sub>2</sub> conversion, several key challenges must be addressed to harness their potential fully. Foremost is improving the long-term photostability and structural integrity of COFs under the reactive conditions required for CO<sub>2</sub> reduction. Exposure to oxidative radicals, high temperatures, and other harsh reaction environments can degrade the covalent organic frameworks over time, limiting their reusability. Strategies to enhance stability, such as incorporating more robust linkages or protective coatings, are active areas of research. Optimizing CO<sub>2</sub> adsorption and activation on the COF surface is another critical hurdle. Many COFs exhibit hydrophobicity or lack sufficient interaction sites, resulting in poor affinity for CO<sub>2</sub> molecules. Tailoring the pore structure, functionality, and surface chemistry can improve CO<sub>2</sub> capture and subsequent activation for conversion. Integrating appropriate cocatalysts or catalyst supports with COFs may also facilitate this process.

Scaling up COF synthesis for large-scale photocatalytic applications remains a significant challenge. The complex, multi-step synthesis techniques used to produce high-quality COFs in the lab are difficult to translate to consistent, cost-effective manufacturing. Developing scalable fabrication methods is necessary to move COF photocatalysts from the research stage to real-world implementation. Additionally, expanding the light absorption capabilities of COFs beyond the current UV–visible range is important to maximize utilization of the solar spectrum. Incorporating light-harvesting chromophores or forming heterostructures with other light-absorbing materials could enhance broadband light harvesting. Improving charge carrier separation and transport within COF frameworks is another area requiring further research to boost overall photocatalytic performance.

Overcoming these challenges will require continued interdisciplinary collaboration among materials scientists, chemists, engineers, and catalysis experts. Innovative solutions combining tailored COF design, advanced characterization, and reactor engineering will pave the way for transformative photocatalytic CO<sub>2</sub> conversion technologies. With sustained progress, COFs hold great promise to play a pivotal role in developing sustainable approaches to climate change mitigation and renewable chemical production.

### 11.1. Future research direction on COFs for photocatalytic CO<sub>2</sub> reduction

Future research areas in COFs for photocatalytic CO<sub>2</sub> reduction include the integration of functional moieties into COFs. The potential of this approach is detailed in the following section.

#### 11.1.1. Functional moieties for improved catalytic activity

Incorporating functional moieties into COFs can significantly improve their catalytic performance for CO<sub>2</sub> reduction. Functional groups, such as amines, carboxylates, or metal centers, serve as active sites for the adsorption, activation, and conversion of CO<sub>2</sub>. Their presence enhances selectivity, reaction kinetics, and overall efficiency of the reduction process. Future research should focus on exploring various functional groups and optimizing their spatial arrangement within the COF structure to maximize catalytic activity. Functional moieties can be integrated into the COF framework to form covalent bonds or create active sites, thereby facilitating enhanced charge transfer and efficient coupling of intermediate species during CO<sub>2</sub> reduction. Investigating the precise placement and density of these moieties is crucial for optimizing catalytic performance and improving photocatalytic efficiency. Moreover, the introduction of certain functional groups can alter the redox properties of COFs, which is essential for efficient electron transport in photocatalysis. Incorporating redox-active molecules, such as metal complexes or organic chromophores, can optimize redox potentials and electron transfer pathways, thereby boosting photocatalytic CO<sub>2</sub>

reduction. Additionally, functional moieties can modify the surface characteristics of COFs to improve CO<sub>2</sub> adsorption capacity. By adding groups with a high affinity for CO<sub>2</sub>, researchers can enhance the accessibility of CO<sub>2</sub> molecules to active sites within the COF structure, leading to improved photocatalytic performance. Functional groups can also be covalently bonded to the COF framework, creating active sites that facilitate efficient charge transfer and intermediate species coupling. Future studies should aim to fine-tune the placement and density of functional moieties to optimize photocatalytic CO<sub>2</sub> reduction. Furthermore, incorporating diverse functional moieties may enable sequential and multi-step catalytic processes, allowing COFs to progressively reduce CO<sub>2</sub> to value-added products. Developing multifunctional COFs capable of performing multiple catalytic processes simultaneously is a promising research direction for enhancing the efficiency and selectivity of photocatalytic CO<sub>2</sub> reduction. Overall, integrating functional moieties into COFs represents a promising strategy for advancing photocatalytic CO<sub>2</sub> reduction, potentially leading to the development of highly efficient COF-based photocatalysts essential for effective CO<sub>2</sub> conversion and climate change mitigation.

#### 11.1.2. Designing COFs with tailored properties

Developing COFs with tailored properties through rational design and synthesis will be critical for future advancements in their application as photocatalysts for CO<sub>2</sub> reduction. Targeted efforts to engineer COFs with precise pore sizes, surface chemistries, and light absorption characteristics have the potential to significantly improve their photocatalytic efficiency. For instance, incorporating photo-responsive chromophores or widening absorption spectra could enhance light harvesting. In addition, modifying framework structures to increase charge carrier mobility and conductivity may enable more efficient charge separation and transport. A key research focus will be the targeted development of COFs with structural properties optimized specifically for photocatalytic CO<sub>2</sub> transformation. This involves experimenting with variable building blocks, linkers, and synthetic protocols to synthesize COFs featuring customized pore networks, surface areas, crystal structures, and accessible active sites.

Another important consideration is fine-tuning the band structure through rational functionalization to promote effective photoexcited charge transfer during CO<sub>2</sub> conversion. This can be achieved by incorporating functional groups or chromophores that modulate energy levels within the COF framework, thus expanding the spectrum of light absorption and improving CO<sub>2</sub> conversion efficiency and solar energy utilization. Similarly, improving the stability and durability of COFs under photocatalytic conditions is critical for their practical application. Future research should focus on strategies to enhance COF stability, such as investigating novel linkages or incorporating functional groups that promote robustness. Additionally, methods to minimize degradation and maintain catalytic activity over extended operation periods will be essential for realizing the long-term application of COFs in photocatalytic CO<sub>2</sub> reduction.

Furthermore, the development of advanced characterization techniques will also be critical in understanding the structure-function relationships in COFs for photocatalytic CO<sub>2</sub> reduction. Employing methods like *in situ* spectroscopy, time-resolved spectroscopy, and advanced microscopy will provide valuable insights into the photocatalytic mechanisms, charge dynamics, and surface properties of COFs. These techniques are crucial for optimizing COF properties and designing more efficient photocatalysts.

#### 11.1.3. Developing new synthetic approaches for COFs

Computational modelling and data-driven methodologies will play an increasingly important role in advancing new synthetic strategies for COFs. Future research should leverage computational techniques to inform the design of innovative building blocks, predict COF structures, optimize synthesis conditions, and investigate structure-property relationships. Additionally, data-driven approaches, including machine

learning and high-throughput screening, offer the potential to significantly expedite the discovery of new COFs with enhanced photocatalytic CO<sub>2</sub> reduction capabilities.

Post-synthetic alterations are a flexible method for adding functionality and improving the features of COFs. Future studies should concentrate on creating novel post-synthetic modification approaches to improve COF features important to photocatalytic CO<sub>2</sub> reduction. Surface functionalization, doping, and guest molecule inclusion are examples of such techniques. These alterations can add active sites, improve CO<sub>2</sub> adsorption, or improve charge transfer characteristics, all of which improve COF photocatalytic activity. Moreover, green and scalable synthesis techniques for COFs are an important future focus. Conventional COF synthesis often relies on harsh reaction conditions and toxic solvents. Future investigations should prioritize the development of more environmentally friendly and sustainable approaches, including solvent-free or solvent-reduced processes, microwave-assisted synthesis, and the use of non-toxic solvents. Efforts should also be directed toward establishing scalable synthesis techniques that can produce COFs in large quantities, which would significantly enhance their practical application in photocatalytic CO<sub>2</sub> reduction.

Furthermore, advancing COF synthesis will require the exploration of novel building blocks and linkers. This involves the design and synthesis of new organic compounds that can serve as building blocks for COF assembly. By introducing diverse and functionalized building blocks, researchers can expand the structural diversity and properties of COFs, enabling precise tuning of their photocatalytic activity for CO<sub>2</sub> reduction. Similarly, the development of new linkers with varying sizes, geometries, and functionalities will facilitate the creation of COFs with unique architectures and enhanced features.

Controlling the growth and crystallinity of COFs is also essential for optimizing their photocatalytic performance. Future research should focus on developing innovative synthetic methodologies, such as template-directed or seed-mediated approaches, that offer precise control over the growth process. These methods hold promise for producing well-defined and highly crystalline COF structures with superior photocatalytic activity. Furthermore, advances in understanding COF nucleation and growth mechanisms will enable the design of synthetic strategies that yield COFs with specific sizes, shapes, and orientations, further enhancing their practical applicability in environmental and energy-related fields.

## 12. Potential impact of COFs on sustainable solutions for mitigating climate change

COFs hold significant promise for contributing to long-term climate change mitigation strategies. Their potential impact on addressing this global challenge can be explored through several key applications:

One of the most promising uses of COFs is as CO<sub>2</sub> reduction photocatalysts. COFs can transform CO<sub>2</sub> into useful chemicals or fuels by capturing solar energy, lowering greenhouse gas emissions, and increasing the use of CO<sub>2</sub> as a resource. This technique provides a sustainable and renewable alternative to typical energy-intensive procedures and feedstocks derived from fossil fuels. COFs can be used for CCS, an important technique for reducing CO<sub>2</sub> emissions from industrial activities. COFs with large surface areas and customized adsorption characteristics can absorb CO<sub>2</sub> selectively from flue gas streams or other emission sources. The gathered CO<sub>2</sub> may subsequently be stored underground or converted into useful goods, reducing its environmental influence. In addition, COFs can also be used to power energy storage and conversion devices. The unique porous architectures and customizable features of COF can improve energy storage capacity, charge/discharge rates, and cycle stability when integrated into energy storage devices such as batteries or supercapacitors. COFs can also be used in energy conversion devices such as fuel cells or solar cells to improve energy conversion and utilization.

Beyond energy and emissions technologies, COFs can also help with

long-term water treatment and purification solutions. Because of their porous architecture and affinity for certain contaminants, they are excellent for applications such as water filtration, desalination, and pollutant and heavy metal removal. COFs can be used as adsorbents, catalytic supports, or membrane materials, providing novel and sustainable alternatives to clean water generation. Additionally, their large surface areas, well-defined architectures, and tunable functionalities make COFs excellent candidates for catalytic applications. They can serve as catalysts or catalyst supports in environmentally friendly and energy-efficient chemical reactions, leading to reduced energy consumption, waste production, and environmental impact.

COFs also exhibit unique structural and chemical characteristics make them ideal candidates for constructing sensors for detecting greenhouse gases. They can be functionalized to interact with gases such as CO<sub>2</sub>, methane (CH<sub>4</sub>), or nitrous oxide (N<sub>2</sub>O). Incorporating COFs into sensor devices makes monitoring and measuring greenhouse gas emissions feasible, allowing for targeted mitigation techniques and emissions reduction initiatives. Leveraging the capabilities of COFs could contribute to a more sustainable, low-carbon future, addressing climate change and reducing dependence on non-renewable resources.

## 13. Conclusion

The review provides valuable insights into the promising yet still developing application of COFs for photocatalytic CO<sub>2</sub> reduction. COFs display desirable characteristics including high porosity, structural tunability and stability. However, major technological challenges surrounding photocatalyst robustness, efficient CO<sub>2</sub> uptake and activation, reactor design at scale, and scalable synthesis must still be addressed. Researchers have explored strategies to enhance COF resilience, surface properties for CO<sub>2</sub> adsorption, and mass transfer via reactor optimization. Efforts have also focused on developing scalable synthesis and boosting CO<sub>2</sub> binding affinity. Post-synthetic functionalization offers a way to optimize COF structure-function relationships and photocatalytic activity. While COFs demonstrate prospective solutions for curbing greenhouse gas emissions by solar-driven CO<sub>2</sub> transformations, further cross-disciplinary advancements are needed to resolve stability, reaction kinetics, process integration and scalability issues. Structural engineering approaches may also help to gain photophysical properties critical for CO<sub>2</sub> photoreduction. With continued progress in COF design and interdisciplinary collaborations, these promising materials could potentially enable practical, solar-powered CO<sub>2</sub> recycling in the future.

### CRedit authorship contribution statement

**Conceptualization:** Mohammad Khalid, Rashmi Walvekar; **Methodology, Supervision, Project administration:** Bey Hing Goh, Mohammad Khalid; **Data collection:** Chien Ing Yeo, Yee Seng Tan, Hafiz Taimoor Ahmed Awan; **Funding:** Mohammad Khalid; **Resources:** Bey Hing Goh, Mohammad Khalid; **Writing—original draft preparation:** Chien Ing Yeo, Yee Seng Tan, Hafiz Taimoor Ahmed Awan, Abdul Hanan, Weng Pin Wong; **Writing—review and editing:** Rashmi Walvekar, Bey Hing Goh, Mohammad Khalid; **Analysis:** Abdul Hanan, Weng Pin Wong.

### Declaration of competing interest

The authors declare that they have no known competing financial interests or personal relationships that could have appeared to influence the work reported in this paper.

### Data availability

Data will be made available on request.

## Acknowledgements

The authors express their gratitude to the University of Glasgow, UK and Sunway University, Malaysia, for their invaluable support and the provision of resources that made this research possible.

## References

- [1] P. Prabhu, V. Jose, J.-M. Lee, 30 (2020) 1910768.
- [2] R.R. Raja Sulaiman, A. Hanan, W.Y. Wong, R. Mohamad Yunus, K. Shyuan Loh, R. Walvekar, V. Chaudhary, M.J.C. Khalid, 12 (2022) 1576.
- [3] A. Paiano, G. Lagioia, C. Ingraio, *Sci. Total Environ.* 866 (2023) 161329.
- [4] W.P. Wong, R. Walvekar, M. Vaka, M. Khalid, N.M. Mubarak, *ECS J. Solid State Sci. Technol.* 12 (2023) 031012.
- [5] G. Yin, M. Nishikawa, Y. Nosaka, N. Srinivasan, D. Atarashi, E. Sakai, M. Miyachi, *ACS Nano* 9 (2015) 2111–2119.
- [6] A. Hussain, M.N. Lakhani, A. Hanan, I.A. Soomro, M. Ahmed, F. Bibi, I. Zehra, *Mat. Today Sustain.* 23 (2023) 100420.
- [7] A.D. Tjandra, J. Huang, *Chin. Chem. Lett.* 29 (2018) 734–746.
- [8] M.Y. Solangi, U. Aftab, A. Tahira, A. Hanan, M. Montecchi, L. Pasquali, M. Tonzzer, R. Mazzaro, V. Morandi, A.J. Laghari, A. Nafady, M.I. Abro, M. Emo, B. Vigolo, E. Dawi, E. Mustafa, Z.H. Ibupoto, *Int. J. Hydrog. Energy* 48 (2023) 36439–36451.
- [9] A. Hanan, D. Shu, U. Aftab, D. Cao, A.J. Laghari, M.Y. Solangi, M.I. Abro, A. Nafady, B. Vigolo, A.J.L.J.O.H.E. Tahira, 47 (2022) 33919–33937.
- [10] A.J. Laghari, U. Aftab, A. Tahira, A.A. Shah, A. Gradone, M.Y. Solangi, A.H. Samo, M. Kumar, M.I. Abro, M.W. Akhtar, R. Mazzaro, V. Morandi, A.M. Alotaibi, A. Nafady, A. Infantes-Molina, Z.H. Ibupoto, *Int. J. Hydrog. Energy* 48 (2023) 12672–12682.
- [11] Q. Huang, R. Wang, X. Li, T. Liu, A.R.M. Shaheer, R. Cao, *Chin. Chem. Lett.* 34 (2023) 108517.
- [12] M. Bellardita, V. Loddò, F. Parrino, L. Palmisano, 5 (2021) 767–791.
- [13] S. Balu, A. Hanan, H. Venkatesvaran, S.-W. Chen, T.C.K. Yang, M. Khalid, *Catalysts* 13 (2023) 393.
- [14] H. Yang, J. Xu, H. Cao, J. Wu, D. Zhao, *Nat. Commun.* 14 (2023) 2726.
- [15] M.B. Chambers, X. Wang, N. Elgrishi, C.H. Hendon, A. Walsh, J. Bonnefoy, J. Canivet, E.A. Quadrelli, D. Farrusseng, C. Mellot-Draznieks, M. Fontecave, 8 (2015) 603–608.
- [16] Y.-Z. Cheng, X. Ding, B.-H. Han, 5 (2021) 406–417.
- [17] M. Khan, Z. Akmal, M. Tayyab, S. Mansoor, A. Zeb, Z. Ye, J. Zhang, S. Wu, L. Wang, *Carbon Capture Science & Technology* 11 (2024) 100191.
- [18] A. Hanan, M.N. Lakhani, F. Bibi, A. Khan, I.A. Soomro, A. Hussain, U. Aftab, *Chem. Eng. J.* 482 (2024) 148776.
- [19] Z. Fu, X. Wang, A.M. Gardner, X. Wang, S.Y. Chong, G. Neri, A.J. Cowan, L. Liu, X. Li, A. Vogel, R. Clowes, M. Bilton, L. Chen, R.S. Sprick, A.I. Cooper, *Chem. Sci.* 11 (2020) 543–550.
- [20] S.Q. You, J. Zhou, M.M. Chen, C.Y. Sun, X.J. Qi, A. Yousaf, X.L. Wang, Z.M. Su, *J. Catal.* 392 (2020) 49–55.
- [21] S. Sarkar, S. Ghosh, S.M. Islam, *Org. Biomol. Chem.* 20 (2022) 1707–1722.
- [22] P. Sarkar, I.H. Chowdhury, S. Das, S.M. Islam, *Mat. Adv.* 3 (2022) 8063–8080.
- [23] K. Geng, T. He, R. Liu, S. Dalapati, K.T. Tan, Z. Li, S. Tao, Y. Gong, Q. Jiang, D. Jiang, *Chem. Rev.* 120 (2020) 8814–8933.
- [24] H.R. Abuzeid, A.F.M. El-Mahdy, W. Kuo, *Giant* 6 (2021) 100054.
- [25] A.P. Côté, A.I. Benin, N.W. Ockwing, M. O’Keefe, A.J. Matzger, O.M. Yaghi, *Science (New York, N.Y.)* vol. 310, 2005, pp. 1166–1170.
- [26] Z. Meng, K.A. Mirica, *Chem. Soc. Rev.* 50 (2021) 13498–13558.
- [27] C.S. Diercks, O.M. Yaghi, *Science (New York, N.Y.)*, 355 (2017) eaal1585.
- [28] R. Liu, K.T. Tan, Y. Gong, Y. Chen, Z. Li, S. Xie, T. He, Z. Lu, H. Yang, D. Jiang, *Chem. Soc. Rev.* 50 (2021) 120–242.
- [29] N. Huang, P. Wang, D. Jiang, *Nat. Rev. Mater.* 1 (2016) 16068.
- [30] M.S. Lohse, T. Bein, *Adv. Funct. Mater.* 28 (2018) 1705553.
- [31] R.P. Bisbey, W.R. Dichtel, *ACS Cent. Sci.* 3 (2017) 533–543.
- [32] X. Chen, K. Geng, R. Liu, K.T. Tan, Y. Gong, Z. Li, S. Tao, Q. Jiang, D. Jiang, *Angew. Chem. Int. Ed.* 59 (2020) 5050–5091.
- [33] X. Wang, H. Liu, J. Zhang, S. Chen, *Polym. Chem.* 14 (2023) 1293–1317.
- [34] S.H. Goudar, D.S. Ingle, R. Sahu, S. Kotha, S.K. Reddy, D.J. Babu, V.R. Kotagiri, *ACS Appl. Polymer Mat.* 5 (2023) 2097–2104.
- [35] Z. Wang, X.-M. Li, H. Li, *CrystEngComm* 25 (2023) 1910–1914.
- [36] K. Asokan, M.K. Patil, S.P. Mukherjee, S.B. Sukumaran, T. Nandakumar, *Chem. – An Asian J.* 17 (2022) e202201012.
- [37] K.S. Song, P.W. Fritz, A. Coskun, *Chem. Soc. Rev.* 51 (2022) 9831–9852.
- [38] L.L.U. Hualin, L.I. Yanan, Z.I. Min, C. Zheng, D. Aihong, Y. Liming, *Chin. J. Chromatogr.* 41 (2023) 187–194.
- [39] E. Dautzenberg, G. Li, L.C.P.M. de Smet, *ACS Appl. Mater. Interfaces* 15 (2023) 5118–5127.
- [40] B. Chen, H. Xie, L. Shen, Y. Xu, M. Zhang, M. Zhou, B. Li, R. Li, H. Lin, *Small* 19 (2023) 2207313.
- [41] S. Zhou, Y. Kuang, Y. Shi, Y. Hu, L. Chen, J. Zheng, G. Ouyang, *Chem. Eng. J.* 453 (2023) 139743.
- [42] C.-X. Liu, Z.-W. Zhou, Y. Yu, Y.-J. Wei, C.-X. Cai, N. Wang, X.-Q. Yu, *Small Struct.* 4 (2023) 2200321.
- [43] X.-R. Deng, A.W. Hu, S.-Q. Hu, W.-L. Yang, C. Sun, S.-J. Xiao, G.-P. Yang, Q.-Q. Zheng, R.-P. Liang, L. Zhang, J.-D. Qiu, *Anal. Chim. Acta* 1252 (2023) 341056.
- [44] E. Nikkhoo, S. Mallakpour, C.M. Hussain, *New J. Chem.* 47 (2023) 6765–6788.
- [45] D. Ma, Y. Song, H. Zhao, C. Yu, Y. Zhang, C. Li, K. Liu, *ACS Sustain. Chem. Eng.* 11 (2023) 6183–6190.
- [46] Z. He, J. Goulas, E. Parker, Y. Sun, X.-D. Zhou, L. Fei, *Catal. Today* 409 (2023) 103–118.
- [47] J. Li, D. Zhao, J. Liu, A. Liu, D. Ma, *Molecules (Basel, Switzerland)*, 2020.
- [48] H. Shen, T. Peppel, J. Strunk, Z. Sun, *Sol. RRL* 4 (2020) 1900546.
- [49] J.L. Segura, M.J. Mancheño, F. Zamora, *Chem. Soc. Rev.* 45 (2016) 5635–5671.
- [50] F.C. Çavuşoğlu, G. Özçelik, Ş.S. Bayazit, Recent development in synthesis of covalent organic frameworks, in: *Covalent Organic Frameworks*, CRC Press, 2022, pp. 39–56.
- [51] J. Cheng, Y. Wu, W. Zhang, J. Zhang, L. Wang, M. Zhou, F. Fan, X. Wu, H. Xu, 36 (2024) 2305313.
- [52] S.B. Alahakoon, S.D. Diwakara, C.M. Thompson, R.A. Smaldone, *Chem. Soc. Rev.* 49 (2020) 1344–1356.
- [53] K. Dey, S. Mohata, R. Banerjee, *ACS Nano* 15 (2021) 12723–12740.
- [54] S. Bhunia, K.A. Deo, A.K. Gaharwar, *Adv. Funct. Mater.* 30 (2020) 2002046.
- [55] S. Xu, M. Richter, X. Feng, *Acc. Mat. Res.* 2 (2021) 252–265.
- [56] A.K. Mohammed, S. Usgaonkar, F. Kanheerampokil, S. Karak, A. Halder, M. Tharkar, M. Addicoat, T.G. Ajithkumar, R. Banerjee, *J. Am. Chem. Soc.* 142 (2020) 8252–8261.
- [57] X. Guan, F. Chen, Q. Fang, S. Qiu, *Chem. Soc. Rev.* 49 (2020) 1357–1384.
- [58] X. Li, P. Yadav, K.P. Loh, *Chem. Soc. Rev.* 49 (2020) 4835–4866.
- [59] S. Xue, X. Ma, Y. Wang, G. Duan, C. Zhang, K. Liu, S. Jiang, *Coord. Chem. Rev.* 504 (2024) 215659.
- [60] H. Li, L. Wang, G. Yu, *Nano Today* 40 (2021) 101247.
- [61] Y.-N. Gong, X. Guan, H.-L. Jiang, *Coord. Chem. Rev.* 475 (2023) 214889.
- [62] Q. Yang, M. Luo, K. Liu, H. Cao, H. Yan, *Appl. Catal. B Environ.* 276 (2020) 119174.
- [63] R.W. Tilford, S.J. Mugavero III, P.J. Pellechia, J.J. Lavigne, *Adv. Mater.* 20 (2008) 2741–2746.
- [64] J. Francis Kuringal, H. Kim, J. Hyeak Choe, C. Seop Hong, *Coord. Chem. Rev.* 473 (2022) 214835.
- [65] P.J. Waller, F. Gándara, O.M. Yaghi, *Acc. Chem. Res.* 48 (2015) 3053–3063.
- [66] Z. Wang, S. Zhang, Y. Chen, Z. Zhang, S. Ma, *Chem. Soc. Rev.* 49 (2020) 708–735.
- [67] S. Liu, M. Wang, Y. He, Q. Cheng, T. Qian, C. Yan, *Coord. Chem. Rev.* 475 (2023) 214882.
- [68] W.-T. Chung, I.M.A. Mekhemer, M.G. Mohamed, A.M. Elewa, A.F.M. El-Mahdy, H.-H. Chou, S.-W. Kuo, K.C.W. Wu, *Coord. Chem. Rev.* 483 (2023) 215066.
- [69] B. Dziejarski, J. Serafin, K. Andersson, R. Krzyżyńska, *Mat. Today Sustain.* 24 (2023) 100483.
- [70] X. Li, S. Cai, B. Sun, C. Yang, J. Zhang, Y. Liu, *Matter* 3 (2020) 1507–1540.
- [71] G. Tian, F. Guo, C. Fan, Z. Zong, J. Wang, J. Xu, *J. Solid State Chem.* 316 (2022) 123614.
- [72] H. Lyu, H. Li, N. Hanikel, K. Wang, O.M. Yaghi, *J. Am. Chem. Soc.* 144 (2022) 12989–12995.
- [73] F. Yuan, Z. Yang, X. Zhang, C. Tong, G. Gahungu, W. Li, J. Zhang, 42 (2021) 888–896.
- [74] Z. Kang, Y. Peng, Y. Qian, D. Yuan, M.A. Addicoat, T. Heine, Z. Hu, L. Tee, Z. Guo, D. Zhao, *Chem. Mater.* 28 (2016) 1277–1285.
- [75] S.B. Alahakoon, C.M. Thompson, A.X. Nguyen, G. Occhialini, G.T. McCandless, R. A. Smaldone, *Chem. Commun.* 52 (2016) 2843–2845.
- [76] J. Wang, L. Wang, Y. Wang, F. Yang, J. Li, X. Guan, J. Zong, F. Zhou, J. Huang, Y.-N. Li, *Chem. Eng. J.* 438 (2022) 135555.
- [77] R. Khatun, S. Biswas, I.H. Biswas, S. Riyajuddin, N. Haque, K. Ghosh, S.M. Islam, *J. CO2 Util.* 40 (2020) 101180.
- [78] H. Lyu, O.I.-F. Chen, N. Hanikel, M.I. Hossain, R.W. Flaig, X. Pei, A. Amin, M. D. Doherty, R.K. Impastato, T.G. Glover, D.R. Moore, O.M. Yaghi, *J. Am. Chem. Soc.* 144 (2022) 2387–2396.
- [79] R.A. Maia, F. Lopes Oliveira, V. Ritleng, Q. Wang, B. Louis, P. Mothé, *Estes* 27 (2021) 8048–8055.
- [80] Y. Ding, Y. Wang, Y. Su, Z. Yang, J. Liu, X. Hua, H. Wei, *Chin. Chem. Lett.* 31 (2020) 193–196.
- [81] A. Sharma, A. Malani, N.V. Medhekar, R. Babarao, *CrystEngComm* 19 (2017) 6950–6963.
- [82] S. An, T. Xu, C. Peng, J. Hu, H. Liu, *RSC Adv.* 9 (2019) 21438–21443.
- [83] W. Liu, Q. Su, P. Ju, B. Guo, H. Zhou, G. Li, Q. Wu, 10 (2017) 664–669.
- [84] Y. Zhi, Z. Li, X. Feng, H. Xia, Y. Zhang, Z. Shi, Y. Mu, X. Liu, *J. Mater. Chem. A* 5 (2017) 22933–22938.
- [85] P.-F. Wei, M.-Z. Qi, Z.-P. Wang, S.-Y. Ding, W. Yu, Q. Liu, L.-K. Wang, H.-Z. Wang, W.-K. An, W. Wang, *J. Am. Chem. Soc.* 140 (2018) 4623–4631.
- [86] X. Yan, H. Liu, Y. Li, W. Chen, T. Zhang, Z. Zhao, G. Xing, L. Chen, *Macromolecules* 52 (2019) 7977–7983.
- [87] E. Jin, Z. Lan, Q. Jiang, K. Geng, G. Li, X. Wang, D. Jiang, *Chem* 5 (2019) 1632–1647.
- [88] S. Bi, C. Yang, W. Zhang, J. Xu, L. Liu, D. Wu, X. Wang, Y. Han, Q. Liang, F. Zhang, *Nat. Commun.* 10 (2019) 2467.
- [89] W. Qiu, Y. He, L. Li, Z. Liu, S. Zhong, Y. Yu, *Langmuir* 37 (2021) 11535–11543.
- [90] R.K. Yadav, A. Kumar, N.-J. Park, K.-J. Kong, J.-O. Baeg, *J. Mater. Chem. A* 4 (2016) 9413–9418.
- [91] Y. Fu, X. Zhu, L. Huang, X. Zhang, F. Zhang, W. Zhu, *Appl. Catal. B Environ.* 239 (2018) 46–51.
- [92] H.-Y. Yu, J.-S. Wang, F.-Y. Xie, Q. Yang, Y. Chen, L. Zhao, Y. Li, W.-J. Ruan, *Chem. Eng. J.* 445 (2022) 136713.
- [93] J.-X. Cui, L.-J. Wang, L. Feng, B. Meng, Z.-Y. Zhou, Z.-M. Su, K. Wang, S. Liu, *J. Mater. Chem. A* 9 (2021) 24895–24902.

- [194] X. Yu, K. Gong, S. Tian, G. Gao, J. Xie, X.-H. Jin, *J. Mater. Chem. A* 11 (2023) 5627–5635.
- [195] J.-X. Cui, Y.-M. Fu, B. Meng, J. Zhou, Z.-Y. Zhou, S.-M. Liu, Z.-M. Su, *J. Mater. Chem. A* 10 (2022) 13418–13427.
- [196] L.-J. Gong, L.-Y. Liu, S.-S. Zhao, S.-L. Yang, D.-H. Si, Q.-J. Wu, Q. Wu, Y.-B. Huang, *R. Cao, Chem. Eng. J.* 458 (2023) 141360.
- [197] M. Dong, J. Zhou, J. Zhong, H.-T. Li, C.-Y. Sun, Y.-D. Han, J.-N. Kou, Z.-H. Kang, X.-L. Wang, Z.-M. Su, *Adv. Funct. Mater.* 32 (2022) 2110136.
- [198] M. Lu, Q. Li, J. Liu, F.-M. Zhang, L. Zhang, J.-L. Wang, Z.-H. Kang, Y.-Q. Lan, *Appl. Catal. B Environ.* 254 (2019) 624–633.
- [199] T. Skorjanc, D. Shetty, M.E. Mahmoud, F. Gándara, J.I. Martínez, A. K. Mohammed, S. Boutros, A. Merhi, E.O. Shehaye, C.A. Sharabati, P. Damacet, J. Raya, S. Gardonio, M. Hmadeh, B.R. Kaafarani, A. Trabolzi, *ACS Appl. Mater. Interfaces* 14 (2022) 2015–2022.
- [100] J. Wang, W. Zhu, F. Meng, G. Bai, Q. Zhang, X. Lan, *ACS Catal.* 13 (2023) 4316–4329.
- [101] M. Zhou, Z. Wang, A. Mei, Z. Yang, W. Chen, S. Ou, S. Wang, K. Chen, P. Reiss, K. Qi, J. Ma, Y. Liu, *Nat. Commun.* 14 (2023) 2473.
- [102] W. Zhong, R. Sa, L. Li, Y. He, L. Li, J. Bi, Z. Zhuang, Y. Yu, Z. Zou, *J. Am. Chem. Soc.* 141 (2019) 7615–7621.
- [103] L. Ran, Z. Li, B. Ran, J. Cao, Y. Zhao, T. Shao, Y. Song, M.K.H. Leung, L. Sun, J. Hou, *J. Am. Chem. Soc.* 144 (2022) 17097–17109.
- [104] W. Liu, X. Li, C. Wang, H. Pan, W. Liu, K. Wang, Q. Zeng, R. Wang, J. Jiang, *J. Am. Chem. Soc.* 141 (2019) 17431–17440.
- [105] J. Bi, B. Xu, L. Sun, H. Huang, S. Fang, L. Li, L. Wu, *ChemPlusChem* 84 (2019) 1149–1154.
- [106] Y. Yang, Y. Lu, H.-Y. Zhang, Y. Wang, H.-L. Tang, X.-J. Sun, G. Zhang, F.-M. Zhang, *ACS Sustain. Chem. Eng.* 9 (2021) 13376–13384.
- [107] X. Chen, Q. Dang, R. Sa, L. Li, L. Li, J. Bi, Z. Zhang, J. Long, Y. Yu, Z. Zou, *Chem. Sci.* 11 (2020) 6915–6922.
- [108] X. Song, Y. Wu, X. Zhang, X. Li, Z. Zhu, C. Ma, Y. Yan, P. Huo, G. Yang, *Chem. Eng. J.* 408 (2021) 127292.
- [109] R. Yang, Q. Chen, G. Huang, J. Bi, *Environ. Res.* 216 (2023) 114541.
- [110] J. Wang, Y. Yu, J. Cui, X. Li, Y. Zhang, C. Wang, X. Yu, J. Ye, *Appl. Catal. B Environ.* 301 (2022) 120814.
- [111] Z. Zhang, Y. Jiang, Z. Dong, Y. Chu, J. Xu, *Inorg. Chem.* 61 (2022) 16028–16037.
- [112] Q. Niu, S. Dong, J. Tian, G. Huang, J. Bi, L. Wu, *ACS Appl. Mater. Interfaces* 14 (2022) 24299–24308.
- [113] X. An, J. Bian, K. Zhu, R. Liu, H. Liu, J. Qu, *Chem. Eng. J.* 442 (2022) 135279.
- [114] Y. Wu, J. Liu, J. Rong, Y. Zhang, Q. Liang, M. Zhou, Z. Li, S. Xu, *Appl. Surf. Sci.* 620 (2023) 156781.
- [115] V.N. Gopalakrishnan, D.-T. Nguyen, J. Becerra, M. Sakar, J.M.E. Ahad, J. J. Jautzy, L.M. Mindorff, F. Bédard, T.-O. Do, *ACS Appl. Energy Mat.* 4 (2021) 6005–6014.
- [116] W. Zheng, J. Hou, C. Liu, P. Liu, L. Li, L. Chen, *Z. Tang*, 16 (2021) 3624–3629.
- [117] O. Ola, M.M. Maroto-Valer, *J. Photochem. Photobiol. C Photochem. Rev.* 24 (2015) 16–42.
- [118] Y. Zhu, J. Zhou, J. Hu, H. Liu, Y. Hu, *Chin. J. Chem. Eng.* 19 (2011) 709–716.
- [119] C. Kang, Z. Zhang, S. Xi, H. Li, A.K. Usadi, D.C. Calabro, L.S. Baugh, Y. Wang, D. Zhao, *Proc. Natl. Acad. Sci. USA* 120 (2023) e2217081120.
- [120] W. Chen, L. Huang, X.F. Yi, A.M. Zheng, *Phys. Chem. Chem. Phys.* 20 (2018) 6487–6499.
- [121] L. Stegbauer, M.W. Hahn, A. Jentys, G. Savasci, C. Ochsenfeld, J.A. Lercher, B. V. Lotsch, *Chem. Mater.* 27 (2015) 7874–7881.
- [122] A.G. Solangi, A. Tahira, A.S. Chang, T. Pirzada, Z.A. Solangi, F. Chang, M. A. Bhatti, A.L. Bhatti, S. Kumar, A. Hanan, E. Dawi, A.A.K.H. Ismail, S.S. Medany, A. Nafady, L.V. Kangle, B. Vigolo, Z.H. Ibutopo, *J. Mater. Sci. Mater. Electron.* 34 (2023) 1549.
- [123] M.Y. Solangi, U. Aftab, A. Tahira, A. Hanan, M. Montecchi, L. Pasquali, M. Tonezzer, R. Mazzaro, V. Morandi, A.J.J.I.O.H.E. Laghari, (2023).
- [124] Z. Liang, R. Shen, Y.H. Ng, Y. Fu, T. Ma, P. Zhang, Y. Li, X. Li, *Chem. Cat.* 2 (2022) 2157–2228.
- [125] S. Yang, W. Hu, X. Zhang, P. He, B. Pattengale, C. Liu, M. Cendejas, I. Hermans, X. Zhang, J. Zhang, J. Huang, *J. Am. Chem. Soc.* 140 (2018) 14614–14618.
- [126] V.N. Gopalakrishnan, J. Becerra, S. Mohan, J.M.E. Ahad, F. Bédard, T.O. Do, *Energy Fuel* 37 (2023) 2329–2339.
- [127] B. Petrovic, M. Gorbounov, S. Masoudi Soltani, *Microporous Mesoporous Mater.* 312 (2021) 110751.
- [128] N. Narayan, A. Meiyazhagan, R. Vajtai, *Materials* 12 (2019) 3602.
- [129] Y. Tauran, A. Brioude, A.W. Coleman, M. Rhimi, B. Kim, *World J. Biol. Chem.* 4 (2013) 35.
- [130] A. Álvarez, M. Borges, J.J. Corral-Pérez, J.G. Olcina, L. Hu, D. Cornu, R. Huang, D. Stoian, A. Urakawa, *Chem. Phys. Chem.* 18 (2017) 3135–3141.
- [131] S.M. Rogge, A. Bavykina, J. Hajek, H. Garcia, A.I. Olivios-Suarez, A. Sepúlveda-Escribano, A. Vimont, G. Clet, P. Bazin, F. Kapteijn, *Chem. Soc. Rev.* 46 (2017) 3134–3184.
- [132] S. Abednatanzi, M. Najafi, P.G. Derakhshandeh, P. Van Der Voort, *Coord. Chem. Rev.* 451 (2022) 214259.
- [133] E. Dautzenberg, F.W. Claassen, L.C.P.M. de Smet, *Microporous Mesoporous Mater.* 350 (2023) 112318.
- [134] S. Jin, O. Allam, S.S. Jang, S.W. Lee, 4 (2022) e12277.
- [135] X. Zhao, P. Pachfule, A. Thomas, *Chem. Soc. Rev.* 50 (2021) 6871–6913.
- [136] B. Ding, M.B. Solomon, C.F. Leong, D.M. D'Alessandro, *Coord. Chem. Rev.* 439 (2021) 213891.
- [137] J. Tang, C. Su, Z. Shao, *Small Methods* 5 (2021) 2100945.
- [138] Y. Song, Q. Sun, B. Aguila, S. Ma, *Adv. Sci.* 6 (2019) 1801410.
- [139] M. Souto, K. Strutyński, M. Melle-Franco, J. Rocha, *Chem. Eur. J.* 26 (2020) 10912–10935.
- [140] M. Mozetic, *Materials* (Basel, Switzerland) vol. 12, 2019.
- [141] L. Ai, W. Li, Q. Wang, F. Cui, G. Jiang, *Chem. Cat. Chem.* 14 (2022) e202200935.
- [142] Z. Li, X. Feng, Y. Zou, Y. Zhang, H. Xia, X. Liu, Y. Mu, *Chem. Commun.* 50 (2014) 13825–13828.
- [143] S. Gao, Q. Zhang, X. Su, X. Wu, X.-G. Zhang, Y. Guo, Z. Li, J. Wei, H. Wang, S. Zhang, J. Wang, *J. Am. Chem. Soc.* 145 (2023) 9520–9529.
- [144] A.F.M. El-Mahdy, H.A.E. Omer, Z.A. Alotman, H. Lee, *J. Colloid Interface Sci.* 633 (2023) 775–785.
- [145] J. Cui, Y. Fu, J. Song, B. Meng, J. Zhou, Z. Zhou, Z. Su, *ChemSusChem* 16 (2023) e202202079.
- [146] H. Jia, B. Zhu, X. Zhi, Y. Du, J. Liu, G.A. Jie, Y. Fu, R. Ma, F. Zhang, W. Zhu, *Flat Chem.* 38 (2023) 100492.
- [147] P. Sarkar, S. Riyajuddin, A. Das, A. Hazra Chowdhury, K. Ghosh, S.M. Islam, *Molecular Catal.* 484 (2020) 110730.
- [148] W. Li, Q. Wang, F. Cui, G. Jiang, *RSC Adv.* 12 (2022) 17984–17989.
- [149] X. Wang, X. Ding, Y. Jin, D. Qi, H. Wang, Y. Han, T. Wang, J. Jiang, *Angew. Chem. Int. Ed.* 62 (2023) e202302808.
- [150] Y. Xiang, W. Dong, P. Wang, S. Wang, X. Ding, F. Ichihara, Z. Wang, Y. Wada, S. Jin, Y. Weng, H. Chen, J. Ye, *Appl. Catal. B Environ.* 274 (2020) 119096.
- [151] Y.H. Kim, N. Kim, J.-M. Seo, J.-P. Jeon, H.-J. Noh, D.H. Kweon, J. Ryu, J.-B. Baek, *Chem. Mater.* 33 (2021) 8705–8711.
- [152] S.-Q. You, J. Zhou, M.-M. Chen, C.-Y. Sun, X.-J. Qi, A. Yousef, X.-L. Wang, Z.-M. Su, *J. Catal.* 392 (2020) 49–55.
- [153] I. Hazra Chowdhury, A. Hazra Chowdhury, A. Das, A. Khan, S.M. Islam, *New J. Chem.* 44 (2020) 11720–11726.
- [154] L. Peng, S. Chang, Z. Liu, Y. Fu, R. Ma, X. Lu, F. Zhang, W. Zhu, L. Kong, M. Fan, *Cat. Sci. Technol.* 11 (2021) 1717–1724.
- [155] S.-Y. Li, S. Meng, X. Zou, M. El-Roz, I. Telegeev, O. Thili, T.X. Liu, G. Zhu, *Microporous Mesoporous Mater.* 285 (2019) 195–201.
- [156] M. Kou, W. Liu, Y. Wang, J. Huang, Y. Chen, Y. Zhou, Y. Chen, M. Ma, K. Lei, H. Xie, P.K. Wong, L. Ye, *Appl. Catal. B Environ.* 291 (2021) 120146.
- [157] H. Lv, P. Li, X. Li, A. Chen, R. Sa, H. Zhu, R. Wang, *Chem. Eng. J.* 451 (2023) 138745.
- [158] P. Sarkar, A. Das, S. Ghosh, S. Manirul Islam, *ChemCatChem* 14 (2022) e202200186.
- [159] H. Zhong, Z. Hong, C. Yang, L. Li, Y. Xu, X. Wang, R. Wang, *ChemSusChem* 12 (2019) 4493–4499.
- [160] R. Xu, X.-S. Wang, H. Zhao, H. Lin, Y.-B. Huang, R. Cao, *Cat. Sci. Technol.* 8 (2018) 2224–2230.
- [161] S. Chen, P. Kong, H. Niu, H. Liu, X. Wang, J. Zhang, R. Li, Y. Guo, T. Peng, *Chem. Eng. J.* 431 (2022) 133357.
- [162] V.S. Vyas, F. Haase, L. Stegbauer, G. Savasci, F. Podjaski, C. Ochsenfeld, B. V. Lotsch, *Nat. Commun.* 6 (2015) 8508.
- [163] M. Dong, W. Li, J. Zhou, S.-Q. You, C.-Y. Sun, X.-H. Yao, C. Qin, X.-L. Wang, Z.-M. Su, *Chin. J. Chem.* 40 (2022) 2678–2684.
- [164] Y. Guo, Q. Zhang, S. Gao, H. Wang, Z. Li, J. Qiu, Y. Zhao, Z. Liu, J. Wang, *Green Chem.* 24 (2022) 9530–9541.
- [165] Y.-N. Gong, W. Zhong, Y. Li, Y. Qiu, L. Zheng, J. Jiang, H.-L. Jiang, *J. Am. Chem. Soc.* 142 (2020) 16723–16731.
- [166] H. Lv, R. Sa, P. Li, D. Yuan, X. Wang, R. Wang, *SCIENCE CHINA Chem.* 63 (2020) 1289–1294.
- [167] Z. Zhang, J. Lu, K. Yang, J. Cao, Y. Zhao, K. Ge, S. Wang, Y. Yang, Y. Zhang, Y. Yang, *ChemistrySelect* 7 (2022) e202201203.
- [168] D. Song, W. Xu, J. Li, J. Zhao, Q. Shi, F. Li, X. Sun, N. Wang, *Chin. J. Catal.* 43 (2022) 2425–2433.
- [169] N. Xu, Y. Diao, C. Qin, Z. Xu, H. Ke, X. Zhu, *Dalton Trans.* 49 (2020) 15587–15591.
- [170] L.-J. Wang, R.-L. Wang, X. Zhang, J.-L. Mu, Z.-Y. Zhou, Z.-M. Su, *Chem. Sus. Chem.* 13 (2020) 2973–2980.
- [171] M. Lu, J. Liu, Q. Li, M. Zhang, M. Liu, J.-L. Wang, D.-Q. Yuan, Y.-Q. Lan, *Angew. Chem. Int. Ed.* 58 (2019) 12392–12397.
- [172] D. Wang, D. Streater, Y. Peng, J. Huang, *ChemPhotoChem* 5 (2021) 1119–1123.
- [173] W. Tu, Y. Yang, C. Chen, T. Zhou, T. Li, H. Wang, S. Wu, Y. Zhou, D. O'Hare, Z. Zou, R. Xu, *Small Struct.* 4 (2022) 2200233.
- [174] K. Lei, D. Wang, L. Ye, M. Kou, Y. Deng, Z. Ma, L. Wang, Y. Kong, *ChemSusChem* 13 (2020) 1725–1729.
- [175] H. Xue, C. Yin, S. Xiong, J. Yang, Y. Wang, *ACS Appl. Mater. Interfaces* 14 (2022) 49672–49679.
- [176] S. Yang, R. Sa, H. Zhong, H. Lv, D. Yuan, R. Wang, *Adv. Funct. Mater.* 32 (2022) 2110694.
- [177] P. Chakraborty, S. Ghosh, A. Das, A. Khan, S.M. Islam, *Cat. Sci. Technol.* 12 (2022) 3484–3497.
- [178] S. Biswas, A. Dey, F.A. Rahimi, S. Barman, T.K. Maji, *ACS Catal.* 13 (2023) 5926–5937.
- [179] L. Yang, W. Yan, N. Yang, G. Wang, Y. Bi, C. Tian, H. Liu, X. Zhu, *Small* 19 (2023) 2208118.
- [180] S. Zhang, S. Wang, L. Guo, H. Chen, B. Tan, S. Jin, *J. Mater. Chem. C* 8 (2020) 192–200.
- [181] J. Qiu, Y. Zheng, L. Wang, M. Liu, L. Tian, X. Yu, X. An, G. Lv, J. Mater. Chem. A 11 (2023) 4572–4578.
- [182] D. Uraguchi, Y. Tsuchiya, T. Ohtani, T. Enomoto, S. Masaoka, D. Yokogawa, T. Ooi, *Angew. Chem. Int. Ed.* 59 (2020) 3665–3670.
- [183] S.S. Dhankhar, C.M. Nagaraja, *Microporous Mesoporous Mater.* 308 (2020) 110314.

- [184] Z. Wang, Y. Huang, H. Li, X.-M. Li, *Microporous Mesoporous Mater.* 349 (2023) 112419.
- [185] S. Kandambeth, A. Mallick, B. Lukose, M.V. Mane, T. Heine, R. Banerjee, *J. Am. Chem. Soc.* 134 (2012) 19524–19527.
- [186] P. Guan, J. Qiu, Y. Zhao, H. Wang, Z. Li, Y. Shi, J. Wang, *Chem. Commun.* 55 (2019) 12459–12462.
- [187] Z. Wang, Y. Yang, Z. Zhao, P. Zhang, Y. Zhang, J. Liu, S. Ma, P. Cheng, Y. Chen, Z. Zhang, *Nat. Commun.* 12 (2021) 1982.
- [188] X. Zhuang, W. Zhao, F. Zhang, Y. Cao, F. Liu, S. Bi, X. Feng, *Polym. Chem.* 7 (2016) 4176–4181.
- [189] E. Jin, M. Asada, Q. Xu, S. Dalapati, M.A. Addicoat, M.A. Brady, H. Xu, T. Nakamura, T. Heine, Q. Chen, D. Jiang, *Science (New York, N.Y.)* vol. 357, 2017, pp. 673–676.
- [190] T. Jadhav, Y. Fang, W. Patterson, C.-H. Liu, E. Hamzehpoor, D.F. Perepichka, *Angew. Chem. Int. Ed.* 58 (2019) 13753–13757.
- [191] Z. Zhao, D. Zheng, M. Guo, J. Yu, S. Zhang, Z. Zhang, Y. Chen, *Angew. Chem. Int. Ed.* 61 (2022) e202200261.
- [192] H.J. Son, F. He, B. Carsten, L. Yu, *J. Mater. Chem.* 21 (2011) 18934–18945.
- [193] H.-L. Qian, F.-L. Meng, C.-X. Yang, X.-P. Yan, *Angew. Chem. Int. Ed.* 59 (2020) 17607–17613.
- [194] Z.-B. Zhou, X.-H. Han, Q.-Y. Qi, S.-X. Gan, D.-L. Ma, X. Zhao, *J. Am. Chem. Soc.* 144 (2022) 1138–1143.
- [195] S. Ma, Z. Li, J. Jia, Z. Zhang, H. Xia, H. Li, X. Chen, Y. Xu, X. Liu, *Chin. J. Catal.* 42 (2021) 2010–2019.
- [196] D. Stewart, D. Antypov, M.S. Dyer, M.J. Pitcher, A.P. Katsoulidis, P.A. Chater, F. Blanc, M.J. Rosseinsky, *Nat. Commun.* 8 (2017) 1102.
- [197] P.-L. Wang, S.-Y. Ding, Z.-C. Zhang, Z.-P. Wang, W. Wang, *J. Am. Chem. Soc.* 141 (2019) 18004–18008.
- [198] R. Luo, W. Xu, M. Chen, X. Liu, Y. Fang, H. Ji, *ChemSusChem* 13 (2020) 6509–6522.
- [199] L. Guo, S. Jin, *ChemPhotoChem* 3 (2019) 973–983.
- [200] M. Liu, L. Guo, S. Jin, B. Tan, *J. Mater. Chem. A* 7 (2019) 5153–5172.
- [201] C. Gu, D. Liu, W. Huang, J. Liu, R. Yang, *Polym. Chem.* 6 (2015) 7410–7417.
- [202] A.A. Olajire, *J. CO2 Util.* 17 (2017) 137–161.
- [203] J. Huo, B. Luo, Y. Chen, *ACS omega* 4 (2019) 22504–22513.
- [204] J. You, Y. Zhao, L. Wang, W. Bao, *J. Clean. Prod.* 291 (2021) 125822.
- [205] R. Sun, B. Tan, *Chem. – A Eur. J. Dermatol.* 29 (2023) e202203077.
- [206] R. Sun, B. Tan, *Chem. Res. Chin. Univ.* 38 (2022) 310–324.
- [207] Y. Zhu, D. Zhu, Y. Chen, Q. Yan, C.-Y. Liu, K. Ling, Y. Liu, D. Lee, X. Wu, T. P. Senftle, R. Verduzco, *Chem. Sci.* 12 (2021) 16092–16099.
- [208] M. Chen, H. Li, C. Liu, J. Liu, Y. Feng, A.G.H. Wee, B. Zhang, *Coord. Chem. Rev.* 435 (2021) 213778.
- [209] Q. Zhang, S. Gao, Y. Guo, H. Wang, J. Wei, X. Su, H. Zhang, Z. Liu, J. Wang, *Nat. Commun.* 14 (2023) 1147.
- [210] S. Wang, Z. Chen, Y. Cai, X.-L. Wu, S. Wang, Z. Tang, B. Hu, Z. Li, X. Wang, *Environ. Funct. Mat.* 2 (2023) 76–92.
- [211] T. Luo, L. Gilmanova, S. Kaskel, *Coord. Chem. Rev.* 490 (2023) 215210.
- [212] X. Jiao, K. Zheng, Z. Hu, Y. Sun, Y. Xie, *ACS Central Sci.* 6 (2020) 653–660.
- [213] Q. Pan, M. Abdellah, Y. Cao, W. Lin, Y. Liu, J. Meng, Q. Zhou, Q. Zhao, X. Yan, Z. Li, H. Cui, H. Cao, W. Fang, D.A. Tanner, M. Abdel-Hafiez, Y. Zhou, T. Pullerits, S.E. Canton, H. Xu, K. Zheng, *Nat. Commun.* 13 (2022) 845.
- [214] H.-J. Zhu, M. Lu, Y.-R. Wang, S.-J. Yao, M. Zhang, Y.-H. Kan, J. Liu, Y. Chen, S.-L. Li, Y.-Q. Lan, *Nat. Commun.* 11 (2020) 497.
- [215] M. Calik, F. Auras, L.M. Salonen, K. Bader, I. Grill, M. Handloser, D.D. Medina, M. Dogru, F. Löbermann, D. Trauner, A. Hartschuh, T. Bein, *J. Am. Chem. Soc.* 136 (2014) 17802–17807.
- [216] C. Mo, M. Yang, F. Sun, J. Jian, L. Zhong, Z. Fang, J. Feng, D. Yu, *Adv. Sci.* 7 (2020) 1902988.
- [217] Y. Wang, H. Liu, Q. Pan, C. Wu, W. Hao, J. Xu, R. Chen, J. Liu, Z. Li, Y. Zhao, *J. Am. Chem. Soc.* 142 (2020) 5958–5963.
- [218] S. Lin, C.S. Diercks, Y.-B. Zhang, N. Kornienko, E.M. Nichols, Y. Zhao, A.R. Paris, D. Kim, P. Yang, O.M. Yaghi, C.J. Chang, *Science (New York, N.Y.)* vol. 349, 2015, pp. 1208–1213.
- [219] L. Wang, L. Wang, S. Yuan, L. Song, H. Ren, Y. Xu, M. He, Y. Zhang, H. Wang, Y. Huang, T. Wei, J. Zhang, Y. Himeida, Z. Fan, *Appl. Catal. B Environ.* 322 (2023) 122097.
- [220] J. Jiang, Y. Chen, H. Ji, *J. CO2 Util.* 60 (2022) 101972.
- [221] H.-B. Wu, W. Zou, S.-X. Shao, X.-T. Zhou, Z.-H. Zhou, Y.-X. Fang, *Catal. Today* 402 (2022) 202–209.
- [222] Y. Zhang, L. Cao, G. Bai, X. Lan, *Small* 19 (2023) 2300035.
- [223] X. Li, C. Tang, L. Zhang, M. Song, Y. Zhang, S. Wang, *Biomimetics* 8 (2023) 171.
- [224] R. Chen, Y. Wang, Y. Ma, A. Mal, X.-Y. Gao, L. Gao, L. Qiao, X.-B. Li, L.-Z. Wu, C. Wang, *Nat. Commun.* 12 (2021) 1354.
- [225] N. Lv, Q. Li, H. Zhu, S. Mu, X. Luo, X. Ren, X. Liu, S. Li, C. Cheng, T. Ma, *Adv. Sci.* 10 (2023) 2206239.
- [226] L.-S. Hornberger, F. Polymers, Adams, in, 2022.
- [227] H. Ding, A. Mal, C. Wang, *Mat. Chem. Front.* 4 (2020) 113–127.
- [228] Y. Yusran, X. Guan, H. Li, Q. Fang, S. Qiu, *Natl. Sci. Rev.* 7 (2020) 170–190.
- [229] J.L. Segura, S. Royuela, M. Mar Ramos, *Chem. Soc. Rev.* 48 (2019) 3903–3945.
- [230] G. Jiang, W. Zou, Z. Ou, W. Zhang, Z. Liang, L. Du, *Chem. Eur. J.* 29 (2023) e202203610.
- [231] X. Li, J. Xiong, Z. Tang, W. He, Y. Wang, X. Wang, Z. Zhao, Y. Wei, *Molecules*, Basel, Switzerland, 2023.
- [232] K.Y. Kumar, H.B. Muralidhara, Y.A. Nayaka, J. Balasubramanyam, H. Hanumanthappa, *Powder Technol.* 246 (2013) 125–136.
- [233] K. Lorber, P. Djinić, *iScience* 25 (2022) 104107.
- [234] S. Navalón, A. Dhakshinamoorthy, M. Álvaro, H. Garcia, *ChemSusChem* 6 (2013) 562–577.
- [235] Y. Chen, D. Wang, X. Deng, Z. Li, *Cat. Sci. Technol.* 7 (2017) 4893–4904.
- [236] D. Zhu, J.-J. Zhang, X. Wu, Q. Yan, F. Liu, Y. Zhu, X. Gao, M.M. Rahman, B. I. Yakobson, P.M. Ajayan, R. Verduzco, *Chem. Sci.* 13 (2022) 9655–9667.
- [237] F. Arcudi, L. Đorđević, B. Nagasing, S.I. Stupp, E.A. Weiss, *J. Am. Chem. Soc.* 143 (2021) 18131–18138.
- [238] H.-L. Wu, X.-B. Li, C.-H. Tung, L.-Z. Wu, *Adv. Mater.* 31 (2019) 1900709.
- [239] X. Yao, Y. Wang, X. Lang, Y. Zhu, Q. Jiang, *Phys. E.* 109 (2019) 11–16.
- [240] S.K. Pandey, R. Das, P. Mahadevan, *ACS Omega* 5 (2020) 15169–15176.
- [241] B. Gidwani, V. Sahu, S.S. Shukla, R. Pandey, V. Joshi, V.K. Jain, A. Vyas, *J. Drug Del. Sci. and Techn.* 61 (2021) 102308.
- [242] S. Nikazar, V.S. Sivasankarapillai, A. Rahdar, S. Gasmí, P.S. Anumol, M. S. Shanavas, *Biophys. Rev.* 12 (2020) 703–718.
- [243] H. Moon, C. Lee, W. Lee, J. Kim, H. Chae, *Adv. Mater.* 31 (2019) 1804294.